Computational Studies of Aromatic and Photophysical Properties of Carbarporphyrinoids

Master's thesis

Isaac Benkyi

August, 2016

Supervisor: Prof. Dage Sundholm

UNIVERSITY OF HELSINKI
Department of Chemistry
Laboratory for Instruction in Swedish

“Imagination is more important than knowledge. For knowledge is limited to all we now know and understand, while imagination embraces the entire world, and all there ever will be to know and understand.”

—Albert Einstein

HELSINGIN YLIOPISTO — HELSINGFORS UNIVERSITET — UNIVERSITY OF HELSINKI

Tiedekunta — Fakultet — Faculty	Laitos — Institution — Department
Faculty of Science	Department of Chemistry

Tekijä — Författare — Author
Isaac Benkyi

Työn nimi — Arbetets titel — Title
Computational Studies of Aromatic and Photophysical Properties of Carbarporphyrinoids

Oppiaine — Läroämne — Subject
Chemistry

Työn laji — Arbetets art — Level	Aika — Datum — Month and year	Sivumäärä — Sidoantal — Number of pages
Master's thesis	August, 2016	92

Tiivistelmä — Referat — Abstract

Porphyrins and porphyrin derivatives are naturally occurring molecules, whereas carbaporphyrinoids are synthesized porphyrin derivatives. They have received much attention in recent years by the scientific community due to their diverse potential applications in technological developments such as molecular electronic devices and conversion of solar energy. However, the full utilization of this class of compounds can not be realized without an in-depth understanding of their chemical and physical properties. Two of such properties are aromaticity and optical properties. In this thesis, the aromatic properties and the light absorption spectra in the ultraviolet and visible (UV-Vis) range have been studied computationally for some recently synthesized carbaporphyrins and carbachlorins using first-principle computational approaches.

In the first part of the thesis, the background of carbaporphyrinoids and some examples of naturally occuring porphyrins and porphyrin derivatives are delineated. The second and third part review theoretical and computational methods that are employed in studies of the molecular aromaticity and electronic excitation spectra of molecules. The computational studies of magnetically induced current densities and electronic excitation energies are discussed in the fourth chapter. The obtained results are also presented in chapter four and the main conclusions are summarized in the last chapter.

The study shows that all the carbaporphyrinoids studied sustain a magnetically induced ring current in the porphyrin macro ring. This indicates that they are aromatic according to the ring-current criterion. However, the calculated ring-current pathways differ from those predicted from the nucleus independent chemical shift (NICS) calculations and the current pathways deduced from ^{1}H NMR spectroscopy studies.

The vertical excitation energies which is akin to the ultraviolet-visible spectrum obtained experimentally for some of the selected carbaporphyrinoids also showed deviations from those of the experimental values. These deviations can be ascribed to solvent effects as in the calculation of the vertical excitation energies, solvent effects were not accounted for.

Avainsanat — Nyckelord — Keywords
Aromaticity, Magnetically induced current density, UV-Vis spectroscopy, Carbaporphyrins

Säilytyspaikka — Förvaringsställe — Where deposited
E-thesis

Muita tietoja — övriga uppgifter — Additional information

List of Figures

List of Tables

List of Abbreviations

ARCS	Aromatic Ring Current Shieldings
CASSCF	Complete Active Space Self-Consistent Field
CASPT2	Complete Active Space Second-Order Perturbation Theory
CC	Coupled Cluster
CDA	Current Density Analysis
CHF	Coupled Hartree-Fock
CI	Configuration Interaction
CISD	Configuration Interaction Singles and Doubles
CMO	Canonical Molecular Orbitals
CTOCD	Continuous Transformation of the Origin of the Current Density
DFT	Density Functional Theory
FCI	Full Configuration Interaction
GIAO	Gauge Including Atomic Orbitals
GIMIC	Gauge Including Magnetically Induced Currents
HF-SCF	Hartree-Fock Self-Consistent Field
HOMO	Highest Occupied Molecular Orbital
LMO	Localized Molecular Orbital
LUMO	Lowest Unoccupied Molecular Orbital
MP2	Second-Order Møller-Plesset Perturbation Theory
MRCI	Multireference Configuration Interaction
MO	Molecular Orbital
NMR	Nuclear Magnetic Resonance
PAHs	Polyaromatic Hydrocarbons
PES	Potential Energy Surface

NICS	Nucleus-Independent Chemical Shift
RASSCF	Restricted Active Space Self-Consistent Field
RICC2	Resolution of Identity Second-Order Approximate Coupled-Cluster
SCF	Self-Consistent Field
TDDFT	Time-dependent Density Functional Theory
TMS	Tetramethylsilane
TZP	Polarized Triple Zeta
UV-Vis	Ultraviolet-Visible
^{13}C NMR	Carbon-13 Nuclear Magnetic Resonance
^{1}H NMR	Proton Nuclear Magnetic Resonance

Contents

1. INTRODUCTION

Porhyrins are a class of organic heterocyclic macromolecules consisting of four modified pyrrole subunits interconnected at their α-carbon atoms via a methine bridge (=CH-). The parent porphyrin is free-base porphin called porphin (Figure 1.1a). Substituted porphyrins and porphyrin derivatives are called porphyrinoids. The name porphyrin comes from the Greek word *porphyros* meaning purple[1] which signifies their deeply coloured nature. They are naturally occurring, one of the best known is the porphyrin found in heme (Figure 1.2a), which is made up of a porphyrin whose nitrogen atoms bind to iron. Chlorophyll (Figure 1.2b), the green pigments found in plants, consists of porphyrin which binds to magnesium. Vitamin B_{12}, whose deficiency in humans results in pernicious anemia, is formed from a porphyrin derivative that binds to cobalt.

(a) **(b)**

Figure 1.1: The molecular structure of a) porphin and b) carbaporphin

Carbaporphyrinoids (Figure 1.1b) are porphyrin analogues in which one of the nitrogen atoms of the porphyrin macroring is substituted by a carbon atom.[2–7] The strong conjugation this class of organic compounds exhibits results in intense absorption bands in the ultraviolet-visible (UV-Vis) spectrum. Porphyrins and porphyrin derivatives have

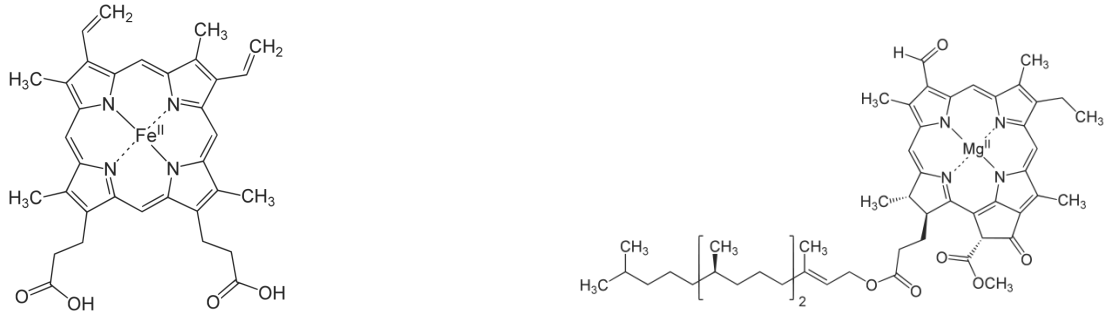

Figure 1.2: The molecular structure of a) heme and b) chlorophyll

attracted much attention in the scientific community because they are ubiquitous in nature and have potential applications in catalysis,[2,7] photodynamic therapy,[8] molecular electronic devices,[9] and conversion of solar energy.[10] These diverse potential applications emanate from the special absorption, emission, charge transfer, and complexing properties porphyrins exhibit. These manifold characteristics of porphyrins result from their ring structure which is made up of conjugated double bonds.

The full utilization of this class of organic compounds cannot be achieved without a better understanding of their aromaticity and optical properties. As most organic (heterocyclic) compounds which exhibit conjugation, the Hückel's $(4n + 2)\pi$ rule (where n is an integer) is obeyed in this class of compounds and one will expect that they are aromatic.

Aromaticity has been generally attributed to the cyclic delocalization of $(4n + 2)\pi$-electrons. However, this view has been challenged by the suggestion that the σ (sigma) electrons in benzene also participate in the bond equalization of the benzene ring.[11]

Although variedly defined, aromaticity has been associated with chemical behaviour (electrophilic aromatic substitution), structural properties (bond length equalization due to cyclic electron delocalization), energetics (enhanced stability) as well as magnetic properties ("ring current" effect). Among these, the magnetic properties are considered as one of the most reliable criteria for studies of aromaticity.[12] The magnetic criterion for aromaticity is based on the early work of London[13], Pople[14,15] and McWeeny[16]. They proposed that the presence of delocalized π-electrons in a molecule sustains a ring cur-

rent in the presence of an external magnetic field.

Optical properties of molecules are usually studied using various spectroscopic methods. The absorption of light by molecules is responsible for the colouration of many molecules and compounds found in nature. The UV-Vis spectroscopy, which is used to measure the absorption of light near the ultraviolet-visible region of the electromagnetic spectrum by molecules is a reliable spectroscopic tool for the determination of the photophysical properties of molecules.

Porphyrins and porphyrinoid derivatives exhibit extremely intense absorption bands, (Figure 1.3) the so-called Soret or B-bands in the 380-500 nm range with molar absorption coefficients of $10^5 M^{-1}cm^{-1}$. They also show a set of bands in the range of 500-700 nm, which are called Q-bands. The Q-bands are weak for porphin and many porphyrins except for chlorophylls, chlorins and porphyrinoids with broken D_{4h} (D_{2h}) symmetry. The Q-band can consist of many bands because of vibrational effects.

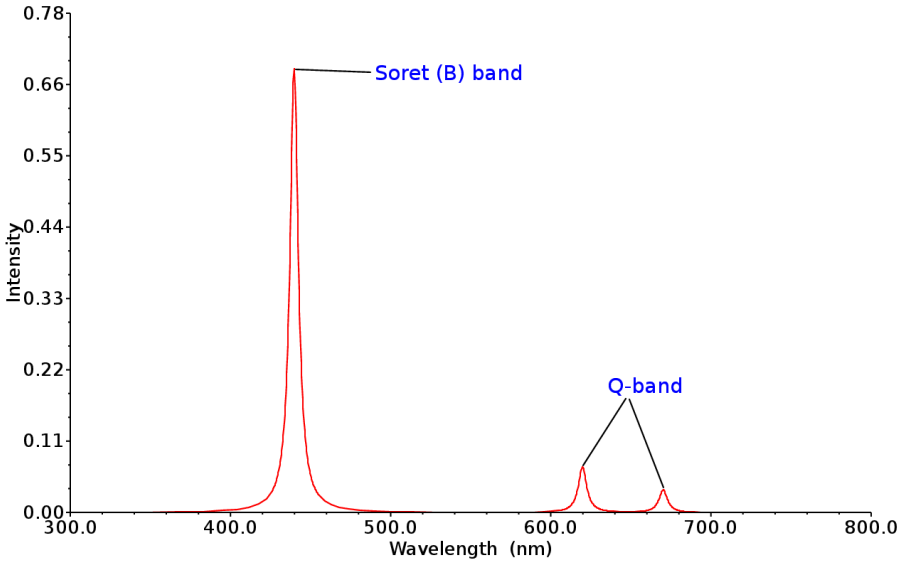

Figure 1.3: The absorption spectrum of porphyrins

2. AROMATICITY

2.1 Introduction

The isolation of benzene in 1825 by Michael Faraday[17,18] presented a great challenge of determining and understanding the structure of the compound to chemists. The empirical formula for benzene was long known, however, the elucidation of its cyclical structure is usually attributed to August Kekulé in his 1865 paper.[19,20] The unusual stability and distinct odour of this class of compounds earn them the name aromatic compounds.

Over the years, aromaticity has become one of the most evasive concept in chemistry, though easy to detect, yet difficult to define.[21] This difficulty can be ascribed to the fact that different fields use the term "aromaticity" differently. To a biochemist aromaticity might mean a part of a molecule involved in a special type of intermolecular interaction, whereas to an organic chemist it may refer to the special stability associated with unsaturated compounds under different reaction conditions. Theoretical and physical chemists might associate aromaticity with the magnetic properties of a compound.[21]

Over the years, several magnetic criteria have been proposed for the studies of the aromaticity of compounds. These include

i NMR Chemical Shifts

ii Magnetic Susceptibility Exaltation

iii Nucleus Independent Chemical Shifts

iv Current Density Analysis

The magnetic criteria make use of the fact that external magnetic fields induce currents

in the electron density of the molecules.

2.2 NMR Chemical Shifts

2.2.1 Background

Nuclear Magnetic Resonance (NMR) is a spectroscopic tool used by chemists to exploit the interaction of the nuclear magnetic moment with an external magnetic field to provide information about the molecular structure and related properties of molecules.

Some nuclei posses an intrinsic angular momentum similar to the electron spin called the nuclear angular momentum. The nuclear spin angular momentum is defined by two quantum numbers, the spin quantum number, I, and the magnetic momentum quantum number m_I. The magnitude of the nuclear spin angular momentum is given by

$$|\mathbf{I}| = \hbar\sqrt{I(I+1)} \tag{2.1}$$

The nuclear spin angular momentum is a vector quantity and in the z-direction it is given by

$$I_z = m_I\hbar \tag{2.2}$$

$\hbar$ is Planck's constant (h) divided by 2π. For a nucleus of spin I, the possible number of orientations or spin states is

$$2I + 1 \tag{2.3}$$

Protons and neutrons are fermions which have a spin of $\frac{1}{2}$. The individual spin of the protons and neutrons of the nucleus add to give the nuclear spin of the nucleus. Depending on the number of protons and neutrons in an atom, the total spin quantum number varies for each atom. For atoms with even proton number (atomic number) and even mass number (sum of proton and neutron) the net spin quantum number value is zero. Atoms with an even number of protons and an odd mass number, as well as atoms with odd proton number and even mass number have non-zero spin value. ^{1}H, ^{13}C, and ^{15}N are some examples of nuclei with spin of $\frac{1}{2}$. Others such as ^{2}H, ^{11}B, and ^{14}N have spin greater than $\frac{1}{2}$ and are referred to as quadrupolar nuclei. Nuclei with spin $\frac{1}{2}$ are the most

studied in NMR spectroscopy. The spin of the nucleus gives raise to the nuclear magnetic moment. The magnitude of the magnetic moment (μ) is

$$\mu = \gamma \hbar I \tag{2.4}$$

Here, γ is characteristic for the nucleus and is referred to as the *gyromagnetic* or *magnetogyric ratio.*

In NMR experiments, the nucleus is subjected to a strong laboratory magnetic field B. In the absence of the external magnetic field, magnetic nuclei of the same isotopes have the same energy. When the field is turned on along a direction, usually designated as *z-direction*, the energies of the nuclei are affected. For spin-half nuclei, which can assume two states, the state with slightly lower energy has more spin population than the higher energy state according to the Boltzmann's distribution. The energy difference between the states is

$$\Delta E = \gamma \hbar B \tag{2.5}$$

This energy difference is extremely small even with a very large magnetic field in comparison to the vibrational or electronic states. This means that very large magnets are required for NMR experiments. The energy difference can also be related to the frequency as

$$h\nu = \Delta E = \gamma \hbar B \tag{2.6}$$

This frequency at which there is an appreciable change in energy between the two spin states is referred to as the resonance frequency. The NMR resonance frequency also referred to as the **Larmor frequency** (ν) is then expressed as

$$\nu = \frac{\gamma}{2\pi} B \tag{2.7}$$

2.2.2 ^{1}H NMR Chemical Shifts

The actual magnetic field, B_{local}, experienced by the nucleus in a molecule is slightly different from the applied field $B_{external}$. In the presence of an external magnetic field, the electrons in the molecule will move and the electron current gives rise to an induced

magnetic field, δB, which might align with or be opposite to the external magnetic field. Thus the local magnetic field experienced by a particular nucleus is

$$B_{local} = B_{external} - \delta B \tag{2.8}$$

The influence of the local electronic structure on the actual magnetic field experienced by a particular nucleus is termed shielding. The induced magnetic field resulting from the electronic structure is related to the applied magnetic field by a constant, σ, called the shielding constant

$$\delta B = -\sigma B_{external} \tag{2.9}$$

The shielding constant, σ, is unique for any nuclei in a molecule as it depends on the local environment of the nuclei. The magnetic field, B_{local}, can then be expressed as

$$B_{local} = B_{external} - \sigma B_{external} \tag{2.10a}$$

$$B_{local} = (1 - \sigma) B_{external} \tag{2.10b}$$

By substituting Equation 2.10b into Equation 2.7, the Larmor frequency becomes

$$\nu = \frac{\gamma}{2\pi}(1 - \sigma) B_{external} \tag{2.11}$$

Since the Larmor frequency from Equation 2.11 depends on the shielding constant, which is unique for nuclei of the same element, different nuclei of the same element comes to resonance at different frequencies. The resonance frequency is generally expressed in terms of an empirical quantity called the NMR chemical shift (δ).

$$\delta = \frac{\nu - \nu^o}{\nu^o} \tag{2.12}$$

where

δ is the chemical shift

ν is the resonance frequency of the nucleus under consideration

ν^o is the resonance frequency of the nucleus of a reference compound.

For proton NMR, the reference compound often used is tetramethylsilane (TMS). It is also possible to express NMR chemical shifts in terms of the shielding constant of the reference compound, σ_{ref}, and that of the sample under study, σ_{sample},

$$\delta = (\sigma_{ref} - \sigma_{sample}) \times 10^6 \tag{2.13}$$

It is common to report the chemical shift values in ppm (parts per million). The shielding σ, becomes smaller as the chemical shift value increases. Such nuclei are said to be deshielded whereas those with large values of σ would have smaller chemical shift values and they are said to be shielded. It is a standard practice to record the chemical shift values (in ppm) on a scale with increasing chemical shift values to the left as shown in Figure 2.1. With this convention, nuclei with large chemical shift values are said to be downfield whereas those with large values are said to be upfield relative to each other.

For organic compounds, hydrogens of different functional groups have distinct chemical shift values as a result of the unsimilar environment of the hydrogens (Figure 2.2). In benzene, which is an archetypical aromatic compound, the proton chemical shift

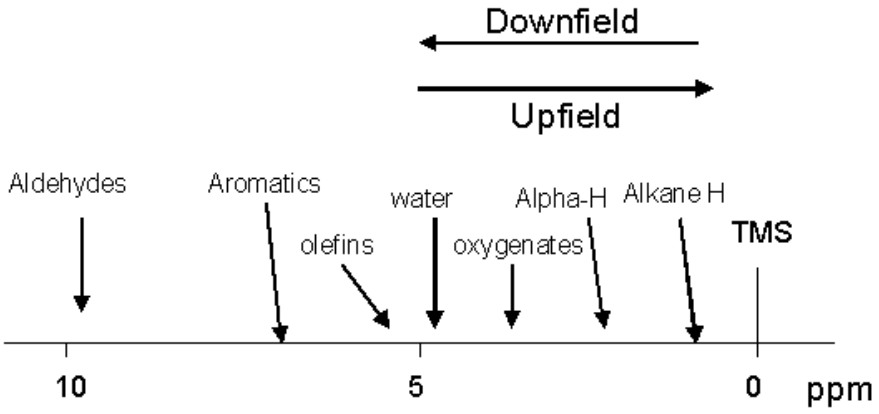

Figure 2.1: ^{1}H NMR scale showing the downfield and upfield directions

is observed at 7.3 ppm, 1.6 ppm downfield from the δ = 5.6-5.8 ppm range of the $\delta(^1H)$ of the olefinic protons in cyclohexene, 1,3-cyclohexadiene, and 1,4-cyclohexadiene.[22] Thus, the nucleus of the hydrogen atoms of aromatic compounds is said to be deshielded. The deshielding of the protons in aromatic compounds is attributed to the fact that in the presence of a magnetic field, the π-electrons in the aromatic ring induce a net diatropic

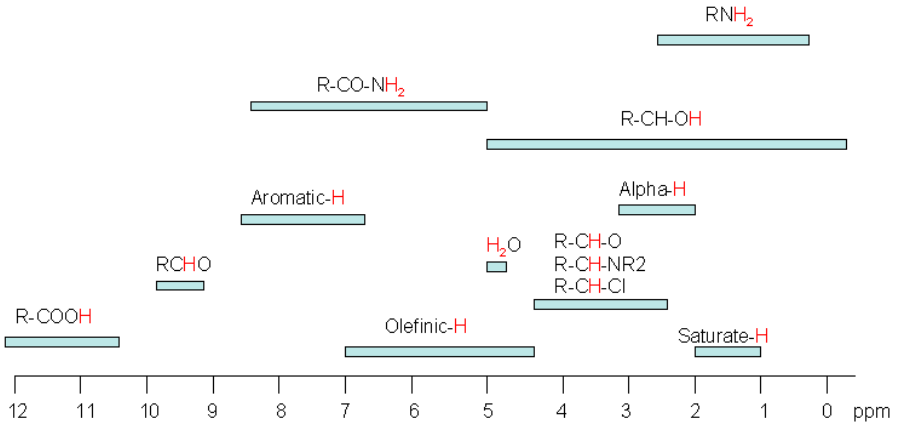

Figure 2.2: ^{1}H NMR scale of organic functional groups and where their hydrogens are observed

ring current giving rise to an induced magnetic field.[23–27] Antiaromatic compounds on the other hand exhibit induced net paratropic ring current resulting in an upfield proton chemical shift value.

Proton chemical shifts in NMR spectroscopy have long been the primary experimental tool used to indicate aromaticity in unsaturated organic rings. For instance, the [18]annulene has an experimental[28,29] ^{1}H NMR chemical shift of 9.17 ppm for the outer protons and -2.96 ppm for the inner protons. The downfield shift of the outer protons and the upfield shift of the inner protons are manifestations of a molecular ring current induced by an external magnetic field. However, proton chemical shifts of arene hydrogens, do not depend solely on ring current effects. Polyolefins can have arene-like proton chemical shifts.[30] This means that it is difficult to predict the aromaticity of organic compounds based on proton chemical shifts.

NMR spectroscopy involves probing the energy required to flip a nuclear spin in the presence of an external magnetic field.[31–34] To compute the NMR chemical shifts of molecules requires that a reasonable molecular structure is used.[32] This is usually achieved by geometry optimization procedures. The geometry optimization procedure is dependent on the choice of basis set and the level of theory used. When reasonable geometry has been obtained, the NMR isotropic shielding constant (σ) or the shielding tensor for the various nuclei in the molecule can then be computed. The shielding tensor is obtained as a second derivative of the total electronic energy (E) in the limit of zero

magnetic field (B) and magnetic moment (μ).

$$\sigma_{\alpha\beta} = \left.\frac{\partial^2 E}{\partial \mu_\alpha \partial B_\beta}\right|_{B=\mu=0} \tag{2.14}$$

where α and β are the components of the induced magnetic moment and the external magnetic field respectively.

The proton chemical shift is then obtained by computing the NMR isotropic shielding constant (σ) of a reference compound, usually tetramethylsilane (TMS) using the same level of theory as the one for the compound under investigation. Using the same level of theory for the NMR isotropic shielding constant (σ) helps in error cancellation.[35] The proton chemical shift, δ_i, of a particular nucleus is computed as

$$\delta_i = \sigma_{ref} - \sigma_i \tag{2.15}$$

where ;

σ_{ref} = isotropic shielding constant of the nucleus of the reference compound

σ_i = isotropic shielding constant of a particular nucleus.

Lash et al.[36] reported the experimental NMR chemical shifts for carbaporphyrinoids and opined that the downfield and the upfield chemical shift values of the outer and inner hydrogens respectively betokens the presence of an induced ring current.

2.3 Magnetic Susceptibility Exaltation

Diamagnetic materials have atoms with no permanent magnetic dipole moment. In the presence of an external magnetic field, a weak induced magnetic dipole is created which is directed opposite to the direction of the applied field. The magnetic field is described by two vector fields; the magnetic field strength, B, and the magnetic field intensity, H, which are related by

$$B = \mu_o H \tag{2.16}$$

where μ_o is the vacuum permeability. The density of the induced magnetic dipole moment called the magnetization or magnetic polarization is

$$M = \frac{d\mathbf{m}}{d\mathbf{V}} \tag{2.17}$$

where $d\mathbf{m}$ is the elementary magnetic moment and $d\mathbf{V}$ is the volume element. The magnetic field strength B, in a material is defined in terms of the magnetization and the magnetic field intensity by the relation

$$B = \mu_o(H + M) \tag{2.18}$$

The magnetization, M, is also related to the magnetic field intensity, H, by the relation

$$M = \chi H \tag{2.19}$$

χ is a dimensionless quantity referred to as the magnetic susceptibility.

A magnetic susceptibility (χ) is merely the quantitative measure of the response of a material to an applied (i.e., external) magnetic field.[37] Materials are usually classified as paramagnetic or diamagnetic based on their magnetic susceptibility. Materials for which χ is positive can be paramagnetic whereas those with negative values of χ are diamagnetic. Non-magnetic materials are generally said to be paramagnetic or diamagnetic because they do not possess permanent magnetization in the absence of an external magnetic field. On the other hand, ferromagnetic, ferrimagnetic, and antiferromagnetic materials have positive magnetic susceptibility and possess permanent magnetization in the absence of an external magnetic field.

In general the susceptibility of diamagnetic substances is independent of temperature and field strength.[38] The susceptibility of paramagnetic substances is inversely proportional to the absolute temperature and independent of field strength. The dependency of the susceptibility of a ferromagnetic substance on temperature and field strength is complicated.[37]

The molar magnetic susceptibility (χ_M) is the magnetic susceptibility per gram-molecular weight of a compound. In molecules, the molar magnetic susceptibility (χ_M) is used in measuring the magnetic susceptibility of the compound. Due to the rapid tumbling of the molecules, the molar susceptibility of compounds in fluids is the average of the susceptibility in the three dimensional Cartesian coordinates.[39,40]

$$\chi_M = \frac{1}{3}(\chi_x + \chi_y + \chi_z) \tag{2.20}$$

If the molecular plane is taken in the z-direction, the diamagnetic anisotropy, $_{\Delta}\chi$, given by $_{\Delta}\chi = \chi_z - \frac{1}{2}(\chi_x + \chi_y)$ has a large magnitude in aromatic compounds. This has been attributed to the presence of the delocalization of the π-electrons in these compounds.[41] Though this seems to be a very convenient way to detect aromaticity, the challenge associated with diamagnetic anisotropy is the difficulty in direct measurement of the anisotropy.[25,42] This prompted the use of magnetic susceptibility exaltation, Λ, which was postulated by Dauben et al.[42] as a measure of aromaticity.

The magnetic susceptibility exaltation (Λ)[42] is defined as the difference between the bulk magnetic susceptibility (χ_M) of a compound and the susceptibility ($\chi_{M'}$) estimated from an increment system for the same system without cyclic conjugation. The magnitude of the exaltation (Λ) is then used as a criterion for the determination of the aromatic character of any compound. For aromatic compounds $\Lambda \gg 0$ whereas all other compounds which are not aromatic have $\Lambda \sim 0$. Several methods exist for the estimation of the magnetic susceptibility of the increment system without cyclic conjugation.

The Pascal method[43,44] of diamagnetic susceptibility (χ) computes the susceptibility as the summation of the susceptibility of the individual atoms in the molecule and includes a correction factor to account for the structure of the molecule.[45]

$$\chi = \sum \chi_i + \lambda \tag{2.21}$$

χ_i is the magnetic susceptibility of the ith atom in the molecule and λ is the corrective factor for the structure (bonds) of the molecule.

The atom and bonding increment system introduced by Haberditzl et al.[46] improves on the Pascal system by using a wave-mechanical approach. In this approach, the magnetic susceptibility is accounted for from three different factors. 1) The magnetic susceptibility contribution from the inner-shell core electrons (χ_{ce}); 2) the magnetic susceptibility contribution from the bonds present in the molecule (χ_{bonds}); and 3) the magnetic susceptibility contribution from the π-electrons (χ_π). The magnetic susceptibility of the compound can then be expressed as

$$\chi_M = \sum \chi_{ce} + \sum \chi_{bonds} + \sum \chi_\pi \tag{2.22}$$

For most aromatic compounds, by using the Haberditzl approach or any of the

several empirical systems currently available to estimate the magnetic susceptibility of a similar system without conjugation, the magnetic susceptibility exaltation (Λ) is then obtained. It is then used as a measure of the aromatic character of the compound. For instance, by using the Haberditzl approach Dauben et al.[42] reported magnetic susceptibility exaltation of 13.7 for benzene and 0.0 for cyclohexane.

2.4 Nucleus-Independent Chemical Shifts

The Nucleus-Independent Chemical Shifts (NICS) method was proposed by Schleyer et al.[47] in 1996 as a magnetic criterion for the determination of the aromatic character of molecules. The first NICS model introduced by Schleyer et al.[47] involves computing the absolute magnetic shieldings at the center of the molecular ring using any available quantum chemistry program. This involves determining the center of the molecule (by the non-weighted average of the coordinates of the heavy atoms) and placing a dummy atom at this position. The magnitude of the shielding constant obtained is then reversed, (in order to conform to NMR sign convention) to obtain the NICS value. A negative NICS value denote aromaticity whereas a positive value shows antiaromaticity. They claimed that the NICS approach has the advantage that it shows a modest dependence on the ring size as compared to the magnetic susceptibility exaltation approach.

However, the use of this NICS method in determining the aromatic character is not without shortfall. It is long known since the beginning of NMR that the magnetic environment of any nucleus is influenced by functional groups and the CC and CH single bonds. This means that the magnetic shieldings calculated at the center of the molecule is not only affected by the ring current in aromatic compounds but also by the presence of the CC and CH σ (sigma) framework. This results in a nonzero NICS value for nonaromatic, saturated and unsaturated hydrocarbons rings.[48] This pitfall in NICS precipitated the modification of the NICS method, the original NICS as proposed by Schleyer et al. in 1996 now referred to as NICS(0).

To offset the effect of the local contribution to the computed NICS values, Schleyer in 1997 proposed the NICS(1)[49]. In this approach, the magnetic shielding of the dummy

atom is computed at 1Å above the ring centre. This leads to the system where the magnetic shielding can be calculated at any distance above the ring centre, designated NICS(x), where x is the distance above the ring centre.[50]

In solution, NMR measurements are unoriented as a result of the rapid tumbling of the molecules. NMR measurements are therefore isotropic (average of the measurements in all directions). The magnetic shielding computed using the above NICS techniques are therefore based on the total isotropic shielding values. This, however, does not reflect a "true" measure of π-aromaticity as the σ (sigma) and in-plane contributions from the π-system is significant.[51] This has resulted in the original NICS now designated as NICS$(x)_{iso}$. (*iso* to show that the NICS is an isotropic shielding). Fowler and Steiner suggested an NICS index designated NICS$_{zz}$ which is based on the total contribution of the out-of-plane component of the NICS tensor.[52,53] However, this NICS index still suffer from contamination from the non-π contribution.

To assess the individual contributions to this NICS value, refined ("dissected") NICS methods were devised based on orbitals.[50,54] The first approach makes used of localized molecular orbitals(LMO) in which the dissection is inherent in the individual gauge for local orbital (IGLO).[55] The second approach is based on the gauge-including atomic orbitals (GIAO)[56] which provides individual canonical molecular orbitals (CMO) contributions to the NICS. The π contribution to the NICS can then be obtained using any of the two approaches.

One would expect that the new NICS, NICS$(0)_{\pi}$, would give a better measure of the aromaticity. However, Fallah-Bagher-Shaidaei et al.[57] debunked this notion, by insisting that the fact that this value is based on the isotropic magnetic shieldings indicates that the directionality associated with magnetic properties is not accounted for in this approach. This was later confirmed by Du et al.[58] who showed that the ring-current strength obtained from aromatic ring current shieldings (ARCS) fit of σ_{zz} tensor component are 2-4 times larger than those deduced from the isotropic shieldings. Rather, the more refined approach suggested by Fowler and Steiner,[51] which combines NICS$_{zz}$ with the dissection method and using either the IGLO or GIAO approach, designated NICS$_{\pi zz}$, gives a better measure of aromaticity.

Suggestions that the local and σ (sigma) effects may play different roles in different systems and that a single NICS value may lead to an erroneous conclusions led to aromatic ring chemical shielding (ARCS) model proposed by Jusélius and Sundholm.[59]

The ARCS model involves probing the nuclear magnetic shieldings in a set of points along a line perpendicular to the molecular plane and using the Biot-Savart law to obtain the current strengths. By using this approach they reported the relative degree of aromaticity of benzene, furan, pyrrole and other systems.[59] Similar approaches have also been used by Morao[60] and Bühl.[61] Stanger[62] in 2006 revisited the NICS scan approach, which he designated NICS$_{\text{-scan}}$. He postulated that it was possible to obtain the paratropic and diatropic contributions to the induced ring currents using this approach.

The NICS approach has the advantage over other magnetic criteria in that, it does not require a reference molecule, increment schemes or calibrating (homodesmotic) equation for evaluation. However, the NICS approach has difficulty in accurately determining the degree of aromaticity of a single molecular ring as well as providing a reliable current pathways in multiring systems.[58,59,63–71]

2.5 Current Density Analysis

The ring current model is dated back to the work of London[13] in 1937 who wrote of interatomic current and superconductivity of aromatic compounds. However, the term "ring current" was not used until in the 1950s when the ^{1}H NMR chemical shift phenomenon caused London's 1930s paper to receive much attention.

Pople[14] and McWeeny[15] by individually applying the molecular orbital theory, studied the ring currents in aromatic compounds. However, McWeeny reported that his approach produced results which differ somewhat from those obtained using Pople's approach.

The current density approach makes use of the fact that aromatic compounds sustain a net diatropic current and antiaromatic systems support a net paratropic ring current under the influence of an external magnetic field. It was Pople,[14] Coulson[72] and McWeeny[16] who began to devise means of calculating the intensity of the ring current(s).

With the advent of great computational power, the pictorial representation of the current density as well as the intensity of the current density can be computed. Hegstrom and Lipscomb[73] were the first to publish a current density map to analyze current in the 1960s. Ten years later, Atkins and Gomes[74] reported the current density profiles for benzene.

The computation of the intensity of current density and the pictorial representation of the current was saddled with the gauge-origin problem in magnetic shielding calculation. The gauge-origin problem arises as a result of the use of finite basis set or the use of finite number of grid point or both to represent molecular orbitals (MOs) in the calculation of second-order magnetic properties of molecules.[55,75,76] Two main approach have been devised to circumvent this problem, namely the individual gauge for localized orbitals (IGLO)[55] and the gauge-including atomic orbital (GIAO).[77] The IGLO approach uses individual gauge origins for the different localized molecular orbitals. The GIAO approach, on the other hand resolves the gauge-origin problem by choosing atomic basis functions such that they are dependent on the external magnetic field ($B_{external}$). This makes the calculation of the nuclear shielding tensor independent of the origin when using even minimal basis set.

The continuous transformation of current-density (CTOCD) approach[65,78,79] for computing current densities resolves the gauge origin problem by calculating the current density tensor using separate gauge origin for each point in space. Based on the point where the origin is positioned in the CTOCD framework, two variant forms exist; the Continuous Transformation of Current-Density-Diamagnetic set to Zero (CTOCD-DZ) and the Continuous Transformation of Current-Density-Paramagnetic set to Zero (CTOCD-PZ).[80–83] In the CTOCD-DZ approach, the gauge origin is identical to the point where the current density is computed whereas in the CTOCD-PZ approach the origin is chosen such that the transverse paramagnetic current density is annihilated. However, it has been shown[84] that current density calculation using the CTOCD schemes is less efficient as it yields current densities only at the coupled Hartree-Fock (CHF) and DFT level of theory, notwithstanding, only current strengths at the CHF level has been reported.[85] The studies at the CHF level of theory means that electron correlation which affects current-

density studies especially in open-shell systems is neglected.[86] Moreover, the CTOCD method has larger basis set errors than the GIAO approach.

The gauge including magnetically induced current (GIMIC) method[84,86] uses gauge including atomic orbitals (GIAOs) in calculating the magnetically induced current densities. The use of GIAOs removes the gauge-origin dependence of the current densities as well as improves the basis set convergence of the current density because the current density is to first order considered in the basis functions.

The GIMIC approach is formulated in the framework of analytical derivatives theory, enabling implementation at the Hartree-Fock self-consistent-field (HF-SCF) as well as electron correlated levels. GIMIC calculations require the one-electron unperturbed and perturbed density matrices, basis set information and the geometry data. This is obtained from an NMR shielding calculation. The GIMIC equation for calculation of the various components of the magnetically induced current-density tensor is

$$\mathrm{J}_{\upsilon}^{\mathrm{B}_\tau\kappa}(\mathrm{r}) = \sum_{\mu\nu} D_{\mu\nu}^{\kappa} \frac{\partial \chi_{\mu}^{*}(\mathrm{r})}{\partial \mathrm{B}_\tau} \frac{\partial \tilde{h}(\mathrm{r})}{\partial \mathrm{m}_{\upsilon}^{k}} \chi_{\nu}(\mathrm{r}) + \sum_{\mu\nu} D_{\mu\nu}^{\kappa} \chi_{\mu}^{*}\mathrm{r} \frac{\partial \tilde{h}(\mathrm{r})}{\partial \mathrm{m}_{\upsilon}^{k}} \frac{\partial \chi_{\nu}(\mathrm{r})}{\partial \mathrm{B}_\tau} + \sum_{\mu\nu} \frac{\partial D_{\mu\nu}^{\kappa}}{\partial \mathrm{B}_\tau} \chi_{\mu}^{*}(\mathrm{r}) \frac{\partial \tilde{h}(\mathrm{r})}{\partial \mathrm{m}_{\upsilon}^{k}} \chi_{\nu}(\mathrm{r}) - \epsilon_{\upsilon\tau\delta} \left[\sum_{\mu\nu} D_{\mu\nu}^{\kappa} \chi_{\mu}^{*}\mathrm{r} \frac{\partial^2 \tilde{h}(\mathrm{r})}{\partial \mathrm{m}_{\upsilon}^{k} \partial \mathrm{B}_\delta} \chi_{\nu}(\mathrm{r}) \right] \quad (2.23)$$

Here, B_τ is the external magnetic field and $\mathrm{m}_{\upsilon}^{k}$ is the nuclear magnetic moment. $D_{\mu\nu}^{\kappa}$ and $\frac{\partial D_{\mu\nu}^{\kappa}}{\partial \mathrm{B}_\tau}$ are elements of the density matrix and the magnetically perturbed density matrices of α and β electrons respectively. $\frac{\partial^2 \tilde{h}(\mathrm{r})}{\partial \mathrm{m}_{\upsilon}^{k} \partial \mathrm{B}_\tau}$ and $\frac{\partial \tilde{h}(\mathrm{r})}{\partial \mathrm{m}_{\upsilon}^{k}}$ describe the coupling between the external magnetic field and the nuclear magnetic moment. $\epsilon_{\upsilon\tau\delta}$ is the Levi-Civita permutation tensor and χ_ν denotes the basis function used.

Equation 2.23 can be reformulated in vector notation as

$$\mathrm{J}_{\alpha}^{B_\beta} = \mathbf{v^T P}_\beta \mathbf{d}_\alpha - \mathbf{b}_\beta^{\mathbf{T}} \mathbf{D d}_\tau + \mathbf{v^T D q}_{\alpha\beta} - \epsilon_{\alpha\beta\gamma} \frac{\mathbf{1}}{\mathbf{2}} (\mathbf{v^T D v}) \mathrm{r}_\gamma \quad (2.24)$$

where $\mathbf{D}$ is the atomic orbital (AO) density matrix, $\mathbf{P}_\alpha$ is the perturbed AO density matrices, $\mathbf{v}$ is the basis set vector, $\mathbf{r}_\gamma$ is the grid point, $\epsilon_{\alpha\beta\gamma}$ is the Levi-Civita tensor and the basis set derivatives $\mathbf{b}_\alpha$, $\mathbf{d}_\alpha$, $\mathbf{q}_{\alpha\beta}$ given by

$$\mathbf{b}_\alpha = \frac{\partial \mathbf{b}}{\partial \mathbf{B}_\alpha} \quad (2.25)$$

$$\mathbf{d}_\alpha = \frac{\partial \mathbf{v}}{\partial \mathbf{r}_\alpha} \tag{2.26}$$

$$\mathbf{q}_{\alpha\beta} = \frac{\partial^2 \mathbf{b}}{\partial \mathbf{r}_\alpha \mathbf{B}_\beta} \tag{2.27}$$

and $(\alpha, \beta = x, y, z)$ The density matrices $\mathbf{D}$ and $\mathbf{P}_\alpha$ are obtained from standard *ab initio* and DFT program packages capable of calculating nuclear magnetic shielding tensors.

A unique feature of the GIMIC approach is its ability to quantify the value of the induced current by integrating the current flow along selected bonds. For instance, by using the GIMIC approach Jusélius et al.[86] reported the induced ring current of benzene to be 11.4 nAT^{-1} at the CCSD(T) level using the TZP basis set. GIMIC has been used to study the aromaticity of various compounds including polyaromatic hydrocarbons (PAHs),[87] porphyrinoids,[88] , Möbius-twisted molecules,[89] and some inorganic species such as Al_4^{2-} and Al_4^{4-}.[90]

The GIMIC approach has proven very useful for determining the current susceptibility as well as the electron delocalization pathways in multiring systems where other methods are prone to fail.[84] GIMIC has also provided a non-invasive method for estimating the individual hydrogen bond strength in molecules.[91] GIMIC is currently interfaced to Turbomole[92,93], Cfour[94], Gaussian[95] and QChem[96] for the studies of current densities using GIAOs

Although the current density approach looks promising, it however requires some special expertise to be able to use. More so, since most current density analysis packages comes as stand-alone programs, they are not readily available for use.

3. PHOTOPHYSICAL PROPERTIES

3.1 Introduction

Electromagnetic radiation is known to exist as a particle as well as a wave. Electromagnetic radiation consist of an oscillating magnetic and electric field perpendicular to each other which travels through vacuum. Electromagnetic waves are characterized by frequency ν, which is inversely proportional to the wavelength λ, by the equation

$$\nu = \frac{\lambda}{c} \tag{3.1}$$

where c is the speed of light. Photons are the elementary particles of the electromagnetic radiation. Photons have energy (E) which is related to the frequency of the electromagnetic radiation (ν) and the Planck's constant (h)

$$E = h\nu \tag{3.2}$$

The total energy of a molecule, also referred to as the molecular energy state is the sum of the translational, vibrational, rotational, nuclear and electronic energy of the molecule. When a photon of an electromagnetic radiation interact with a molecule, the energy of the photon can be transferred to the different molecular energy levels lifting the molecule to a different energy level. The molecular energy levels of the molecule are quantized. This means that the energy transferred by the photon to the molecule would only be absorbed if the energy of the photon is equal to the energy difference between any two states. This phenomenon is the underlying principle of molecular spectroscopy. Table (3.1) summarizes the wavelengths of the electromagnetic spectrum and the spectroscopic processes that occur in each region.

	Wavelength(nm)	Spectroscopic process
Ultraviolet	200-300	Electronic
Visible	400-700	
Infrared	1000-10000	Vibrational
Microwave	10^7 -10^9	Rotational
Radio wave	10^{11}	NMR

Table 3.1: Spectroscopic processes and the range of the electromagnetic radiation where they occur

3.2 The Jablonski Diagram

The absorption of a photon of UV-Vis radiation results in an excited electronic state of the molecule. In the transition to an excited state, an electron can be considered to be promoted from a lower energy orbital such as the HOMO (highest occupied molecular orbital), to an unoccupied orbital, e.g., the LUMO (lowest unoccupied molecular orbital). The various photophysical processes that occur when a molecule absorbs a photon of UV-Vis radiation is summarized by a Jablonski[97] diagram. The Jablonski diagram is an energy diagram that illustrates the electronic states of a molecule and the transitions between them. Figure (3.1) shows a modified Jablonski diagram where the energy surface is represented by a Morse potential with the vibronic state in each of the different electronic states and the photophysical processes associated with them.

3.2.1 Absorption

According to the Stark-Einstein law, when a molecule is exposed to radiation of appropriate frequency, only a single photon of light whose energy is generally the energy difference between the ground and excited state will be absorbed to bring about excitation. However, in the presence of strong laser fields, two-photon absorption (TPA) can also be achieved. Two-photon absorption involves the simultaneous absorption of two photons of identical or different frequencies in order to excite a molecule from one state (usually the ground state) to a higher energy electronic state.[99,100] The excitation occurs between

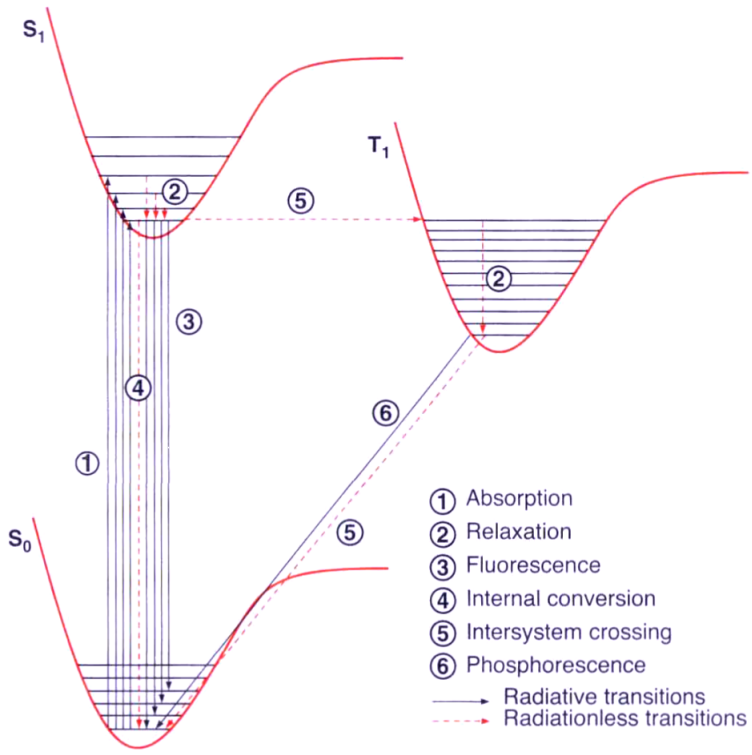

Figure 3.1: An example of a Jablonski diagram[98]

the ground state, S_0, and the lowest excited states S_1, S_2, S_3, and few others.

The absorption of a photon leads to an excitation from the ground state to an excited state. The electronic transition process follows the Franck-Condon principle.[101] The Franck-Condon principle describes how the intensity of the transition between vibrational levels of different electronic excited states as shown in Figure 3.1 is proportional to the square of the overlap integral between the vibrational wavefunctions of the two states that are involved in the transition. Classically, the Franck-Condon principle is the approximation that an electronic transition is most likely to occur without changes in the positions of the nuclei in the molecular entity and its environment. The resulting state is called a Franck–Condon state, and the transition involved is called a vertical transition.[102] In a simple orbital picture, an electron in the highest occupied molecular orbital (HOMO) can be considered excited to the lowest unoccupied molecular orbital (LUMO). These orbitals may be bonding, nonbonding or antibonding orbitals. Antibonding orbitals are often labelled with an asterisk (*). Chemists have assigned notations for the

orbitals from which the electron departs and where it lands during the absorption and excitation process. For instance, when an electron is excited from a π molecular orbital to π* molecular orbital, it is referred to as π-π* transition and such a molecule is said to be in the π-π* state. When an electron in a non-bonding molecular orbital n, is excited to any of the antibonding molecular orbital π* and σ*, an n-π* and n-σ* transitions are achieved, respectively. The various transitions and the wavelength which results in such transitions for some selected functional groups and their molar absorption coefficients are shown in Table (3.2). Generally, the n-π* and π-π* are the most important transitions in organic photochemistry.

At ambient temperatures, the excitation process takes place from the lowest vibrational level, which has the highest population, to any of the vibrational levels in the excited state. This results in the vibronic bands which are sometimes observed in the absorption spectra of molecules in the gas phase as well as in solution for prophyrin molecules. These vibronic bands are what give rise to the broad absorption spectrum observed in the UV-Vis spectrum of some molecules which centers around the wavelength of the major transition in addition to other weak bands.

Functional groups or a set of functional groups responsible for the absorption of photons are referred to as chromophores. Sometimes the word "chromophore" is used to refer to the whole molecules which contains these functional groups. There are generally two classes of chromophores; the π, π* and the n, π*. The π-π* transitions are said to be symmetry allowed and give very intense absorption band(s) as a result of their very large molar absorption coefficients. The n-π* transitions have smaller molar absorption coefficients and are said to be symmetry forbidden. Different chromophores have different maximum wavelength of absorption, λ_{max} which are affected by the environment of the chromophore as well as the environment or solvent in which the absorption of compound is studied. A shift of the absorbance to a longer wavelength is referred to as bathochromic or red shift whereas a shift to shorter wavelength is referred to as hypsochromic or blue shift. In some cases, the absorbance or intensity of the absorption is increased or decreased, which is referred to as hyperchromic or hypochromic shifts respectively.

Functional group	Type of transition	Molar absorption coefficient(ϵ)/Lmol^{-1}cm	λ_{max}(nm)
C-C	$\sigma \rightarrow \sigma$*	< 180	1000
C-O	$n \rightarrow \sigma$*	~ 180	200
C=C	$\pi \rightarrow \pi$*	180	10000
C-Br	$n \rightarrow \sigma$*	208	300
C-I	$n \rightarrow \sigma$*	260	400
C=O	$n \rightarrow \pi$*	280	20
N=N	$n \rightarrow \pi$*	350	100
C_6H_6	$\pi \rightarrow \pi$*	260	200
C=C-C=C	$\pi \rightarrow \pi$*	220	20000

Table 3.2: Some functional groups and the characteristic transitions observed

The rate of absorption is given by the Beer-Lambert law. The law states that the amount of radiation absorbed is proportional to the number of molecules absorbing the radiation (that is the concentration, c, of the absorbing species). Mathematically, the law is stated as

$$A = \epsilon bc \tag{3.3}$$

where A is the absorbance, b is the path length and c is the concentration. ϵ is a constant of proportionality referred to as the molar absorption coefficient. UV-Vis spectrum which shows a plot of the absorbance verses wavelength are experimentally obtained using a UV-Vis spectrophotometer.

3.2.2 Vibrational Relaxation and Internal Conversion

When a molecule is excited from the ground state, the molecular system has excess energy, and in order for the system to be stabilized, it loses some of its energy through structural relaxation and non-radiative processes. Two of such non-radiative processes are internal conversion and vibrational relaxation.

Vibrational relaxation occurs when the molecule gives away energy as heat as a

result of the increase in the kinetic energy of the molecules. The dissipated energy may be transferred to the surrounding molecules or stay in the molecule. Vibrational relaxation is a very fast process, occurring almost simultaneously during the absorption of a photon. The typical rates of vibrational relaxation is $10^{11}s^{-1}$-$10^{12}s^{-1}$.[98]

During internal conversion, the dissipation of the energy occurs between the vibrational states of the different electronic states. Internal conversion occurs as a result of overlap of vibrational and electronic energy states.[98] Although internal conversion occurs between different electronic energy states of the same spin multiplicity, the process can be as fast as vibrational relaxation. However, due to a lack of vibrational and electronic energy state overlap and a large energy difference between the ground state and first excited state, internal conversion is a very slow means for an electron to return to the ground state.

3.2.3 Fluorescence

When an electron is excited to the higher energy state, the energy can also be dissipated by emission of radiation so that the system return to a lower energy state. Fluorescence is one of the radiative means by which the system returns to a lower energy state, as shown in Fig. 3.1. Fluorescence is often observed between the first excited state and the ground state of a molecule. This is attributable to the Kasha's rule[103], as during de-excitation the first excited state is the most likely state for the excited electron to be found. Fluorescence is generally a slow process in comparison with vibrational relaxation. The typical rates of fluorescence is $10^{7}s^{-1}$-$10^{9}s^{-1}$. Though a slow process, the conservation of the spin state of the electron during the transition makes it a spin allowed transition. Also, for any emitted light to be detected, the internal conversion processes must be slower than fluorescence for any given molecule.

Fluorophores are chromophores analogues responsible for fluorescence in molecules. As fluorescence involves the emission of photons, one would expect that the energy of the absorbed photon is what would be emitted. Thus, in an ideal situation the absorption spectra and emission spectra would be the same. However, due to the different radiative and radiationless processes such as vibrational relaxation that occur in the molecule

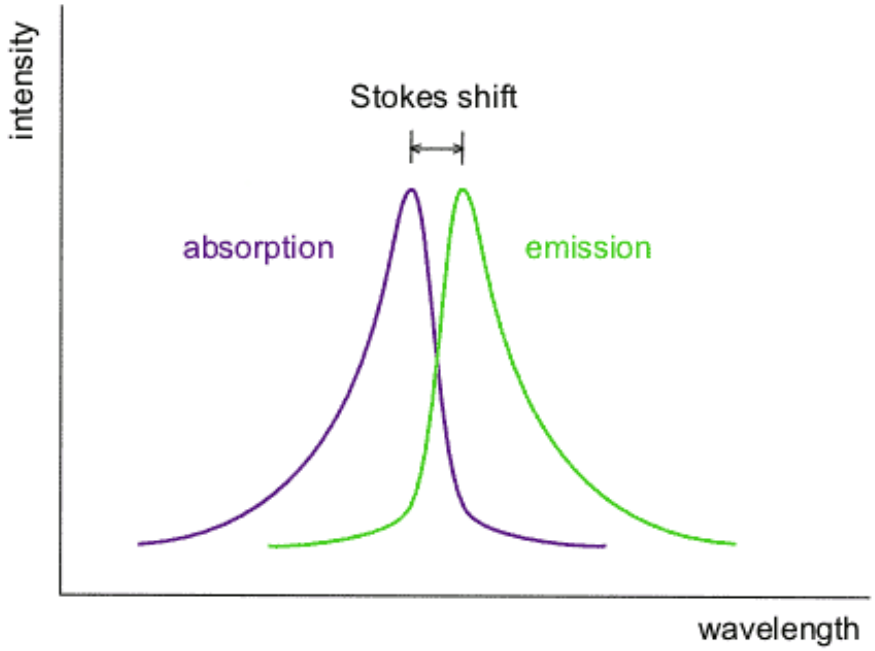

Figure 3.2: Stokes shift

and structural relaxation effect, some of the absorbed energy is lost through such processes and the emitted photons and thus the emission spectra occurs at longer wavelength (lower energy). Since the potential energy surface (PES) is different for the excited state as compared to the ground state (upper and lower state), the fluorescence spectra is red-shifted in comparison to the absorption spectra. When the PESs do not differ significantly, there exists a mirror image relationship between the absorption and emission spectra. The difference observed between the maximum wavelength of absorption spectra and emission spectra is referred to as the Stokes shift (Figure 3.2). Notwithstanding the fact that emission of photons usually occurs from the lowest vibrational level of the first excited state S_1 to S_0, in rarer cases emission occurs from the higher excited state S_2 to S_1. Such emissions are referred to as anomalous fluorescence.

Generally, molecules will return to their ground electronic state by the fastest route. However, several de-excitation channels can be activated. Fluorescence in molecules is observed only if it is a more efficient means of de-excitation than the combination of vibrational relaxation and internal conversion. Fluorescence quantum yield (ϕ_f) is the measure of the fraction of excited molecules returning to the ground state by fluorescence.

Fluorescence is generally observed for molecules where the lowest energy absorption is a π-π* transition although some n-π* transitions show weak fluorescence.[104]

3.2.4 Intersystem Crossing and Phosphorescence

Intersystem crossing is a radiationless process which involves a transition between two electronic states with different spin multiplicity. In intersystem crossing, there is a change of spin during the radiationless transition. Although this is a spin forbidden transition, intersystem crossing is enhanced by two factors: a very similar molecular geometry in the excited singlet and triplet states, and a strong spin-orbit coupling, which allows the spin-flip associated with a singlet–triplet transition to occur.[105]

Spin-orbit coupling arises from the special theory of relativity and is greater for heavier atoms because the velocity of the $1s$ electrons in such atoms can go nearly as fast as the speed of light. In such situation an electron in each orbital does not have a well-defined spin. Thus, a pure singlet, doublet or triplet state is not completely observed. This makes the radiative (phosphorescence) and non-radiative (intersystem crossing) transitions weakly allowed.

The conversion of an excited triplet state to a singlet state accompanied by the emission of a photon is termed phosphorescence. The population of the triplet excited state is enhanced by intersystem crossing, as usually a transition from the ground singlet state S_0 to a triplet excited state T_1 is a spin forbidden transition. The population of the electrons which are found in the triplet excited state then return to the ground state accompanied by the emission of a photon in phosphorescence. The forbidden nature of phosphorescence makes it a much slower process compared to fluorescence. The typical rates of phosphorescence is $10^{-2}s^{-1}$-$10^{3}s^{-1}$. The slow rate of phosphorescence is responsible for the glow that is observed after the excitation source is removed. Phosphorescence is more favoured in molecules that have n-π* transitions than π-π* as the former have a higher probability for intersystem crossing to occur. Phosphorescence emission occur at a longer wavelength than that of fluorescence emission as well as absorption. This is because the T_1 state is usually below S_1, and intersystem crossing is always downward in energy.

3.3 Optical Spectroscopy of Porphyrinoids

It was known early that the deeply coloured nature of porphyrins and porphyrin derivatives was as a result of their highly conjugated π-electron systems. Porphyrins and porphyrin derivatives such as carbaporphyrinoids have characteristic absorption spectrum of very intense sharp absorption band in the 380 -500 nm range of the UV-Vis spectrum, the so called Soret or B-band and weak absorption bands in the 500 -750 nm range of the visible spectrum, the so called Q-bands.(Figure 1.3)

However, theoretical studies and explanation for the absorption process was not understood until in the 1960s when Gouterman[106] proposed the four-orbital model to explain the absorption spectra of porphyrins. According to this model, the absorption spectrum of porphyrins results from the transitions between two HOMOs and two LUMOs. The HOMOs and LUMOs were found to be a_{1u}, a_{2u} and a degenerate set of e_g orbitals respectively. These transitions between orbitals give rise to two excited states. Orbital mixing causes the two energy states to split creating a higher energy state with larger oscillator strength. This accounts for the Soret band and the lower energy state with a smaller oscillator strength is responsible for the Q-bands.[107] However, in the less symmetric (D_{2h}) case, four excited states are observed, whereas, in the symmetric (D_{4h}) case, such as magnesium porphyrin, two doubly degenerate excited states result from the transition between the orbitals.

Gouterman also showed that changes in conjugation pathway and symmetry of the porphyrins as well as the metal which the porphyrin binds in metalloporphyrins could affect the UV-Vis absorption spectrum, resulting in a red-shift of the B and Q-bands.[106] The absorption spectrum of porphyrins as well as porphyrin derivatives results from a $\pi \rightarrow \pi^*$ transition of the conjugated π system. However, further studies of the fluorescence spectroscopy of porphyrins have shown that there is also an $n \rightarrow \pi^*$ transition at about 630 nm.[108]

3.4 Computational Approach for Excited States

The Hartree-Fock approximation[109–111] uses a Slater determinant (SD) as the ansatz for the antisymmetric wavefunction.[112] However, the exact wavefunction cannot be expressed as a single determinant. This is because a single Slater determinant does not account for Coulomb correlation which describes the correlation between the spatial position of electrons due to Coulomb repulsion. This results in the Hartree-Fock energy (E_{HF}) being greater than the 'exact' energy for a given basis set. The exact energy is the solution to the Schrödinger equation (Equation 3.4) in the basis set used for the Hartree-Fock calculation.

$$H|\Psi\rangle = E|\Psi\rangle \tag{3.4}$$

Here, H is the Hamiltonian of the system, $|\Psi\rangle$ is the exact wavefunction and E is the ground state energy. The difference between the HF energy and the exact non-relativistic energy is referred to as the correlation energy, a term coined by Löwdin.[113]

$$E_{correlation} = E_{exact} - E_{HF} \tag{3.5}$$

Electron correlation is sometimes classified as dynamical and non-dynamical (static) correlation.[114,115] Dynamical correlation accounts for the effect of the instantaneous repulsion between all the electrons in a system whereas static correlation refers to the phenomenon where multiple determinants are required to describe the coarse electronic structure of a system.

In computational studies on excited states, electron correlation plays an important role. This implies that *ab initio* methods which account for electron correlation are required rendering the studies of excited states problematic and non-trivial. Additionally, choosing a good basis set for the computation is crucial. For instance, for excited states with Rydberg character, basis set augmented with diffuse function is needed.

In recent years, a large number of computational methods have been developed for the studies of excited state including easy-to-apply methods such as configuration interaction (CI), coupled-cluster methods (CC), Møller-Plesset perturbation theory[116] and time-dependent density functional theory (TDDFT).[117,118] More complicated methods

based on multiconfigurational self-consistent field approach such as multireference configuration interaction (MRCI), complete active space self-consistent field (CASSCF), complete active space perturbation theory (CASPT2),[119] restricted active space self consistent field (RASSCF)[120] are also used.

3.4.1 Configuration Interaction

The configuration interaction is a post-Hartree-Fock linear variational method for approximately solving the non-relativistic Schrödinger equation for a quantum chemical multi-electron system. The Hartree-Fock approximation uses an average potential to account for the electron-electron interaction. However, in real systems, the interaction between electrons do not occur in an average manner. This results in a higher Hartree-Fock energy.

The configuration interaction (CI) is based on the fact that the Hartree-Fock wavefunction can easily be computed. As a result, the electron correlation can be accounted for by including terms that represent the electronic configuration in different states, such as promotion of an electron from an occupied to virtual molecular orbital in the construction of the Slater determinant for the wavefunction. Thus, the wavefunction for the configuration interaction is a combination of the wavefunctions obtained for the Hartree-Fock determinant and the determinant for different orbital configuration.

$$\Psi_{CI} = a_0\phi_{SCF} + \sum_{Singles(S)} a_s\phi_s + \sum_{Doubles(D)} a_D\phi_D + ... = \sum_{i=0}^{n} a_i\phi_i \tag{3.6}$$

By using this approach, the wavefunction and the electronic structure of the system conceptualize a state in which the electrons interact with each other as a result of the mixing of the different electronic configurations. Various forms of CI exist based on the number of excitations used in constructing the CI wavefunction. For instance, if the single (S) and double (D) excitations are used, it is designated as CISD. When all excitations are used, a full configuration interaction (FCI) is obtained. However, full configuration interaction is seldom used due to the high computational cost involved. Implementation of CI is mostly truncated to the single and double excitations.

The use of CI is problematic because the relative importance of a configuration

changes across the potential energy surface. Moreover, truncated CI methods are neither size-extensive nor size-consistent and do not scale well with the system size.[121]

3.4.2 Coupled-Cluster Theory

The coupled-cluster theory was initially developed by Coester and Kümmel[122] in 1960 to solve the nuclear binding energies in nuclear physics. It was then reformulated by Cižek[123] in 1966 and later by Paldus et al.[124] in 1972 for handling electron correlation effects in atoms and molecules. The method became the method of choice for handling the electron correlation problem by a large part of the scientific community when Bartlett[125] in 1978 implemented for the first time an efficient method to solve the coupled-cluster equations providing as exact solution to the Schrödinger equation (Equation 3.4) as possible.

The coupled-cluster wavefunction is given by the exponential ansatz

$$|\Psi\rangle = e^T|\Phi_0\rangle \tag{3.7}$$

where $|\Phi_0\rangle$ is the reference wavefunction, which is typically a Slater determinant obtained from Hartree-Fock molecular orbitals. Wavefunctions constructed from configuration interaction, multi-reference self consistent field may also be used as a reference wavefunction. The multireference CC methods are, however, complicated and will not be discussed here. T, the cluster operator, is written in the form $T = T_1+T_2+T_3+...$ where T_1 is the operator for single excitations, T_2 is the operator for all double excitations and so forth. Combining Equation 3.4 and 3.7, the Schrödinger equation in the coupled-cluster approach is expressed as

$$H|\Psi\rangle = He^T|\Phi_0\rangle = Ee^T|\Phi_0\rangle \tag{3.8}$$

The ansatz does not forbid a variational solution, however, the similarity transformation of the Hamiltonian leads to a non-variational method. The exponential operator e^T may be expressed as a Taylor series

$$e^T = 1 + T^1 + \frac{T^2}{2!} + \frac{T^3}{3!} + ... \tag{3.9}$$

Considering only T_1 and T_2 of the cluster operator, Equation 3.9 can be expressed as

$$e^T = 1 + T_1 + T_2 + \frac{1}{2}T_1^2 + T_1T_2 + \frac{1}{2}T_2^2 + ... \tag{3.10}$$

In practical calculations, the excitations used in the cluster operator are truncated and based on the highest number of excitations considered, various forms of coupled-cluster are implemented. For instance, when only single (S) and double (D) excitations are considered, the designation CCSD is used. Coupled-cluster methods considering triple (T) and quadruple (Q) excitations are sometimes used. To save computational cost, the highest excitation, may be treated using perturbation theory. For instance, at the CCSD(T) level, the triple excitations are treated perturbationally.

The coupled-cluster theory formulated using either linear-response,[126] equation-of-motion,[127,128] state-universal multi-reference coupled-cluster[129] or valence-universal multi-reference coupled-cluster[130] can be used for performing calculations on excited state systems. Coupled-cluster is considered the de-facto standard of modern *ab initio* quantum chemistry, however, its computational expensiveness makes it applicable to small and medium-size systems only.

The second-order approximate coupled-cluster singles and doubles model (CC2)[131] has become the most widely used approach for the study of excited states of biomolecules and other larger systems. The CC2 is an approximation to the CCSD approach. Here, the equation for the double excitations are approximated such that it becomes similar to that of the single excitations. The equations for the singles are however retained and provides an approximate description of the orbital relaxation. The energy of the CC2 approach is analogous to the MP2. The excitation amplitudes are obtained by solving the CC2 equation. The CC2 calculation scales as N^5, where N is the number of orbitals. The hierachy of the scaling behaviour for the coupled-cluster approach is CCS(N^4), CC2(N^5), CCSD(N^6), CC3(N^7), CCSD(T)(N^7), CCSDT(N^8) etc.

3.4.3 Many-Body Perturbation Theory

The many-body perturbation theory is an *ab initio* method for accounting for the electron correlation as a perturbation to the Hartree-Fock wavefunction. In this approach, the

Hartree-Fock wavefunction is used as the reference system. By considering a perturbation $\hat{V}$ to the reference or unperturbed Hamiltonian $\hat{H}_0$, the Hamiltonian $\hat{H}$ of the system can be written as

$$\hat{H} = \hat{H}_0 + \lambda\hat{V} \tag{3.11}$$

Here λ is an arbitrarily parameter which determines the extent of the perturbation to the unperturbed system. Thus, the electron correlation term is obtainable from the perturbation term. When the perturbation is very small, it is possible to expand the Hamiltonian of the system as a Taylor series in terms of the parameter λ

$$\hat{H} = \hat{H}^{(0)} + \lambda\hat{H}^{(1)} + \lambda^2\hat{H}^{(2)} + \dots \tag{3.12}$$

The wavefunction and energy can be expressed as

$$\psi_n = \psi_n^{(0)} + \lambda\psi_n^{(1)} + \lambda^2\psi_n^{(2)} + \dots \tag{3.13}$$

$$E_n = E_n^{(0)} + \lambda E_n^{(1)} + \lambda^2 E_n^{(2)} + \dots \tag{3.14}$$

The powers of the parameter λ describe the order of the perturbation so that for the unperturbed system, the order of the perturbation is said to be zeroth-order. In practice, the expression is truncates at the second, third or higher level perturbation terms. However, it has been shown that generally higher order terms beyond the third order do not improve the correlation energy. In some cases the MP series might diverge.[132]

In most standard *ab initio* quantum chemistry program, the correction to the second order is mostly used. It is a common convention to refer to them as MPX, where X refers to the order of the perturbation and MP for the publishers of the main idea, Møller and Plesset.[116] The approach is sometimes referred to as Møller-Plesset perturbation (MP) theory. MP theory is computationally more efficient than the CI approach. However, the method is not variational and at any order, the energy obtained may be above or below the actual energy. MP theory has the advantage of been size-consistent.

3.4.4 Multiconfigurational SCF (MCSCF) and Complete Active Space SCF (CASSCF)

In multiconfigurational self-consistent field theory, the wavefunction is written as a linear combination of different Slater determinants (configuration state function), ϕ_I, of different electronic configuration as in the CI method.

$$\Psi_{MCSCF} = \sum_{I}^{CI} c_I \phi_I \tag{3.15}$$

In this approach the molecular orbitals are determined by minimizing the MCSCF energy. In general, the MCSCF calculation involves specifying which MO would be occupied in the configuration state functions. The selection of which MO to include in the configuration state functions, the so called active space can be esoteric as the selection of which set of orbitals and electrons to use are directly related to the chemistry to be described.

In the complete active space self-consistent field (CASSCF), all configurations obtained by exciting the active electrons among the active orbitals are used in the MCSCF procedure. It is also possible to use the MCSCF wavefunction as the reference wavefunction for other approaches such as CASSCF perturbation theory, where the CASPT2 method is implemented in many *ab initio* quantum chemistry programs, or in multireference configuration interaction (MRCI) where configuration interaction approach is used with MCSCF as the reference wavefunction.

3.4.5 Time-Dependent Density Functional Theory (TDDFT)

Though DFT is not strictly an *ab initio* method, its inclusion here is justified by the fact that in its extended form, the TDDFT is widely used in excited state calculations. The time-dependent density functional theory is based upon the time-dependent Schrödinger equation

$$i\hbar\frac{\partial}{\partial t}\Psi(r,t) = \hat{H}\Psi(r,t) \tag{3.16}$$

which describes the evolution of a system with time.

The formalism for TDDFT is based on the Runge-Gross theorem.[133] The Runge-Gross theorem states that for a many-body system evolving from a given initial wave-

function, there exists a one-to-one mapping between the potential (or potentials) in which the system evolves and the density (or densities) of the system.[134] According to this theorem, the densities $\eta(r,t)$ and $\eta'(r,t)$ evolving from a common initial state, under the influence of two external potentials $v_{ext}(r,t)$ and $v'_{ext}(r,t)$ which differ not only in the time variable t, but also in r are always different. By using this theorem, Runge and Gross[133] used three different schemes; a set of hydrodynamical equations, a stationary action principle and an effective single-particle Schrödinger equation to calculate the density.

The linear response formalism is one of the common applications. In this approach, the external time-dependent potential is considered to be very small and is treated as a perturbation to the system. Perturbation theory is then used for determining the behaviour of the system instead of solving the Kohn-Sham equation.

TDDFT has proven useful in predicting the absorbance spectra of several systems[135–137], the calculation of the vibronic structure of electronic absorption spectra[138,139] and electronic dichroism spectra.[140] It is also computationally more efficient and scales better than other *ab initio* methods. However, charge transfer problems, Rydberg excited states, and conical intersections are not well described at the TDDFT level using currently available functionals.

4. COMPUTATIONAL STUDIES

4.1 Computational Methods

The calculations were performed using version 6.6 of the Turbomole program package.[92,93] All molecular structures were optimized at the density functional theory (DFT) level using the Becke-three-parameter functional combined with the Lee-Yar-Parr exchange-correlation functional (B3LYP)[141,142]. The Karlrushe triple-ζ basis set (def2-TZVP) was used for all atoms. Frequency analysis was done by using the AOFORCE module of Turbomole. The frequency calculations showed that all vibrational frequencies are real indicating that all the structures were energy minima on the potential energy surface. The NMR shielding calculations were performed with the MPSHIFT module of Turbomole[143,144] using the same basis set and level of theory as used for the geometry optimization. ^{1}H NMR and ^{13}C NMR chemical shifts calculated at the B3LYP/def2-TZVP level have proven to be close to the basis set limit and agree qualitatively with experimental data for organic molecules.[145] Recent studies have shown that the effect of the semi-empirical dispersion correction (D3) on the optimized structures and the NMR shielding calculation for the studied porphyrinoids is negligible.[146] The ring-current strengths and the visualization of the current flow which is obtained as the signed modulus of the magnetically induced current density was also calculated at the B3LYP/def2-TZVP level of theory using the GIMIC program package.

The excitation energies of the lowest singlet states were calculated at the linear-response time-dependent density functional theory (TDDFT) level using the B3LYP functional[141,142] and at the second-order approximate coupled-cluster (CC2) level using the frozen core and resolution of the identity (RI) approximations.[131,147,148] The Karlrushe

triple-ζ basis set (def2-TZVP) was used for all atoms.

4.2 Nomenclature and Molecular Structures

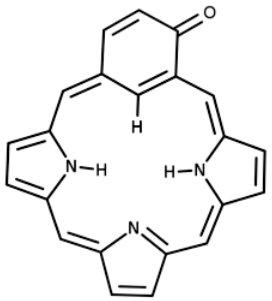

(a) Oxybenziporphyrin **1**

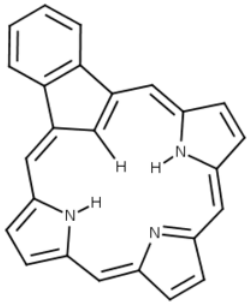

(b) Benzocarbaporphyrin **2**

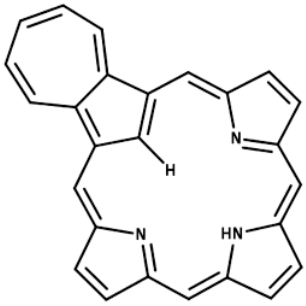

(c) Azuliporphyrin **3**

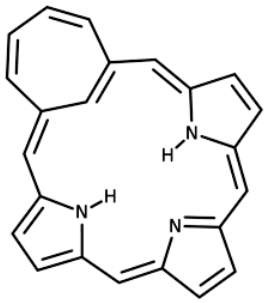

(d) Tropiporphyrin **4**

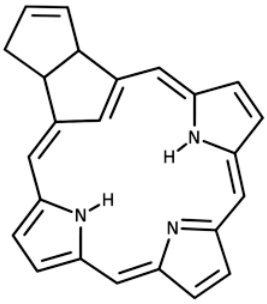

(e) Carbachlorin **6a** (*trans*)

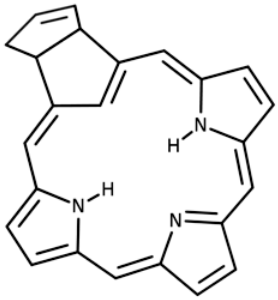

(f) Carbachlorin **6b** (*cis*)

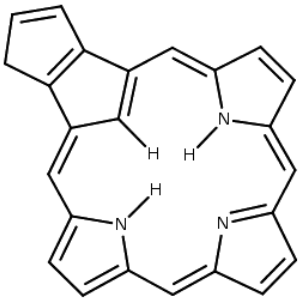

(g) Carbaporphyrin **9**

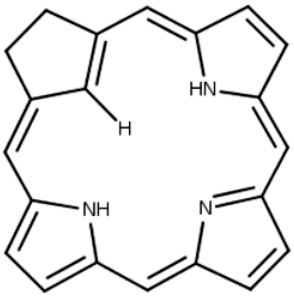

(h) Carbachlorin **11**

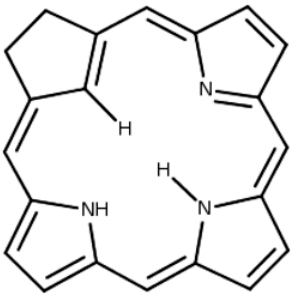

(i) Carbachlorin **11′**

The molecules selected for this study are carbaporphyrinoids and carbachlorins recently synthesized by Li and Lash.[36] The alkyl substituents have however been omitted to save computational cost as previous studies have shown that they do not significantly affect the current strengths and current pathways of porphyrinoids.[149] Labeling of the molecular structures follow that in Ref 36, this is to enable comparison of the obtained results

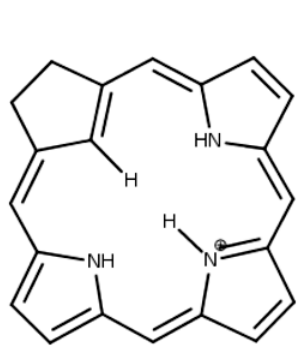

(j) Carbachlorin **11H**$^+$

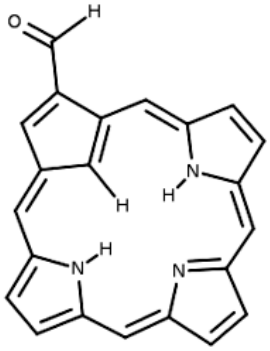

(k) Carbaporphyrin **14**

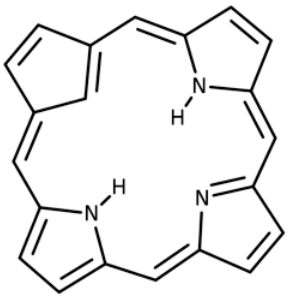

(l) Carbaporphyrin **20**

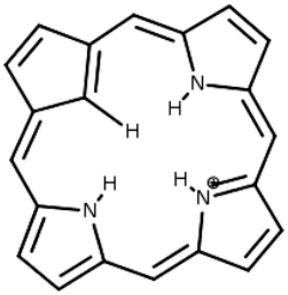

(m) Carbaporphyrin **20H**$^+$

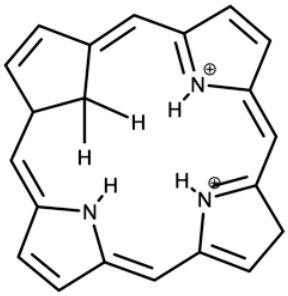

(n) Carbaporphyrin **20H**$_2^{2+}$

Figure 4.1: The molecular structure of the studied carbaporphyrinoids

with those in the said publication.

Carbaporphyrin **20** shown in Figure 4.1l is the simplest carbaporphyrin without any substituents. Carbaporphyrin **20H**$^+$ (Figure 4.1m) and **20H**$_2^{2+}$ (Figure 4.1n) are the singly and doubly protonated form of carbaporphyrin **20**, respectively. Carbaporphyrin **20H**$_2^{2+}$ has 5 inner hydrogens, two of which saturate the inner path of the cyclopentadienyl ring.

Carbachlorin **11** (Figure 4.1h) is the most simple carbachlorin with a saturated C_β-C'_β bond of the cyclopentadienyl ring and without any substituents. Carbachlorin **11** lacks an inner hydrogen in the *trans* position to the cyclopentadienyl ring, whereas carbachlorin **11′** (Fig. 4.1i) is the *cis* tautomer of **11**. Carbachlorin **11H**$^+$ (Figure 4.1j) is the prontonated form of **11** with four inner hydrogens.

Carbachlorin **6a** and **6b** are propencarbachlorins. Carbachlorin **6a** (Figure 4.1e) has a propene moiety which binds to the cyclopentandienyl ring of the carbachlorin moiety.

It is possible for the binding of the propene moiety to occur in a *trans* or *cis* manner, giving raise to the *cis* **6a** and *trans* **6b** shown in Figure 4.1f and Figure 4.1e, respectively.

Carbaporphyrinoid **9** which is shown in Figure 4.1g, could in principle be obtained by the oxidization of carbachlorin **6**, however, Li and Lash reported that this is not experimentally feasible.

Compounds **1-4** are modified carbaporphyrinoids. In oxybenziporphyrin **1** (Figure 4.1a), the cyclopentadienyl subring is replaced by a cyclohexadien-1-one ring. In benzocarbaporphyrin **2** (Figure 2.1), a benzene ring is fused to the cyclopentadienyl moiety, whereas in azuliporphyrin **3** (Figure 4.1c), a cycloheptatriene ring is fused to the cyclopentadienyl ring. Tropiporphyrin **4** (Figure 4.1d) has the cyclopentadienyl moiety substituted by a cycloheptatriene ring.

4.3 Current Density and Aromaticity

The aromaticity of the studied carbaporphyrinoids has previously been assessed by recording NMR spectra and by performing calculations of NICS values.[36] However, it is nowadays a well known fact that aromaticity studies based on these criteria are not reliable.[58,63–65,69,70]

In this study, the more definitive current density analysis using the GIMIC approach has been adapted for the study of the aromatic properties of the carbaporphyrinoids. The GIMIC approach has the advantage of giving the ring-current strengths and the current densities. The ring-current strengths are obtained by the integration of current flow along selected bonds.

The current density calculations show that all the studied carbaporphyrinoids are aromatic according to the ring current criterion. However, the ring-current pathways obtained in the GIMIC calculations differ from those predicted by the studies of Li and Lash.[36] They predicted an aromatic pathway based on the classical 18π aromaticity pathway.

4.3.1 Carbaporphyrin 20, $20H^+$ and $20H_2^{2+}$

The net current strength calculated for carbaporphyrin **20** is 26.8 nAT^{-1}. The current splits almost equally at the pyrrolic ring without an inner hyrodgen. The current strengths of the inner and outer routes are 13.8 nAT^{-1} and 13.0 nAT^{-1} respectively. A large fraction (17.7 nAT^{-1}) of the current takes the outer route in the case of the pyrrolic rings where there is an inner hydrogen. The ring-current strengths and pathways are shown in Figure 4.2a. At the cyclopentandienyl moiety, a larger portion (20.5 nAT^{-1}) of the net current takes the inner route with 24% (6.3 nAT^{-1}) of the total current passing the outer route of the ring.

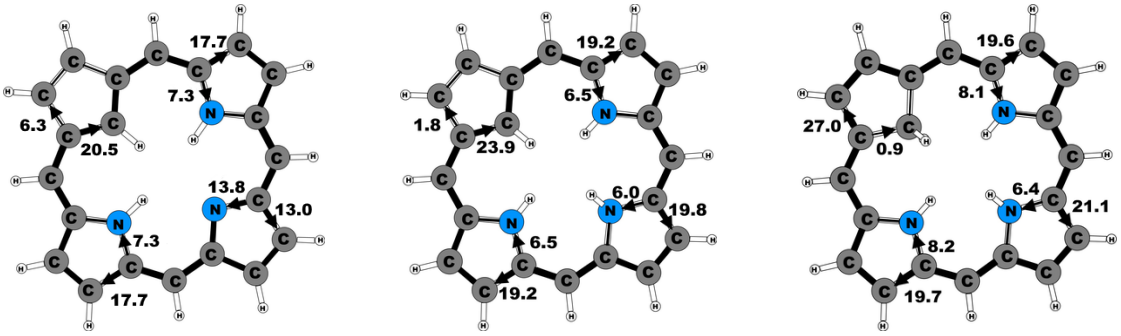

(a) **(b)** **(c)**

Figure 4.2: The calculated net current strength (in nAT^{-1}) passing selected bonds for carbaporphyrins **a) 20**, **b)** $\mathbf{20H^+}$ and **c)** $\mathbf{20H_2^{2+}}$.

This however, is different from previous suggestions[36] that the current follows the 18π aromaticity, and that the inner NH group and C_β atom of the pyrrolic ring without an inner hyrogen do not belong to the aromatic pathway. Similar current pathways as for **20** are observed for the singly protonated carbaporphyrin $\mathbf{20H^+}$ (Figure 4.2b) and the doubly protonated carbaporphyrin $\mathbf{20H_2^{2+}}$ (Figure 4.2c). The net current strength of 25.7 nAT^{-1} for the singly protonated carbaporphyrin $\mathbf{20H^+}$ is practically the same as for the unprotonated **20**. However, the current strength of 27.8 nAT^{-1} for the doubly protonated $\mathbf{20H_2^{2+}}$ is about 10% larger than for **20** and $\mathbf{20H^+}$

4.3.2 Carbachlorin 11, 11′ and 11H$^+$

The calculated ring-current strength of **11** is 24.6 nAT^{-1}. The ring current at the cyclopentandienyl has a large portion of the current strength passing the inner route. The small ring-current strength of 1.5 nAT^{-1} which takes the outer route of this ring is understandable as the outer path has sp^3 hybridization carbons and is not expected to sustain any strong current. The pathway for the pyrrolic rings follows that of **20** where the current strength is divided almost equally at the pyrrolic ring without an inner hydrogen. For the pyrrolic rings where there is an inner hydrogen, a large fraction of the current takes the outer route. The route of the ring currents and the ring-current strengths are shown in Figure 4.3a.

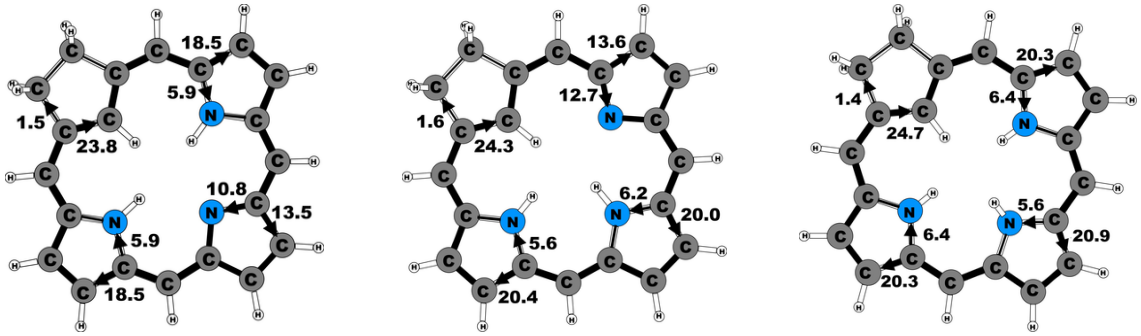

(a) **(b)** **(c)**

Figure 4.3: The calculated net current strength (in nAT^{-1}) passing selected bonds for carbachlorins **a) 11**, **b) 11**′ and **c) 11H**$^+$.

Compound **11**′ is a tautomer of **11** . Carbachlorin **11**′ has a net ring-current strength of 26.4 nAT^{-1} which is about 1.8 nAT^{-1} greater than that of **11**. The current pathways in **11**′, shown in Figure 4.3b, is similar to the one observed in **11**. However, there is significant difference at the pyrrolic ring without an inner hydrogen. The current strengths at the outer and inner routes are 13.6 nAT^{-1} and 12.7 nAT^{-1}, respectively. The protonated **11H**$^+$ (Figure 4.3c) has a net ring-current strength of 26.1 nAT^{-1}. Although a greater portion of the current takes the outer route in this carbachlorin, the inner current strength of 5.6 - 6.5 nAT^{-1} is significant and does not follow the superposition principle which Li and Lash used to predict the current pathways.[36] Thus, the inner NH at the pyrrolic ring

participate in the current transport around the carbachlorin macroring.

4.3.3 Carbachlorin 6a, 6b and 14

Carbachlorin **6a** (*trans*) sustains a net current strength of 25.7 nAT^{-1}. The current pathway at the pyrrolic ring with NH has 75% of the current taking the outer route and the remaining 25% taking the inner route. For the pyrrolic ring with an inner hydrogen bonded to nitrogen atom, 55% of the ring current passes the outer path and 45% goes through the inner pathway. Figure 4.4b shows that the current pathways of the all-carbon five-membered ring has 1.3 nAT^{-1} taking the outer path and 24.3 nAT^{-1} of the current strength going through the inner route.

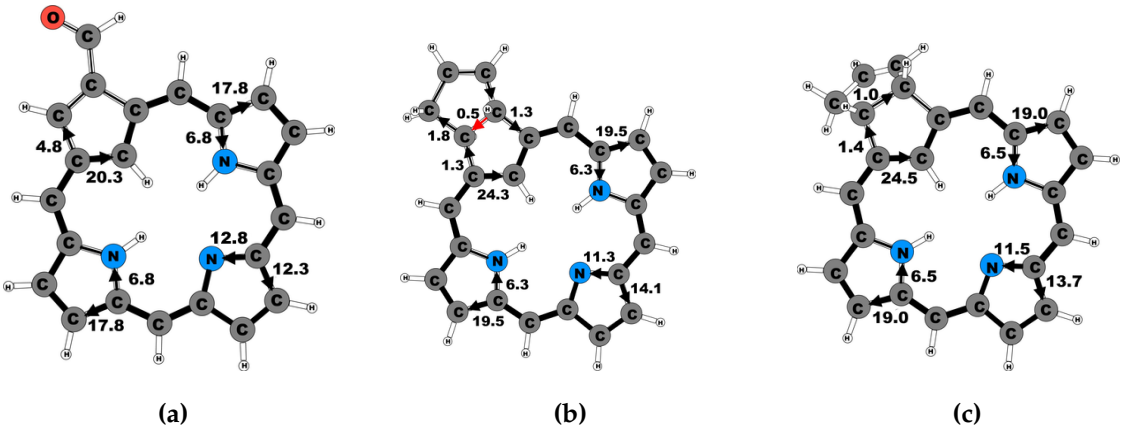

(a) **(b)** **(c)**

Figure 4.4: The calculated net current strength (in nAT^{-1}) passing selected bonds for compounds a) **14**, b) **6a** (*trans*) and c) **6b** (*cis*).

The ring-current pathways in **6b** (Figure 4.4c) with a net ring-current strength of 25.5 nAT^{-1} is not significantly different from what is observed in **6a** (Figure 4.4b). This shows that the substitution on the all-carbon five-membered ring does not significantly affects the ring current pathways or the ring-current strengths. Carbaporphyrin **14** (Figure 4.4a) has an aldehyde substituent on the cyclopentadienyl ring. The net ring-current strength is calculated to be 24.8 nAT^{-1} which is 2.0 nAT^{-1} smaller than that calculated for **20** (Figure 4.2a). This decrease in ring current may be ascribed to the electron withdrawing nature of the aldehyde substituent. The current at the cyclopentadienyl ring splits into an inner and outer route with a current strength of 20.3 nAT^{-1} and 4.8 nAT^{-1},

respectively.

4.3.4 Carbaporphyrinoids 9, 4, and 3

Tropiporphyrin **4** , which has the cyclopentadienyl moiety replaced with a cycloheptatrienyl ring, has a net ring-current strength of 22.1 nAT^{-1}, which is 82% of the ring current of carbaporphyrin **20** (Figure 4.2a). The decrease in the ring-current strength might be attributed to the antiaromatic cycloheptatrienyl moiety. The antiaromatic nature of this moiety is seen from the ring-current strength of -15.9 nAT^{-1} sustained by this subring. The current pathways has 43% of the ring current using the inner route where there is no hydrogen attached to the nitrogen of the pyrrolic ring whereas 19% of the ring current takes the inner route for the pyrrolic ring with an inner hydrogen bonded to nitrogen. The pathway of the ring current is shown in Figure 4.5b.

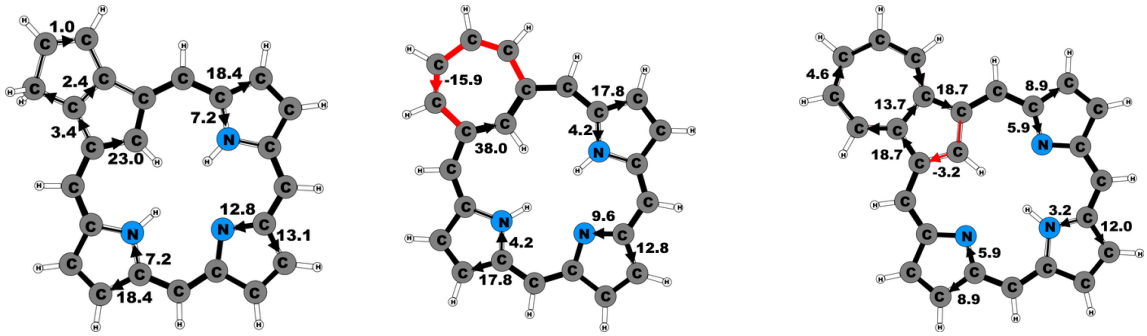

(a) **(b)** **(c)**

Figure 4.5: The calculated net current strength (in nAT^{-1}) passing selected bonds for compounds a) **9**, b) **4** and c) **3** .

Lash et al. proposed that the azuliporphyrin can be described by two resonance structures in which the zwitterionic form sustains a ring current around the carbaporphyrin macrocycle whereas the ring current in the other form revolves around the azulene moiety.[150,151] However, the picture obtained from GIMIC calculations differs somewhat from this scheme. The azuliporphyrin **3** (Figure 4.5c) macrocycle ring sustains a net ring-current strength of 15.1 nAT^{-1}. At the azulene moiety, the main current strength of 18.7 nAT^{-1} takes the outer route around the cycloheptatriene ring, with a weak current of 4.6 nAT^{-1} taking the outer route of the cycloheptatriene moiety.

4.3.5 Carbaporphyrinoids 1 and 2

Oxybenziporphyrin **1** sustains a net ring-current strength of 24.4 nAT^{-1}. The presence of the carbonyl group prevents the cyclohexadienone moiety from sustaining any significant ring current since the conjugation pathway is interrupted. The ring current which circles around the oxybenziporphyrin macrocyle uses the inner route of the cyclohexadienone where 97% of the ring current passes with only 3% using the outer path. The current pathways as well as the current strengths are shown in Figure 4.6a.

(a) **(b)**

Figure 4.6: The calculated net current strength (in nAT^{-1}) passing selected bonds for compounds a) **1** and b) **2** .

Benzocarbaporphyrin **2** sustains a net ring-current strength of 26.5 nAT^{-1}. The current pattern at the pyrrolic rings, as shown in Figure 4.6b, is similar to those observed for the other carbaporphyrins in this study. The benzoic moiety sustains a ring-current strength of 5.6 nAT^{-1}. At the cyclopentadienyl ring, the ring current prefers the inner route where 24.3 nAT^{-1} of the ring-current strength uses the inner route and only 1.3 nAT^{-1} of the ring-current strength using the outer route.

The total ring-current strengths and the current strengths (in nAT^{-1}) of the outer and inner pathways of the studied carbaporphyrinoids are summarized in Table 4.1. The numbering of the currents are shown in Figure 4.7. A pictorial representation of the signed modulus of the magnetically induced current vector for the studied molecules and the net current strengths (in nAT^{-1}) passing selected bonds for the studied molecules can be found in Appendix A.1.

Table 4.1: The total ring-current strength (in nAT^{-1}) and the current strengths (in nAT^{-1}) of the outer and inner pathways of the studied carbaporphyrinoids. The numbering of the currents are shown in Figure 4.7

Ring →		A		B		C		D	
Molecule	Total	1	2	3	4	5	6	7	8
20	26.8	6.3	20.5	17.7	7.3	13.0	13.8	17.7	7.3
20H$^+$	25.7	1.8	23.9	19.2	6.5	19.8	6.0	19.2	6.5
20H$_2^{2+}$	27.8	27.0	0.9	19.6	8.1	21.1	6.4	19.7	8.2
14	24.8	4.8	20.3	17.8	6.8	12.8	12.3	17.8	6.8
19	24.6	1.5	23.8	18.5	5.9	13.5	10.8	18.5	5.9
19′	26.1	1.6	24.3	13.6	12.7	20.0	6.2	20.4	5.6
19H$^+$	26.5	1.4	24.7	20.3	6.4	20.9	5.6	20.3	6.4
6b (cis)	25.5	1.4	24.5	19.0	6.5	13.7	11.5	19.0	6.5
6b (trans)	25.7	1.3	24.3	19.5	6.3	14.1	11.3	19.5	6.3
9	25.9	3.4	23.0	18.4	7.2	13.1	12.8	18.4	7.2
1	24.4	0.7	23.4	18.0	6.5	12.4	12.0	18.7	5.8
2	26.5	3.8	22.5	19.1	6.9	13.9	12.6	19.1	6.9
3	15.1	18.7	-3.2	8.9	5.9	12.0	3.2	8.9	5.9
4	22.1	-15.9	38.0	17.8	4.2	12.8	9.6	17.8	4.2

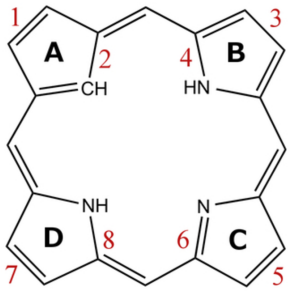

Figure 4.7: The numbering of the current pathways of the carbaporphyrinoids. Odd numbers indicates outer routes

4.4 Electronic Excitation Energies

The same optimized molecular structures as used in the current density analysis were also employed in the calculation of the electronic excitation energies. The calculations were performed for carbachlorins **11, 11H**$^+$, carbaporphyrin **20, 20H**$^+$ and **20H**$_2^{2+}$ whose experimental UV-Vis spectra have been reported enabling comparison between calculated and measured results.[36] The electronic excitation energies are reported in the wavelength unit of nanometers (nm) to enable easy comparison with that of the experimentally obtained results.

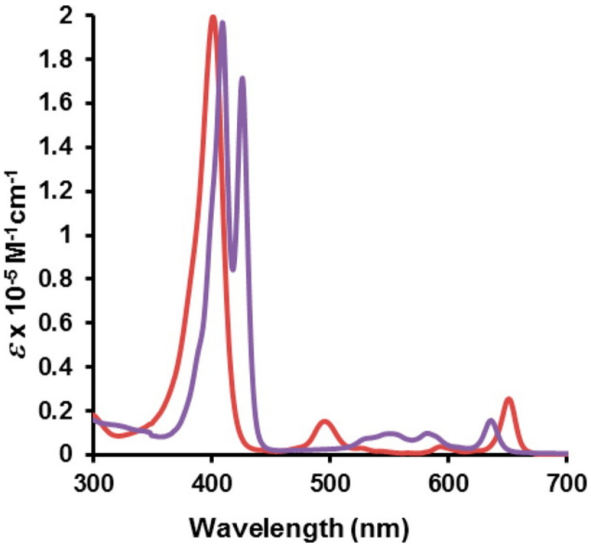

(a) The UV-Vis spectrum of **11** (red) and **11H**$^+$ (purple)

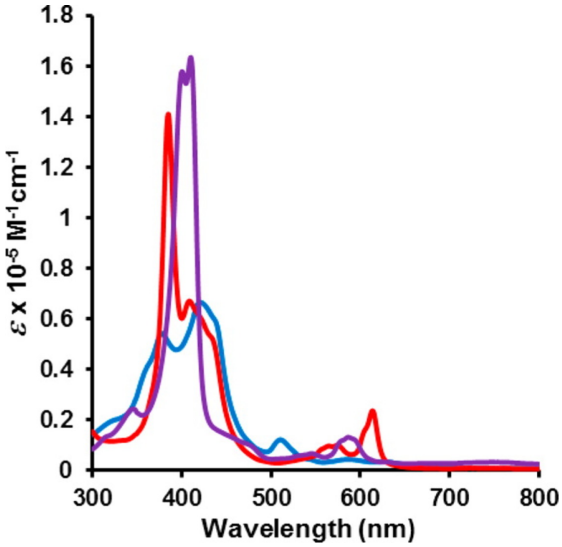

(b) The UV-Vis spectrum of **20** (blue), **20H**$^+$ (red) and **20H**$_2^{2+}$ (purple)

Figure 4.8: The experimental UV-Vis spectra of the studied compounds.[36]

The four lowest excited states were considered in the calculation of the vertical excitation energies because they should correspond to the Q and B (Soret) band in the porphyrin spectrum. The calculated oscillator strengths obtained are also representative for the intensities of the absorption. By using an in-house python code written by M. Johansson and modified by O. Lehtonen, a UV-Vis spectrum can then be obtained from the calculated vertical excitation energies.

4.4.1 Carbachlorin 11 and 11H$^+$

The first vertical excitation energy for carbachlorin **11** is overestimated at the TDDFT and RICC2 levels of theory. The calculated excitation energies at the TDDFT and RICC2 levels are 553 nm and 543 nm, respectively whereas the experimental value for the first excited state of **11** is 651 nm. Thus TDDFT overestimates the excitation by 98 nm (0.34 eV) while RICC2 level of theory also overestimates the excitation energy by 88 nm (0.38 eV). However, the RICC2 theory gives a quite accurate prediction for the second excited state. The experimental value for the second excited state is 495 nm. For this state, the TDDFT and RICC2 level of theory predicts the excitation energies to be 514 nm and 475 nm, respectively. At the TDDFT level of theory the excitation energies are underestimated by 19 nm (0.09 eV) whereas RICC2 overestimate the excitation energy by 20 nm (0.11 eV). Both the TDDFT and RICC2 calculations overestimate the excitation energies for the third

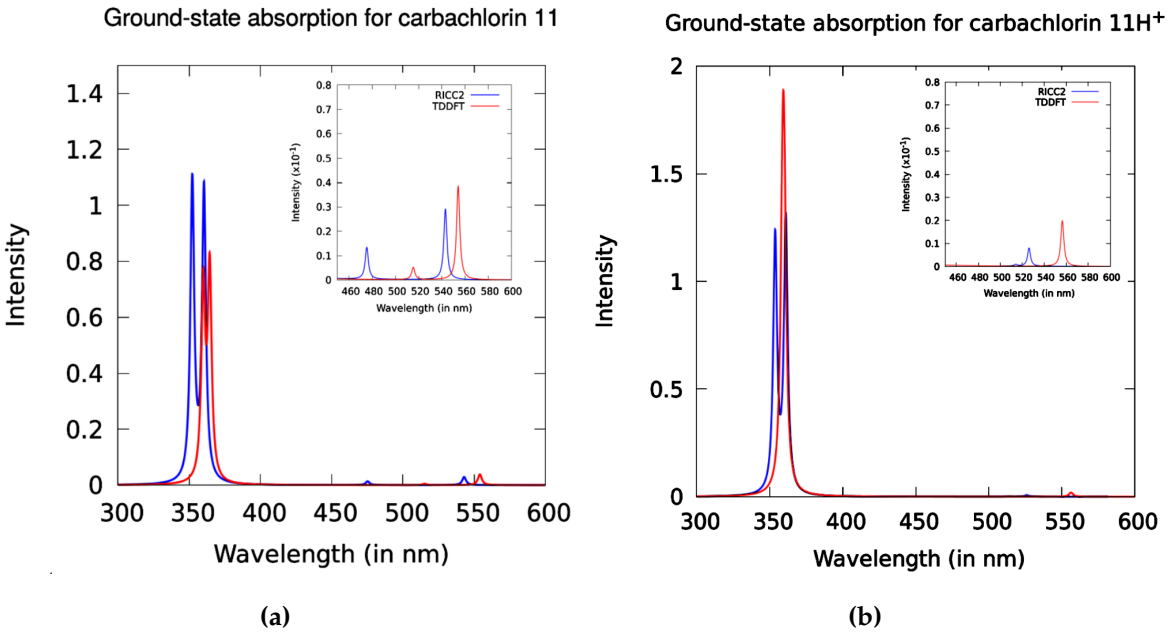

(a) **(b)**

Figure 4.9: The modelled UV-Vis spectrum for carbachlorin a) **11** and b) **11H**$^+$

state. The difference between the excitation energies obtained at the TDDFT and RICC2 levels is 4 nm. Whereas the oscillator strength at the TDDFT level predicts the third state to be the most intense, the RICC2 theory predicts the fourth state to be the most intense.

The first vertical excitation energy for carbachlorin **11H**$^+$ is overestimated at both

TDDFT and RICC2 levels of theory. The calculated excitation wavelengths at the TDDFT and RICC2 levels are 555 and 525 nm, respectively, compared to the experimental value[36] of 629 nm. The absorbance for the first state from the experimental spectrum in Figure 4.8a is significant, however, at the RICC2 level the calculated oscillator strength is almost approximately zero for this state.

The vertical excitation energies for all the four different states are overestimated at both RICC2 and TDDFT levels of theory. Since carbachlorin **11H**$^+$ is a charged compound, solvent effects, which are not included in this study, might play a significant role in the excitation energies in these compounds. The solvent effects on the vertical excitation energies for the carbaporphyrins will however, be studied in a future work.

4.4.2 Carbaporphyrin 20, 20H$^+$, and 20H$_2^{2+}$

The wavelengths of the first vertical excitation in carbaporphyrin **20**, predicted at TDDFT and RICC2 levels of theory are 596 nm and 579 nm, respectively. The wavelength of the first vertical excitation energy, at the TDDFT level of theory is 9 nm less than that of the experimental value of 590 nm, while that of the RICC2 is 11 nm more than the expermintal value. Similarly, the second and third vertical excitation energies are underestimated at the TDDFT level of theory while the RICC2 level of theory overestimates them. The second excitation energy predicted at the TDDFT level of theory has almost negligible intensity. The oscillator strengths for each of the four states studied are relatively low, with the fourth excitation for the RICC2 level at 379 nm being the most intense, with the oscillator strength of 0.37. This excitation energy value is 4 nm larger than that predicted by experiment . The TDDFT level of theory also predicts the fourth state to be the most intense with an oscillator strength of 0.13 and excitation energy of 407 nm which is 32 nm higher than the experimental value of 439 nm. The spectrum obtained from the computational studies for the singly protonated carbaporphyrin **20H**$^+$ is shown in Figure 4.10b. Whereas the TDDFT approach predicts more accurately the first and second vertical excitation energies (614 nm and 563 nm, respectively) , the RICC2 approach overestimates the first and second excitation energies by 43 nm and 40 nm, respectively. However, both the TDDFT and RICC2 levels of theory underestimate the excitation energies for the third

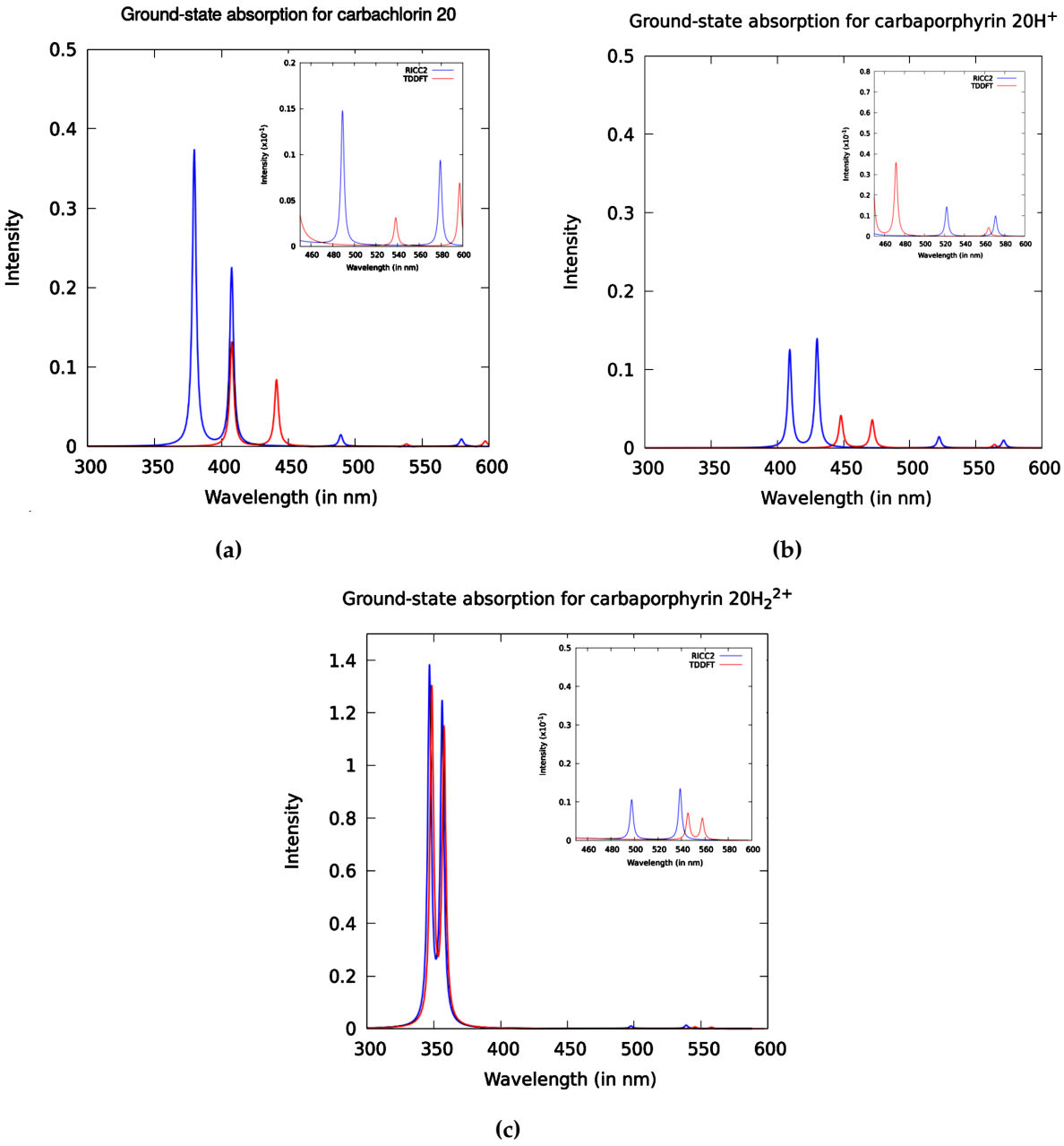

Figure 4.10: The modelled UV-Vis spectrum for carbaporphyrins a) **20**, b) $\mathbf{20H}^{+}$ and c) $\mathbf{20H_2}^{2+}$

and fourth states. The excitation energy of the third state is underestimated by 21 nm and 62 nm at the RICC2 and TDDFT levels, respectively. Similarly, the prediction at the RICC2 level of theory for the fourth state is 24 nm greater than the experimental value of 385 nm. The results for carbaporphyrin $\mathbf{20H}^{+}$ shows that while the RICC2 theory predicts relatively satisfactory excitation energies for the third and fourth states, it performs relatively poor for the first and second states which are more accurately predicted at the

TDDFT level of theory. Thus for this molecule, the RICC2 prediction for the Q band is satisfactory while the TDDFT level of theory gives a better estimate for the Soret (B) band.

The experimentally obtained spectrum for the doubly protonated carbaporphyrin **20H**$_2^{2+}$ (Figure 4.8b) shows an intense Soret (B) band which is slightly split at 413 - 399 nm. Similar spectrum is obtained from the computational studies at both the RICC2 and TDDFT levels of theory. The wavelengths of the third and fourth states are overestimated at both levels of theory. The RICC2 calculations, however, predicts a satisfactory excitation energy for the second state. Its prediction differs from the experimental value of 495 nm by 2 nm. Both levels of theory predict the same oscillator strength of 0.01 for the first and second states.

	11			11H$^+$		
States	TDDFT	RICC2	Experiment[a]	TDDFT	RICC2	Experiment[a]
1	553 (0.04)	543 (0.03)	651 (w)	555 (0.02)	525 (0.00)	629 (w)
2	514 (0.01)	475 (0.01)	495 (w)	539 (0.00)	514 (0.00)	539 (v)
3	364 (0.75)	360 (1.05)	398 (s)	360 (1.06)	361 (1.27)	426 (s)
4	359 (0.69)	352 (1.07)		358 (1.06)	353 (1.19)	409(s)
	20			20H$^+$		
States	TDDFT	RICC2	Experiment[a]	TDDFT	RICC2	Experiment[a]
1	596 (0.01)	579 (0.01)	590 (v)	613 (0.02)	571 (0.01)	614 (w)
2	539 (0.00)	488 (0.02)	516 (w)	563 (0.00)	523 (0.01)	563 (v)
3	441 (0.08)	407 (0.22)	427 (m)	471 (0.03)	430 (0.14)	409 (m)
4	407 (0.13)	379 (0.37)	375 (m)	447 (0.04)	409 (0.12)	385 (s)
	20H$_2^{2+}$					
States	TDDFT	RICC2	Experiment[a]			
1	558 (0.01)	539 (0.01)	582 (w)			
2	546 (0.01)	497 (0.01)	495 (w)			
3	357 (1.11)	356 (1.21)	413 (s)			
4	348 (1.27)	346 (1.35)	399 (s)			

Table 4.2: Vertical excitation energies (in nm) for the 11, 11H$^+$, 20, 20H$^+$, and 20H$_2^{2+}$ compounds calculated at the TDDFT and RICC2 levels of theory. Calculated oscillator strengths are given in parentheses. The relative absorbance of the experimentally obtained UV-Vis spectrum are labeled as letters in parentheses. (s) = strong (m) = medium (w) = weak (v) = very weak. [a] Experimental values were taken from Ref. 36

5. CONCLUSIONS

Magnetically induced current density has been calculated for some recently synthesized as well as spectroscopically and theoretically characterized carbaporphyrins and cabachlorins.[36] The geometry optimization as well as the nuclear magnetic shieldings of the studied molecules were performed at the density functional theory level (DFT) using the B3LYP functional.[141,142] The aromaticity of the compounds were computationally studied using the magnetic criterion. Though the aromaticity of the studied molecules has been predicted based on NICS and ^{1}H NMR spectroscopy calculations in a previous study[36], these two approaches have proven to be less reliable and the prediction of the aromatic properties of molecules based on this criteria can lead to inaccurate conclusions especially for multiring systems.[30,58,63,64,71] The gauge including magnetically induced current (GIMIC) approach which has proven to be a reliable tool has been used in this study. The GIMIC approach provides an accurate numerical integration of the current flow yielding reliable current strengths and pathways.[84,89]

All studied molecules were aromatic according to the ring current criterion. However, the ring current pathways differ from those predicted by Li and Lash based on spectroscopic and magnetic shielding calculations.[36] For all the studied compounds, the current transport around the pyrrolic rings involve all the π-electrons in the system. The current splits into an inner and outer path around the pyrrolic ring. However, for the pyrrolic rings which contain an inner hydrogen bonded to a nitrogen, a greater portion of the current uses the outer route, whereas for those pyrrolic rings in which the nitrogen atom is not bonded to hydrogen, the current splits almost evenly between the inner and outer route.

The degree of aromaticity for the studied compounds differs from one molecule to another. Tropiporphyrins **3** has the weakest aromaticity with a magnetically induced current strength of 15 nAT^{-1}. This is comparable to that of a benzene molecules whose aromaticity has been reported as 12.0 nAT^{-1}.[152] Carbaporphyrin $\mathbf{20H_2^{2+}}$ is the most aromatic compound among the studied molecules. Carbaporphyrin **20** and carbachlorin **11** which have protonated derivatives showed that protonation slightly increases the aromaticity of these carbaporphyrins. The effect of substituents on the cyclopentadienyl moiety was studied in carbaporphyrin **14** which had an aldehyde group, and it is observed that the current pathway is not significantly affected by the carbonyl substituent. The signed modulus and a streamline plot of the current density 1 bohr above the carporphyrinoids molecules is presented in Appendix A.1. A summary of the total ring-current strengths and the current strengths (in nAT^{-1}) of the outer and inner pathways of the studied carbaporphyrinoids can be found in Table 4.1

The vertical electronic excitation energies for carbachlorins **11, 11H**$^+$, carbaporphyrin **20, 20H**$^+$ and $\mathbf{20H_2^{2+}}$ have been computationally studied using the linear response TDDFT and the RICC2 levels of theory. By using an in-house code, the UV-Vis spectra of the carbachlorins and carbaporphyrins has been simulated from the calculated excitation energies and oscillator strengths obtained. The simulated UV-Vis spectra have been compared with those obtained from experiment. The four lowest excited state were selected for the calculation of the excitation energies as they should correspond to the Q and B bands found in porphyrin systems. Comparison with experiment shows that the predictions at the TDDFT level fluctuates between an overestimation and underestimation of the excitation energies for both the Q and Soret (B) bands. The predictions for the neutral compounds **20** and **11** at the TDDFT level shows maximum deviation of 32 nm and 98 nm respectively, which can be considered to be in good agreement with experiment. However, for the charged molecules, carbaporphyrin **20H**$^+$, $\mathbf{20H_2^{2+}}$ and carbachlorin **11H**$^+$, the results obtained at the TDDFT level of theory do not agree well with those of experiment except for the B band of **11H**$^+$. The predictions at the RICC2 level of theory generally overestimate the excitation energies for the studied molecules except for the Q bands of **20H**$^+$ in which the prediction deviates by 24 nm and shows good agreement with that

of experiment. The overestimation of excitation energies could be attributed to solvent effects, especially for the charged molecules. The solvent effects were not accounted for in this study, but they will be studied in a future work.

References

1 *Online Etymology Dictionary*, 2016, http://www.etymonline.com/index.php?term=porphyria.

2 A. Berlicka, P. Dutka, L. Szterenberg and L. Latos-Grażyński, *Angew. Chem. Int. Ed.*, 2014, **53**, 4885–4889.

3 S. Aronoff and M. Calvin, *J. Org. Chem.*, 1943, **8**, 205–223.

4 M. O. Senge, *Angew. Chem. Int. Ed.*, 2011, **50**, 4272–4277.

5 Berlin K., *Angew. Chem. Int. Ed.*, 1996, **35**, 1820–1822.

6 T. D. Lash and S. T. Chaney, *Chem. Eur. J.*, 1996, **2**, 944–948.

7 M. Pawlicki and L. Latos-Grażyński, *Chem. Rec.*, 2006, **6**, 64–78.

8 R. K. Pandey and G. Zheng, *Porphyrin Handbook*, Academic Press, San Diego, CA, 2000, vol. 6, pp. 157–230.

9 M. Jurow, A. E. Schuckman, J. D. Batteas and C. M. Drain, *Coord. Chem. Rev.*, 2010, **254**, 2297–2310.

10 M. G. Walter, A. B. Rudine and C. C. Wamser, *J. of Porphyrins and Phthalocyanines*, 2010, **14**, 759–792.

11 B. Kovačevič, D. Barič, Z. B. Maksić and T. Müller, *ChemPhysChem*, 2004, **5**, 1352–1364.

12 A. Stanger, *Chem. Comm.*, 2009, 1939–1947.

13 F. London, *J. Phys. Radium*, 1937, **8**, 397–409.

14 J. A. Pople, *J. Chem. Phys.*, 1956, **24**, 1111.

15 J. A. Pople, *Mol. Phys.*, 1958, **1**, 175.

16 R. McWeeny, *Mol. Phys.*, 1958, **1**, 311.

17 R. Kaiser, *Angew. Chem. Int. Ed.*, 1968, **7**, 345–350.

18 M. Faraday, *Phil. Trans. Roy.*, 1825, **115**, 440–466.

19 A. Kekulé, *Bull. Soc. Chim.*, 1865, **3**, 98.

20 A. Kekuié, *Justus Liebigs Annalen der Chemie*, 1866, **137**, 129–196.

21 R. Gershoni-Poranne and A. Stanger, *Chem. Soc. Rev.*, 2015, **44**, 6597–6615.

22 H. Günther, *NMR-Spektroskopie: eine Einführung in die Protonenresonanz-Spektroskopie und ihre Anwendungen in der Chemie*, G. Thieme, 1983.

23 V. I. Minkin, M. N. Glukhovtsev and B. Y. Simkin, *Aromaticity and Antiaromaticity*, Wiley New York, 1994.

24 J. A. Pople and K. G. Untch, *J. Am. Chem. Soc.*, 1966, **88**, 4811–4815.

25 H. J. Dauben Jr, J. D. Wilson and J. L. Laity, *Non-benzenoid Aromatics*, Academic Press, New York, 1971, vol. 2.

26 U. Fleischer, W. Kutzelnigg, P. Lazzeretti and V. Mühlenkamp, *J. Am. Chem. Soc.*, 1994, **116**, 5298.

27 P. von Ragué Schleyer and H. Jiao, *Pure Appl. Chem.*, 1996, **28**, 209.

28 L. Jackman, F. Sondheimer, Y. Amiel, D. Ben-Efraim, Y. Gaoni, R. Wolovsky and A. Bothner-By, *J. Am. Chem. Soc.*, 1962, **84**, 4307–4312.

29 C. D. Stevenson, and T. L. Kurth, *J. Am. Chem. Soc.*, 2000, **122**, 722–723.

30 C. S. Wannere, C. Corminboeuf, W. D. Allen, H. F. Schaefer III and P. von Ragué Schleyer, *Org. Letters*, 2005, **7**, 1457–1460.

31 H. Günther, *NMR Spectroscopy*, Wiley, New York, 1980.

32 H. Günther, *NMR Spectroscopy: Basic Principles, Concepts, and Applications in Chemistry*, John Wiley & Sons, 2nd edn, 1995.

33 W. Kutzelnigg, U. Fleischer and M. Schindler, *NMR basic principles and progress. Vol 23*, Springer, Berlin, 1990, pp. 165–262.

34 B. Blümich, *Essential NMR: for Scientists and Engineers*, Springer, 1st edn, 2005.

35 S. M. Bachrach, *Computational Organic Chemistry*, Wiley-Interscience, 2007.

36 D. Li and T. D. Lash, *J. Org. Chem.*, 2014, **79**, 7112–7121.

37 R. L. Carlin, *Magnetochemistry*, Springer, 1986.

38 A. Earnshaw, *Introduction to Magnetochemistry*, Academic Press,Inc, New York, 1968.

39 P. W. Selwood, *Magnetochemistry*, Interscience Publishers,New York, 2nd edn, 1956.

40 A. A. Bothner-By and J. A. Pople, *Annu. Rev. Phys. Chem.*, 1965, **16**, 43–66.

41 L. Pauling, *J. Chem. Phys.*, 1936, **4**, 637.

42 H. J. Dauben Jr, J. D. Wilson and J. L. Laity, *J. Am. Chem. Soc.*, 1968, **90**, 811.

43 P. Pascal, *J. Ann. Chm. Phys.*, 1910, **19**, 5.

44 P. Pascal, *J. Compt. Rend*, 1951, **233**, 10783.

45 M. Kumar, R. Gupta and R. R. G. (eds.), *Diamagnetic Susceptibility and Anisotropy of Inorganic and Organometallic Compounds*, Springer-Verlag Berlin Heidelberg, 1st edn, 2007.

46 W. Haberditzl, *Angew. Chem. Int. Ed.*, 1966, **5**, 288–298.

47 P. von Ragué Schleyer, C. Maerker, A. Dransfeld, H. Jiao and N. J. R. van Eikema Hommes, *J. Am. Chem. Soc.*, 1996, **118**, 6317–6318.

48 Z. Chen, C. S. Wannere, C. Corminboeuf, R. Puchta and P. von Ragué Schleyer, *Chem. Rev.*, 2005, **105**, 3842–3888.

49 P. von Ragué Schleyer, Haijun Jiao, Hommes, N. J. R. van Eikema, V. G. Malkin and O. L. Malkina, *J. Am. Chem. Soc.*, 1997, **119**, 12669–12670.

50 P. von Ragué Schleyer and M. Manoharan and Z-X. Wang and B. Kiran and H. Jiao and R. Puchta and N. J. R. van Eikema Hommes, *Org. Lett.*, 2001, **3**, 2465–2468.

51 E. Steiner and P. W. Fowler, *J. Phys. Chem. A*, 2001, **105**, 9553–9562.

52 I. Cernusak, P. Fowler and E. Steiner, *Mol. Phys.*, 2000, **98**, 945–953.

53 E. Steiner, P. W. Fowler and L. W. Jenneskens, *Angew. Chem. Int. Ed.*, 2001, **40**, 362–366.

54 C. Corminboeuf, T. Heine and J. Weber, *Phys. Chem. Chem. Phys.*, 2003, **5**, 246–251.

55 W. Kutzelnigg, C. van Wüllen, U. Fleischer, R. Franke and T. van Mourik, *Nuclear Magnetic Shieldings and Molecular Structure*, Kluwer Academic Publishers, 1993, pp. 141–161.

56 K. Wolinski, J. F. Hinton and P. Pulay, *J. Am. Chem. Soc.*, 1990, **112**, 8251–8260.

57 H. Fallah-Bagher-Shaidaei, C. S. Wannere, C. Corminboeuf, R. Puchta and P. von Ragué Schleyer, *Org. Lett.*, 2006, **8**, 863–866.

58 D. Du, H. Fliegl and D. Sundholm, *J. Chin. Chem. Soc.*, 2015, **63**, 93–100.

59 J. Jusélius and D. Sundholm, *Phys. Chem. Chem. Phys.*, 1999, **1**, 3429–3435.

60 I. Morao and F. P. Cossío, *J. Org. Chem.*, 1999, **64**, 1868.

61 M. Bühl, *Chem. Eur. J.*, 1998, **4**, 734–739.

62 A. Stanger, *J. Org. Chem.*, 2006, **71**, 883–893.

63 P. Lazzeretti, *Phys. Chem. Chem. Phys.*, 2004, **6**, 217–223.

64 S. Pelloni, G. Monaco, P. Lazzeretti and R. Zanasi, *Phys. Chem. Chem. Phys.*, 2011, **13**, 20666–20672.

65 P. Lazzeretti, *Prog. Nucl. Magn. Reson. Spectrosc.*, 2000, **36**, 1–88.

66 I. Morao, B. Lecea and F. P. Cossío, *J. Org. Chem.*, 1997, **62**, 7033–7036.

67 J. O. C. Jiménez-Halla, E. Matito, J. Robles and M. Solá, *J. Organomet. Chem.*, 2006, **691**, 4359–4366.

68 Y. C. Lin, D. Sundholm and J. Jusélius, *J. Chem. Theory Comput.*, 2006, **2**, 761–764.

69 S. Pelloni and P. Lazzeretti, *J. Phys. Chem. A*, 2013, **117**, 9083–9092.

70 Z. Badri, S. Pathak, H. Fliegl, P. Rashidi-Ranjbar, R. Bast, R. Marek, C. Foroutan-Nejad and K. Ruud, *J. Chem. Theory Comput.*, 2013, **9**, 4789–4796.

71 G. Monaco and R. Zanasi, *J. Phys. Chem. A*, 2014, **118**, 1673–1683.

72 J. C. A. Coulson, *Mol. Phys*, 1975, **30**, 713.

73 R. Hegstrom and W. Lipscomb, *J. Chem. Phys.*, 1968, **48**, 809–811.

74 P. Atkins and J. Gomes, *Mol. Phys.*, 1976, **32**, 1063–1074.

75 T. Helgaker, M. Jaszuński and K. Ruud, *Chem. Rev.*, 1999, **99**, 293–352.

76 M. K. M. B. V. G. Malkin, *Calculation of NMR and EPR parameters : theory and applications*, Wiley-VCH, 2004.

77 J. R. Cheeseman, G. W. Trucks, T. A. Keith and M. J. Frisch, *J. Chem. Phys.*, 1996, **104**, 5497.

78 R. F. W. Bader and T. A. Keith, *J. Chem. Phys.*, 1993, **99**, 3683–3693.

79 A. Soncini and P. W. Fowler, *Chem. Phys. Letters*, 2008, **450**, 431–436.

80 P. Lazzeretti, M. Malagoli and R. Zanasi, *Chem. Phys. Letters*, 1994, **220**, 299–304.

81 S. Coriani, P. Lazzeretti, M. Malagoli and R. Zanasi, *Theor. Chim. Acta*, 1994, **89**, 181–192.

82 S. T. Epstein, *J. Chem. Phys.*, 1973, **58**, 1592–1595.

83 J. Gauss and J. F. Stanton, *Adv. Chem. Phys.*, 2002, **123**, 355–422.

84 H. Fliegl, S. Taubert, O. Lehtonen and D. Sundholm, *Phys. Chem. Chem. Phys.*, 2011, **77**, 3408–3414.

85 G. Monaco, R. Zanasi, S. Pelloni and P. Lazzeretti, *J. Chem. Theory Comput.*, 2010, **6**, 3343–3351.

86 J. Jusélius, D. Sundholm and J. Gauss, *J. Chem. Phys.*, 2004, **121**, 3952–3963.

87 M. Kaipio, M. Patzschke, H. Fliegl, F. Pichierri and D. Sundholm, *J. Phys. Chem. A*, 2012, **116**, 10257–10268.

88 H. Fliegl and D. Sundholm, *J. Org. Chem.*, 2012, **77**, 3408–3414.

89 H. Fliegl, D. Sundholm and F. Pichierri, *Phys. Chem. Chem. Phys.*, 2011, **13**, 20659–20665.

90 H. Fliegl, O. Lehtonen, M. Patzschke, D. Sundholm and Y. C. Lin, *Theoret. Chem. Acc.*, 2011, **129**, 701–713.

91 H. Fliegl, O. Lehtonen, D. Sundholm and V. R. I. Kaila, *Phys. Chem. Chem. Phys.*, 2011, **13**, 434–437.

92 R. Ahlrichs, M. Bär, M. Häser, H. Horn and C. Kölmel, *Chem. Phys. Letters*, 1989, **162**, 165–169.

93 F. Furche, R. Ahlrichs, C. Hättig, W. Klopper, M. Sierka and F. Weigend, *WIREs Comput. Mol. Sci.*, 2014, **4**, 91–100.

94 J. F. Stanton, J. Gauss, M. E. Harding and P. G. Szalay, 2009, CFOUR, Coupled Cluster techniques for Computational Chemistry, a quantum-chemical program package also with contributions from A.A. Auer, R.J. Bartlett, U. Benedikt, C. Berger, D.E. Bernholdt, Y.J. Bomble, O. Christiansen, M. Heckert, O. Heun, C. Huber, T.-C. Jagau, D. Jonsson, J. Jusélius, K. Klein, W.J. Lauderdale, D.A. Matthews, T. Metzroth, D.P. O'Neill, D.R. Price, E. Prochnow, K. Ruud, F. Schiffmann, S. Stopkowicz, M.E. Varner, J. Vázquez, F. Wang, J.D. Watts and the integral packages MOLECULE (J. Almlöf and P.R. Taylor), PROPS (P.R. Taylor), ABACUS (T. Helgaker, H.J. Aa. Jensen,

P. Jørgensen, and J. Olsen), and ECP routines by A. V. Mitin and C. van Wüllen. For the current version, see http://www.cfour.de.

95 M. J. Frisch, G. W. Trucks, H. B. Schlegel, G. E. Scuseria, M. A. Robb, J. R. Cheeseman, G. Scalmani, V. Barone, B. Mennucci, G. A. Petersson, H. Nakatsuji, M. Caricato, X. Li, H. P. Hratchian, A. F. Izmaylov, J. Bloino, G. Zheng, J. L. Sonnenberg, M. Hada, M. Ehara, K. Toyota, R. Fukuda, J. Hasegawa, M. Ishida, T. Nakajima, Y. Honda, O. Kitao, H. Nakai, T. Vreven, J. J. A. Montgomery, J. E. Peralta, F. Ogliaro, M. Bearpark, J. J. Heyd, E. Brothers, K. N. Kudin, V. N. Staroverov, R. Kobayashi, J. Normand, K. Raghavachari, A. Rendell, J. C. Burant, S. S. Iyengar, J. Tomasi, M. Cossi, N. Rega, J. M. Millam, M. Klene, J. E. Knox, J. B. Cross, V. Bakken, C. Adamo, J. Jaramillo, R. Gomperts, R. E. Stratmann, O. Yazyev, A. J. Austin, R. Cammi, C. Pomelli, J. W. Ochterski, R. L. Martin, K. Morokuma, V. G. Zakrzewski, G. A. Voth, P. Salvador, J. J. Dannenberg, S. Dapprich, A. D. Daniels, Ö. Farkas, J. B. Foresman, J. V. Ortiz, J. Cioslowski and D. J. Fox, *Gaussian∼09 Revision E.01*, Gaussian Inc. Wallingford CT 2009.

96 Y. Shao, L. F. Molnar, Y. Jung, J. Kussmann, C. Ochsenfeld, S. T. Brown, A. T. B. Gilbert, L. V. Slipchenko, S. V. Levchenko, D. P. O'Neill, R. A. DiStasio, R. C. Lochan, T. Wang, G. J. O. Beran, N. A. Besley, J. M. Herbert, C. Y. Lin, T. Van Voorhis, S. H. Chien, A. Sodt, R. S. V. A. Rassolov, P. E. Maslen, P. P. Korambath, R. D. Adamson, B. Austin, J. Baker, E. F. C. Byrd, H. Dachsel, R. J. Doerksen, A. Dreuw, B. D. Dunietz, A. D. Dutoi, T. R. Furlani, S. R. Gwaltney, A. Heyden, S. Hirata, C. P. Hsu, G. Kedziora, R. Z. Khalliulin, P. Klunzinger, A. M. Lee, M. S. Lee, W. Liang, I. Lotan, N. Nair, B. Peters, E. I. Proynov, P. A. Pieniazek, Y. M. Rhee, J. R. E. Rosta, C. D. Sherrill, A. C. Simmonett, J. E. S. H. L. Woodcock, W. Zhang, A. T. Bell, A. K. Chakraborty, D. M. Chipman, F. J. Keil, A. Warshel, W. J. Hehre, H. F. Schaefer III, J. Kong, A. I. Krylov, P. M. W. Gill and M. Head-Gordon, *Phys. Chem. Chem. Phys.*, 2006, **8**, 3172–3191.

97 J. A, *Nature*, 1933, **131**, 839–840.

98 E. Anslyn and D. Dougherty, *Modern Physical Organic Chemistry*, Univ. Sci. Books, 2006.

99 N. V. Tkachenko, *Optical spectroscopy: Methods and instrumentations*, Elsevier Science, 1st edn, 2006.

100 M. Göppert-Mayer, *Annalen der Physik*, 1931, **401**, 273–294.

101 J. Franck and E. G. Dymond, *Trans. Faraday Soc.*, 1926, **21**, 536–542.

102 A. D. McNaught and A. D. McNaught, *Compendium of chemical terminology*, Blackwell Science Oxford, 1997, vol. 1669.

103 M. Kasha, *Disc. of the Faraday Soc.*, 1950, **9**, 14–19.

104 J. D. Coyle, *Introduction To Organic Photochemistry*, Wiley, 1991.

105 E. T., *Quantum chemistry and spectroscopy*, Pearson, 3rd edn, 2013.

106 M. Gouterman, G. H. Wagnière and L. C. Snyder, *J. of Mol. Spec.*, 1963, **11**, 108–127.

107 R. Giovannetti, *Macro To Nano Spectroscopy*, InTech, 2012, ch. 3.

108 M. Gouterman and G.-E. Khalil, *J. of Mol. Spec.*, 1974, **53**, 88–100.

109 D. R. Hartree, *Proc. Camb. Phil. Soc*, 1928, **24**, 89–110.

110 V. Fock, *Z. Phys*, 1930, **61**, 126–148.

111 J. C. Slater, *Phys. Rev.*, 1951, **81**, 385–390.

112 J. C. Slater, *Phys. Rev.*, 1929, **34**, 1293–1322.

113 P.-O. Löwdin, *Phys. Rev.*, 1955, **97**, 1509–1520.

114 P. Fulde, *Electron correlations in molecules and solids*, Springer-Verlag, 3rd edn, 2002.

115 J. H. McGuire, *Electron correlation dynamics in atomic collisions*, Cambridge University Press, 1997.

116 C. Møller and M. S. Plesset, *Phys. Rev.*, 1934, **46**, 618.

117 M. A. Marques and E. Gross, *Annu. Rev. Phys. Chem.*, 2004, **55**, 427–455.

118 E. Gross and W. Kohn, *Adv. Quantum Chem*, 1990, **21**, 287–323.

119 K. Andersson, P.-Å. Malmqvist and B. O. Roos, *J. Chem. Phys.*, 1992, **96**, 1218–1226.

120 P. Å. Malmqvist, A. Rendell and B. O. Roos, *J. Phys. Chem.*, 1990, **94**, 5477–5482.

121 R. J. Bartlett, *Annu. Rev. Phys. Chem.*, 1981, **32**, 359–401.

122 F. Coester and H. Kümmel, *Nuclear Phys.*, 1960, **17**, 477–485.

123 J. Čížek, *J. Chem. Phys.*, 1966, **45**, 4256–4266.

124 J. Paldus, J. Čížek and I. Shavitt, *Phys. Rev. A*, 1972, **5**, 50–67.

125 R. J. Bartlett and G. D. Purvis, *Int. J. Quant. Chem.*, 1978, **14**, 561–581.

126 H. Sekino and R. J. Bartlett, *Int. J. Quant. Chem.*, 1984, **26**, 255–265.

127 J. Geertsen, M. Rittby and R. J. Bartlett, *Chem. Phys. Letters*, 1989, **164**, 57–62.

128 J. F. Stanton and R. J. Bartlett, *J. Chem. Phys.*, 1993, **98**, 7029–7039.

129 P. Piecuch and K. Kowalski, *Int. J. Mol. Sci.*, 2002, **3**, 676–709.

130 M. Das, R. K. Chaudhuri, S. Chattopadhyay and U. S. Mahapatra, *J Phys B At Mol Opt Phys*, 2011, **44**, 065003.

131 O. Christiansen, H. Koch and P. Jørgensen, *Chem. Phys. Letters*, 1995, **243**, 409.

132 J. Olsen, P. Jørgensen, T. Helgaker, O. Christiansen *et al.*, *J. Chem. Phys.*, 2000, **112**, 9736–9748.

133 E. Runge and E. K. U. Gross, *Phys. Rev. Lett.*, 1984, **52**, 997–1000.

134 *Wikipeadia Article on Runge-Gross theorem*, 2016, https://en.wikipedia.org/wiki/Runge%E2%80%93Gross_theorem.

135 M. K. Nazeeruddin, F. De Angelis, S. Fantacci, A. Selloni, G. Viscardi, P. Liska, S. Ito, B. Takeru and M. Grätzel, *J. Am. Chem. Soc.*, 2005, **127**, 16835–16847.

136 S. van Gisbergen, A. Rosa, G. Ricciardi and E. Baerends, *J. Chem. Phys.*, 1999, **111**, 2499–2506.

137 D. Jacquemin, E. A. Perpete, G. E. Scuseria, I. Ciofini and C. Adamo, *J. Chem. Theory Comput.*, 2008, **4**, 123–135.

138 M. Dierksen and S. Grimme, *J. Chem. Phys.*, 2004, **120**, 3544–3554.

139 J. Neugebauer, E. J. Baerends and M. Nooijen, *J. Phys. Chem. A*, 2005, **109**, 1168–1179.

140 L. Goerigk and S. Grimme, *J. Phys. Chem. A*, 2008, **113**, 767–776.

141 C. Lee, W. Yang and R. G. Parr, *Phys. Rev. B*, 1988, **37**, 785–789.

142 A. D. Becke, *J. Chem. Phys.*, 1993, **98**, 5648–5652.

143 M. Häser, R. Ahlrichs, H. P. Baron, P. Weis and H. Horn, *Theoret. Chim. Acta*, 1992, **83**, 455–470.

144 M. Kollwitz, M. Häser and J. Gauss, *J. Chem. Phys.*, 1998, **108**, 8295–8301.

145 S. Taubert, H. Konschin and D. Sundholm, *Phys. Chem. Chem. Phys.*, 2005, **7**, 2561–2569.

146 I. Benkyi, H. Fliegl, R. R. Valiev and D. Sundholm, *Phys. Chem. Chem. Phys.*, 2016, **18**, 11932–11941.

147 F. Weigend, M. Häser, H. Patzelt and R. Ahlrichs, *Chem. Phys. Letters*, 1998, **294**, 143–152.

148 C. Hättig and F. Weigend, *J. Chem. Phys.*, 2000, **113**, 5154–5161.

149 R. R. Valiev, H. Fliegl and D. Sundholm, *Phys. Chem. Chem. Phys.*, 2014, **16**, 11010–11016.

150 T. D. Lash, M. J. Hayes, J. D. Spence, M. A. Muckey, G. M. Ferrence and L. F. Szczepura, *J. Org. Chem.*, 2002, **67**, 4860–4874.

151 T. D. Lash, S. T. Chaney and D. T. Richter, *J. Org. Chem.*, 1998, **63**, 9076–9088.

152 R. R. Valiev, H. Fliegl and D. Sundholm, *Phys. Chem. Chem. Phys.*, 2015, **17**, 14215–14222.

A. Appendices

A.1 Pictorial representation of the current densities

Figure A.1: A pictorial representation of the signed modulus of the magnetically induced current vector for the studied molecules and a streamline plot of the current density 1 bohr above the carporphyrinoids molecules.

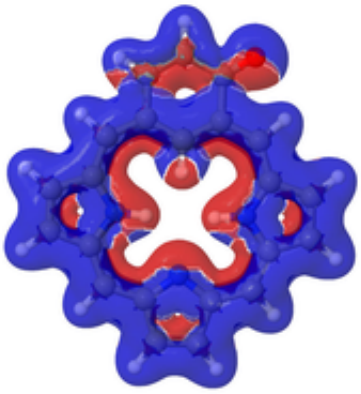

(A.1.1) The signed modulus of the magnetically induced current vector for oxybenziporphyrin **1**. The paratropic component of the ring current is shown in red and the diatropic component in blue.

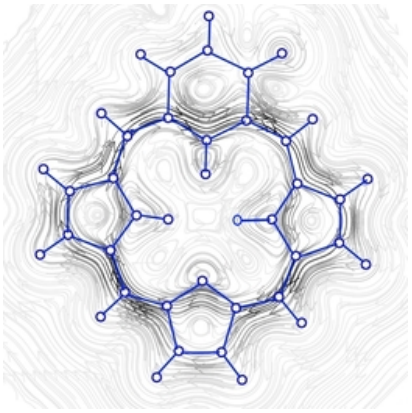

(A.1.2) A streamline plot of the current density 1 bohr above the oxybenziporphyrin **1** molecule that sustains a net ring-current strength of 24.4 nAT^{-1} around the porphyrinoid macroring.

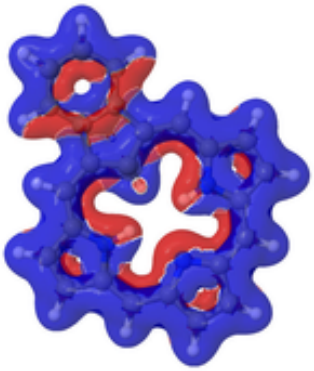

(A.1.3) The signed modulus of the magnetically induced current vector for benzocarbaporphyrin **2**. The paratropic component of the ring current is shown in red and the diatropic component in blue.

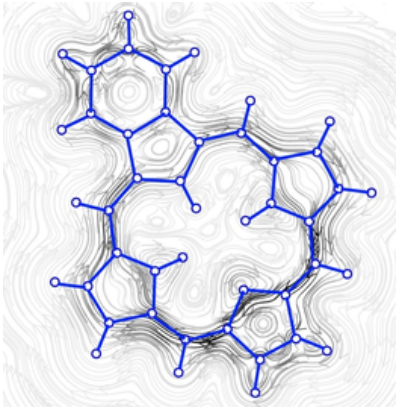

(A.1.4) A streamline plot of the current density 1 bohr above the benzocarbaporphyrin **2** molecule that sustains a net ring-current strength of 26.5 nAT^{-1} around the porphyrinoid macroring.

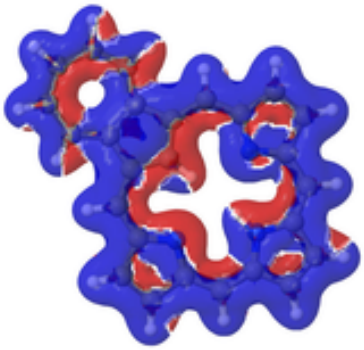

(A.1.5) The signed modulus of the magnetically induced current vector for azuliporphyrin **3**. The paratropic component of the ring current is shown in red and the diatropic component in blue.

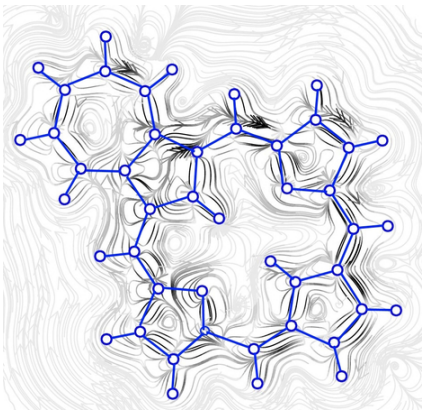

(A.1.6) A streamline plot of the current density 1 bohr above the azuliporphyrin **3** molecule that sustains a net ring-current strength of 15.1 nAT^{-1} around the porphyrinoid macroring.

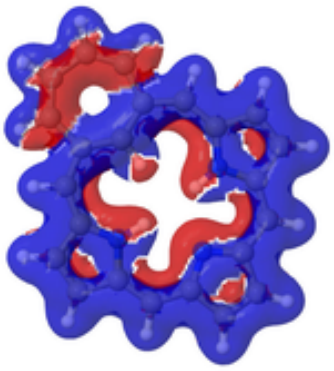

(A.1.7) The signed modulus of the magnetically induced current vector for tropiporphyrin **4**. The paratropic component of the ring current is shown in red and the diatropic component in blue.

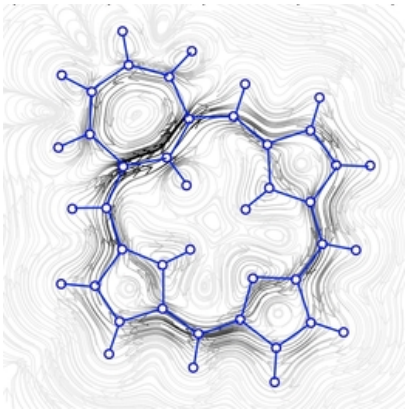

(A.1.8) A streamline plot of the current density 1 bohr above the tropiporphyrin **4** molecule that sustains a net ring-current strength of 21.9 nAT^{-1} around the porphyrinoid macroring.

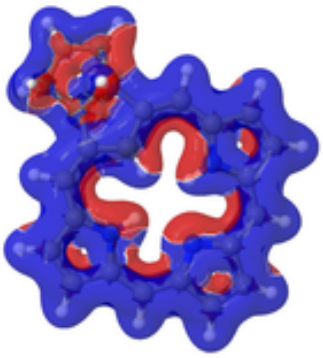

(A.1.9) The signed modulus of the magnetically induced current vector for carbachlorin **6a**. The paratropic component of the ring current is shown in red and the diatropic component in blue.

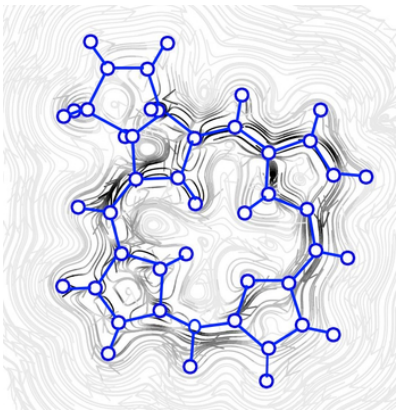

(A.1.10) A streamline plot of the current density 1 bohr above the carbachlorin **6b** (*trans*) molecule that sustains a net ring-current strength of 25.7 nAT^{-1} around the porphyrinoid macroring.

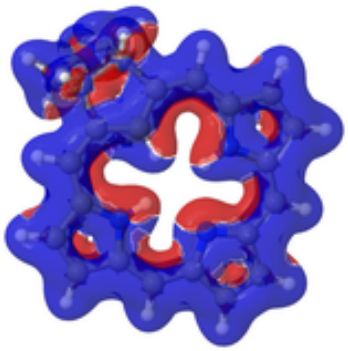

(A.1.11) The signed modulus of the magnetically induced current vector for carbachlorin **6b**. The paratropic component of the ring current is shown in red and the diatropic component in blue.

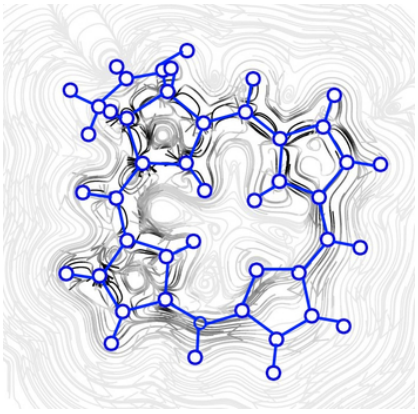

(A.1.12) A streamline plot of the current density 1 bohr above the carbachlorin **6b** (*cis*) molecule that sustains a net ring-current strength of 25.5 nAT^{-1} around the porphyrinoid macroring.

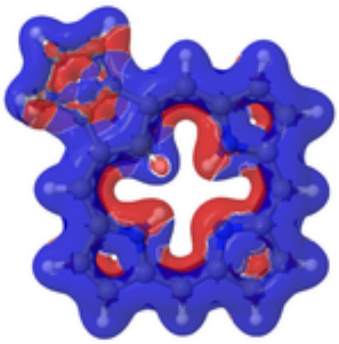

(A.1.13) The signed modulus of the magnetically induced current vector for carbaporphyrin **9**. The paratropic component of the ring current is shown in red and the diatropic component in blue.

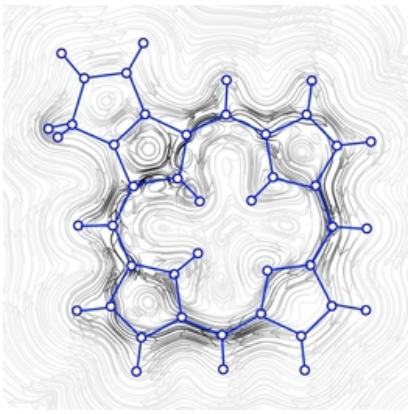

(A.1.14) A streamline plot of the current density 1 bohr above the carbaporphyrin **9** molecule that sustains a net ring-current strength of 25.9 nAT^{-1} around the porphyrinoid macroring.

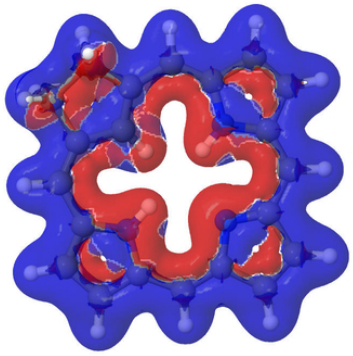

(A.1.15) The signed modulus of the magnetically induced current vector for carbachlorin **11**. The paratropic component of the ring current is shown in red and the diatropic component in blue.

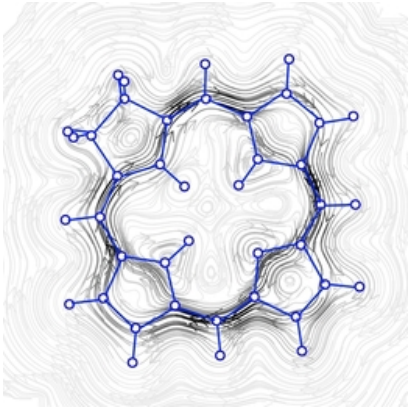

(A.1.16) A streamline plot of the current density 1 bohr above the carbachlorin **11** molecule that sustains a net ring-current strength of 24.6 nAT^{-1} around the porphyrinoid macroring

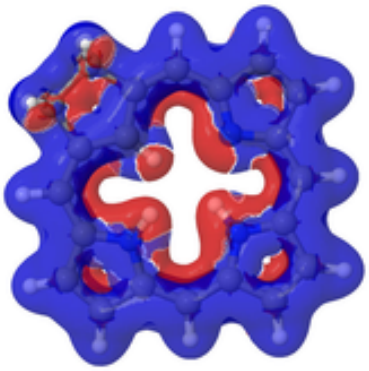

(A.1.17) The signed modulus of the magnetically induced current vector for carbachlorin **11′**. The paratropic component of the ring current is shown in red and the diatropic component in blue.

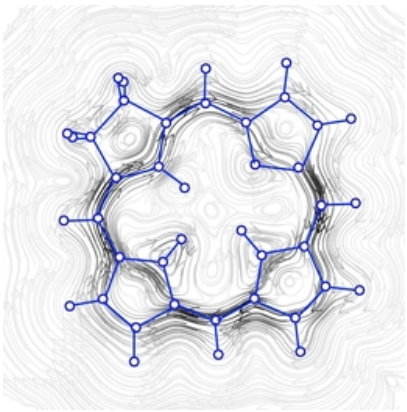

(A.1.18) A streamline plot of the current density 1 bohr above the carbachlorin **11′** molecule that sustains a net ring-current strength of 26.1 nAT^{-1} around the porphyrinoid macroring.

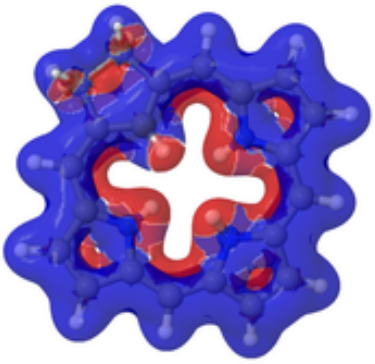

(A.1.19) The signed modulus of the magnetically induced current vector for carbachlorin **11H**$^+$. The paratropic component of the ring current is shown in red and the diatropic component in blue.

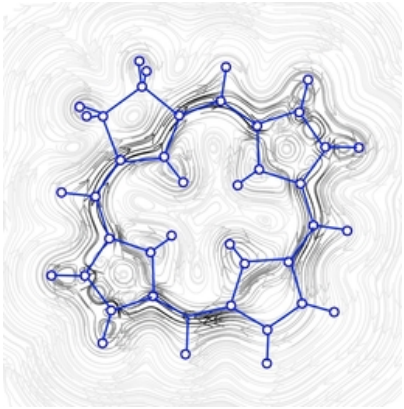

(A.1.20) A streamline plot of the current density 1 bohr above the carbachlorin **11H**$^+$ molecule that sustains a net ring-current strength of 26.5 nAT^{-1} around the porphyrinoid macroring.

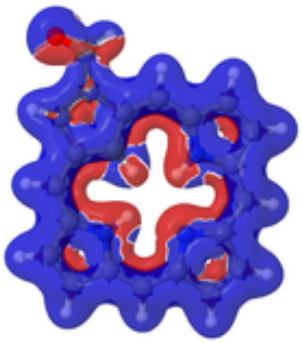

(A.1.21) The signed modulus of the magnetically induced current vector for carbaporphyrin **14**. The paratropic component of the ring current is shown in red and the diatropic component in blue.

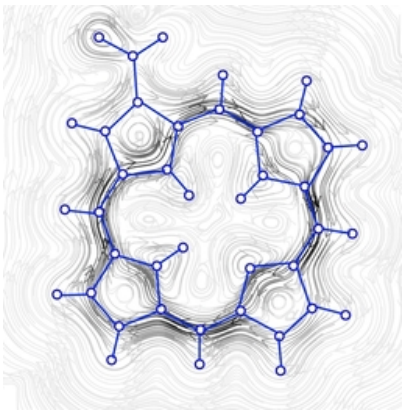

(A.1.22) A streamline plot of the current density 1 bohr above the carbaporphyrin **14** molecule that sustains a net ring-current strength of 24.6 nAT^{-1} around the porphyrinoid macroring.

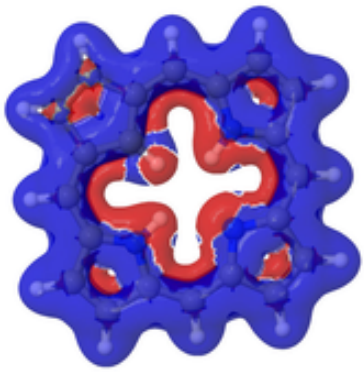

(A.1.23) The signed modulus of the magnetically induced current vector for carbaporphyrin **20**. The paratropic component of the ring current is shown in red and the diatropic component in blue.

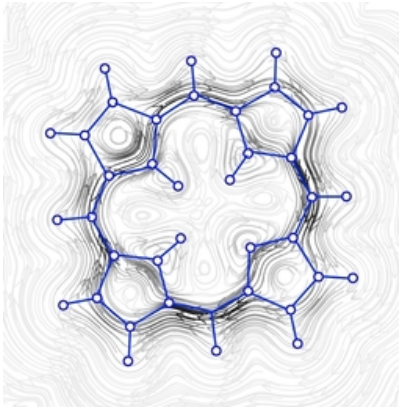

(A.1.24) A streamline plot of the current density 1 bohr above the carbaporphyrin **20** molecule that sustains a net ring-current strength of 26.8 nAT^{-1} around the porphyrinoid macroring.

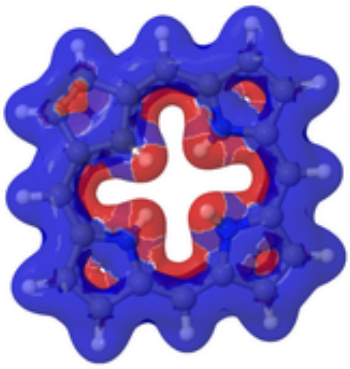

(A.1.25) The signed modulus of the magnetically induced current vector for carbaporphyrin $\mathbf{20H}^{+}$. The paratropic component of the ring current is shown in red and the diatropic component in blue.

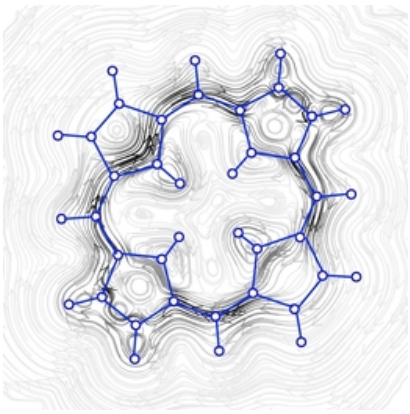

(A.1.26) A streamline plot of the current density 1 bohr above the carbaporphyrin $\mathbf{20H}^{+}$ molecule that sustains a net ring-current strength of 25.7 nAT^{-1} around the porphyrinoid macroring.

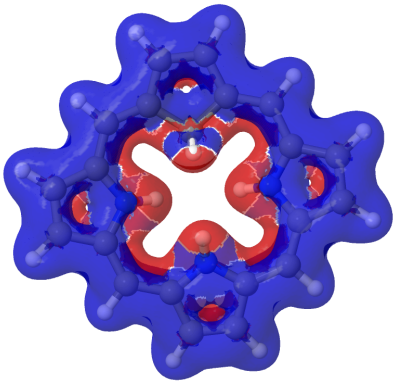

(A.1.27) The signed modulus of the magnetically induced current vector for carbaporphyrin $\mathbf{20H_2^{2+}}$. The paratropic component of the ring current is shown in red and the diatropic component in blue.

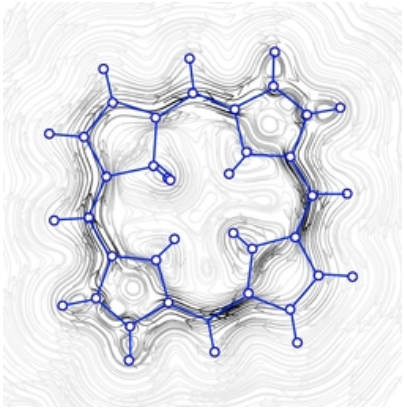

(A.1.28) A streamline plot of the current density 1 bohr above the carbaporphyrin $\mathbf{20H_2^{2+}}$ molecule that sustains a net ring-current strength of 27.8 $\mathrm{nAT^{-1}}$ around the porphyrinoid macroring.

A.2 Publication from the thesis

Printed with permission from the Royal Society of Chemistry.

PCCP

PAPER

View Article Online
View Journal

Cite this: DOI: 10.1039/c5cp06987d

New insights into aromatic pathways of carbachlorins and carbaporphyrins based on calculations of magnetically induced current densities†

Isaac Benkyi,*[a] Heike Fliegl,*[b] Rashid R. Valiev*[cd] and Dage Sundholm*[a]

Magnetically induced current densities have been calculated and analyzed for a number of synthesized carbachlorins and carbaporphyrins using density functional theory and the gauge including magnetically induced current (GIMIC) method. Aromatic properties have been determined by using accurate numerical integration of the current flow yielding reliable current strengths and pathways that are related to the degree of aromaticity and the aromatic character of the studied molecules. All investigated compounds are found to be aromatic. However, the obtained aromatic pathways differ from those previously deduced from spectroscopic data and magnetic shielding calculations. For all studied compounds, the ring current divides into an outer and an inner branch at each pyrrolic subring, showing that all π-electrons of the pyrrolic rings take part in the delocalization pathway. The calculations do not support the common notion that the main share of the current takes the inner route at the pyrrolic rings without an inner hydrogen and follows an 18π aromatic pathway. The aromatic pathways of the investigated carbaporphyrins and carbachlorins are very similar, since the current strength *via* the $C_\beta{=}C_{\beta'}$ bond of the cyclopentadienyl ring of the carbaporphyrins is almost as weak as the current density passing the corresponding saturated $C_\beta{-}C_{\beta'}$ bond of the carbachlorins.

Received 14th November 2015,
Accepted 25th February 2016

DOI: 10.1039/c5cp06987d

www.rsc.org/pccp

1 Introduction

Carbaporphyrinoids are porphyrin analogues in which one of the nitrogen atoms of the porphyrin macroring is replaced by an isoelectronic CH moiety.[1–6] Carbachlorins are similar molecules with a saturated $C_\beta{-}C_{\beta'}$ bond of the cyclopentadienyl ring. This class of organic compounds is interesting for chemists due to their potential use in catalysis as they are able to bind metals in unusual oxidation states.[1,6] In particular carbaporphyrinoid compounds such as carbachlorins with strong absorption bands at around 650 nm or even at longer wavelengths have the potential to be used as photosensitizers in photodynamic therapy.[7]

A clear picture of the full utilization of these compounds cannot be obtained without elucidating their aromatic properties. In spite of their unusual structure and chemistry, carbaporphyrinoids can be expected to be aromatic like most planar organic (heterocylic) compounds that exhibit conjugation pathways fulfilling the Hückel 4n + 2π rule for aromaticity. However, very little is known about their aromatic character and electron delocalization pathways,[8,9] mainly because it is challenging to experimentally quantify the electron delocalization of complicated multiring molecules, and computational studies of the aromatic character of porphyrinoids are also demanding. By using the gauge-including magnetically induced current (GIMIC) method,[10–12] it is though possible to determine current strength susceptibilities and current pathways by explicitly calculating the susceptibility of the magnetically induced current density passing selected chemical bonds. A careful analysis of the current density provides information about how electronic charge can be transported around molecular rings of fused multiring molecules.[10,12–19] Comprehensive and detailed current-density studies have proven to be very helpful in elucidating the aromatic properties of porphyrinoids.[20–28] Current density calculations carried out using the GIMIC program are an invaluable computational means for designing carbaporphyrinoids or other compounds with distinct aromaticity and electron delocalization features, since they can accurately predict aromatic pathways and ring-current strengths along different routes in the molecule.[10–12,29] The GIMIC program, which is a stand-alone

[a] University of Helsinki, Department of Chemistry, P. O. Box 55 (A.I. Virtanens plats 1), FIN-00014 University of Helsinki, Finland. E-mail: Dage.Sundholm@helsinki.fi
[b] Centre for Theoretical and Computational Chemistry (CTCC), Department of Chemistry, University of Oslo, P. O. Box 1033 Blindern, 0315 Oslo, Norway. E-mail: Heike.Fliegl@kjemi.uio.no
[c] Tomsk Polytechnic University, 43a Lenin Avenue, Building 2, Tomsk 634050, Russian Federation
[d] Tomsk State University, Lenina Avenue 36, Tomsk, Russian Federation. E-mail: valievrashid@mail.ru

† Electronic supplementary information (ESI) available. See DOI: 10.1039/c5cp06987d

code, has been employed in a number of aromaticity studies of porphyrinoids.[10,22–28] The studies have shown that numerical integration of the current strength susceptibilities passing selected chemical bonds is a reliable tool for quantifying molecular aromaticity according to the magnetic criterion.[30–32] By calculating the current strength susceptibilities of selected chemical bonds one obtains information about the electron-delocalization pathways. The approach has proven to be very useful for determining current pathways in multiring molecules, where many other approaches are prone to fail.[22,33–47]

In this work, we have employed the GIMIC method at the density functional theory (DFT) level to investigate the aromatic character of a number of traditional carbaporphyrinoids and modified carbaporphyrinoids such as oxybenziporphyrin,[48–50] benzocarbaporphyrin,[51,52] azuliporphyrin[51,53,54] and tropiporphyrin.[55,56] In addition, we have also studied a number of carbachlorins that have been synthesized and characterized.[9] The proton nuclear magnetic resonance (^{1}H NMR) and ultraviolet-visible (UV-Vis) spectra have been recorded to assess the aromatic properties of the synthesized carbachlorins and carbaporphyrins.[9] The calculated values for nucleus independent chemical shifts (NICS)[57] have been previously used for assessing the aromatic character and delocalization pathways of carbaporphyrinoids,[9] concluding that all the investigated carbaporphyrinoids are aromatic with a similar 18π aromatic pathway as the classical aromatic pathway of free-base porphyrin.[9] Nowadays it is well known that the NICS approach has difficulties in accurately determining the degree of aromaticity of single molecular rings.[33–43] Furthermore, NICS has even larger problems to provide reliable current pathways in multiring molecules such as free-base porphyrin.[22,58–62] Here we aim at providing novel insights regarding the aromatic pathways and electron delocalization pathways of the investigated compounds using the reliable current-density integration technique for analyzing the current flow.

The computational methods are described in Section 2. The molecular structures of the carbaporphyrinoids are discussed in Section 3, whereas the results of the current density calculations are presented in detail for all studied molecules in Section 4. The results of the study are summarized in Section 5 where the main conclusions are also drawn.

2 Computational methods

The optimization of the molecular structures as well as the calculations of the NMR shieldings were performed at the density functional theory (DFT) level using the Becke-three-parameter functional combined with the Lee–Yang–Parr exchange–correlation functional (B3LYP)[63,64] as implemented in Turbomole 6.6.[65,66] The Karlsruhe triple-ζ quality basis set (def2-TZVP) was used for all atoms.[67,68] The NMR shielding calculations were performed using the mpshift module of Turbomole.[69,70] Benchmark calculations have shown that B3LYP/def2-TZVP calculations of ^{1}H NMR and ^{13}C NMR chemical shifts are close to the basis-set limit and agree qualitatively with experimental data for organic molecules.[71]

The magnetically induced current densities were calculated at the B3LYP/def2-TZVP level using the GIMIC program.[10–12] GIMIC is an independent program that uses the atomic orbital density matrix as well as the corresponding first-order magnetically perturbed density matrices from the NMR shielding calculations and basis-set information as input data.[10,11] GIMIC employs gauge-including atomic orbitals (GIAOs), which imply that the basis set convergence is faster than with magnetic-field independent basis functions.[10,72,73] When GIAOs are employed, the obtained gauge-origin independent current densities were close to the complete basis-set limit already when standard basis sets are used.[72,73] The current densities can be analyzed by determining the current pathways, which are obtained by the numerical integration of the current-strength susceptibilities (in nA T^{-1}) flowing along the chosen chemical bonds. The current pathways are visualized using the XMakemol[74] and paint.net[75] programs. The pictures of the molecules have been drawn using the Marvin program.[76] The streamline representations of the current density have been obtained using PyNgl[77] and the schematic ring labeling displayed in Fig. 15 has been done using ChemBioDraw[78] and Gimp.[79]

The effects of dispersion corrections[80] on the geometry and the current strength were investigated for oxybenziporphyrin. No significant changes in the molecular structure or the ring-current strength were observed. See ESI.†

3 Molecular structures and nomenclature

A number of recently synthesized carbaporphyrins and carbachlorins[9] have been investigated computationally. The alkyl substituents have been omitted to save computational costs, since previous current density studies have shown that alkyl substituents do not significantly influence the current pathways and current strengths of aromatic porphyrinoids,[25] whereas for antiaromatic porphyrinoids substituents such as ethylformate or pentafluorophenyl may significantly reduce the strength of the ring current.[24–26] The labeling of the investigated molecules follows the one in ref. 9, which inspired us to perform the present study. The common notation enables easier comparison of the present results with previously published ones.[9,50]

Carbaporphyrin **20** (Fig. 1) is the most simple carbaporphyrin without any substituents. The carbaporphyrin cation **20H$^+$** (Fig. 2) is the protonated form of **20** with one extra inner hydrogen and a positive charge. The doubly protonated carbaporphyrin dication **20H$_2^{2+}$** (Fig. 3) has five inner hydrogens of which two saturate the inner carbon of the cyclopentadienyl ring. Carbaporphyrin **14** (Fig. 4) has an aldehyde group substituted in one of the C_β positions of the cyclopentadienyl ring of the carbaporphyrin.

Carbachlorin **19** is the most simple carbachlorin with a saturated C_β–$C_{\beta'}$ bond of the cyclopentadienyl ring and without any substituents. Carbachlorin **19** (Fig. 5) lacks the inner hydrogen in the *trans* position to the cyclopentadienyl ring, whereas carbachlorin **19′** (Fig. 6) is the corresponding *cis*

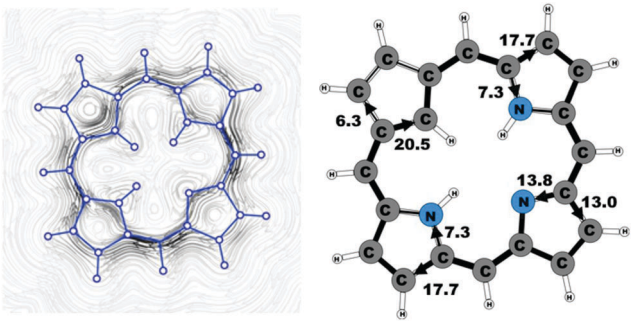

(a) (b)

Fig. 1 (a) A streamline plot of the current density 1 bohr above the carbaporphyrin **20** molecule that sustains a net ring-current strength of 26.8 nA T^{-1} around the porphyrinoid macroring. (b) The calculated net current strengths (in nA T^{-1}) passing selected bonds are given for carbaporphyrin **20**.

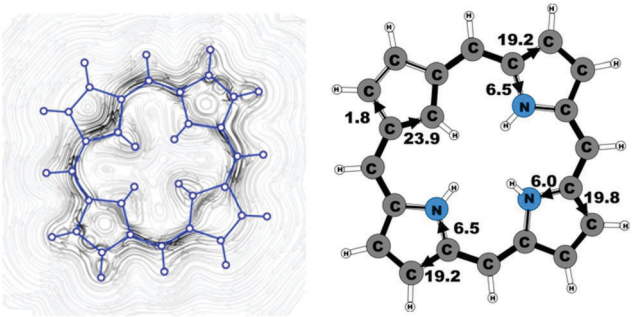

(a) (b)

Fig. 2 (a) A streamline plot of the current density 1 bohr above the carbaporphyrin **20H**$^+$ molecule that sustains a net ring-current strength of 25.7 nA T^{-1} around the porphyrinoid macroring. (b) The calculated net current strengths (in nA T^{-1}) passing selected bonds are given for carbaporphyrin **20H**$^+$.

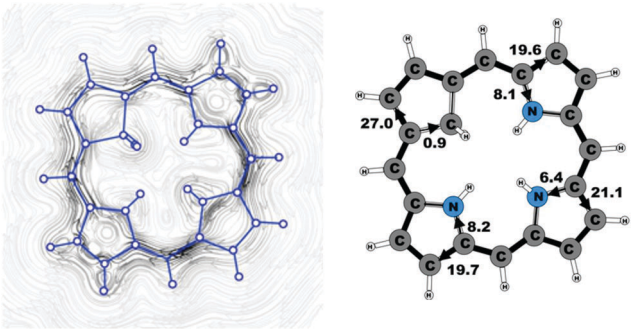

(a) (b)

Fig. 3 (a) A streamline plot of the current density 1 bohr above the carbaporphyrin **20H$_2$**$^{2+}$ molecule that sustains a net ring-current strength of 27.8 nA T^{-1} around the porphyrinoid macroring. (b) The calculated net current strengths (in nA T^{-1}) passing selected bonds are given for carbaporphyrin **20H$_2$**$^{2+}$.

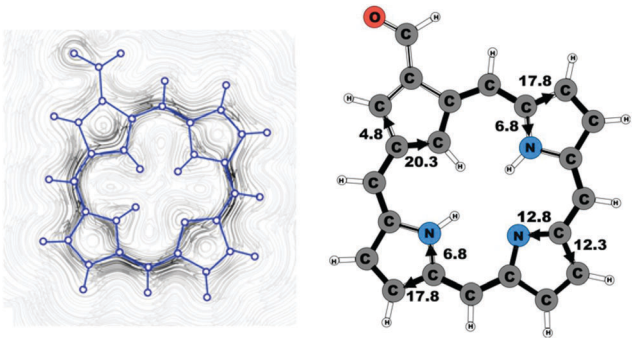

(a) (b)

Fig. 4 (a) A streamline plot of the current density 1 bohr above the carbaporphyrin **14** molecule that sustains a net ring-current strength of 24.6 nA T^{-1} around the porphyrinoid macroring. (b) The calculated net current strengths (in nA T^{-1}) passing selected bonds are given for carbaporphyrin **14**.

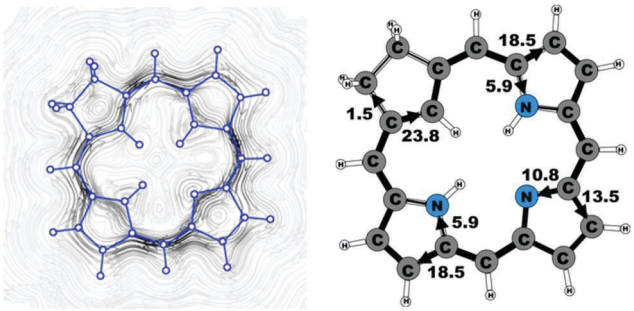

(a) (b)

Fig. 5 (a) A streamline plot of the current density 1 bohr above the carbachlorin **19** molecule that sustains a net ring-current strength of 24.6 nA T^{-1} around the porphyrinoid macroring. (b) The calculated net current strengths (in nA T^{-1}) passing selected bonds are given for carbachlorin **19**.

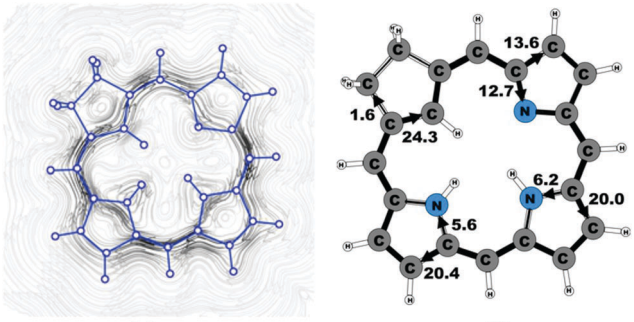

(a) (b)

Fig. 6 (a) A streamline plot of the current density 1 bohr above the carbachlorin **19′** molecule that sustains a net ring-current strength of 26.1 nA T^{-1} around the porphyrinoid macroring. (b) The calculated net current strengths (in nA T^{-1}) passing selected bonds are given for carbachlorin **19′**.

tautomer. The carbachlorin cation **19H**$^+$ (Fig. 7) is the protonated form of **19** and **19′** with four inner hydrogens.

In compound **6b**, a propene moiety is fused to the cyclopentadienyl ring forming a fused nonaromatic cyclopentene ring.

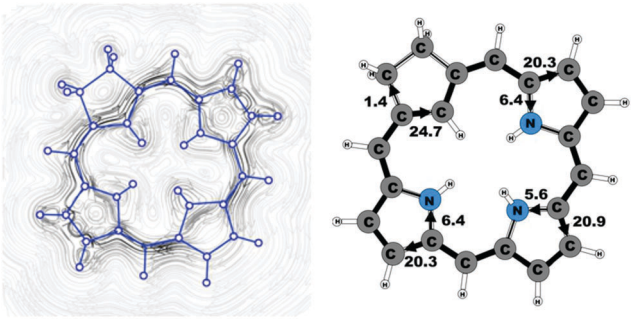

(a) (b)

Fig. 7 (a) A streamline plot of the current density 1 bohr above the carbachlorin **19H**$^+$ molecule that sustains a net ring-current strength of 26.5 nA T^{-1} around the porphyrinoid macroring. (b) The calculated net current strengths (in nA T^{-1}) passing selected bonds are given for carbachlorin **19H**$^+$.

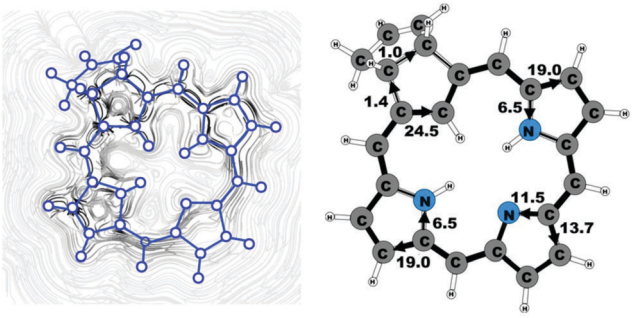

(a) (b)

Fig. 8 (a) A streamline plot of the current density 1 bohr above the carbachlorin **6b** (*cis*) molecule that sustains a net ring-current strength of 25.5 nA T^{-1} around the porphyrinoid macroring. (b) The calculated net current strengths (in nA T^{-1}) passing selected bonds are given for carbachlorin **6b** (*cis*).

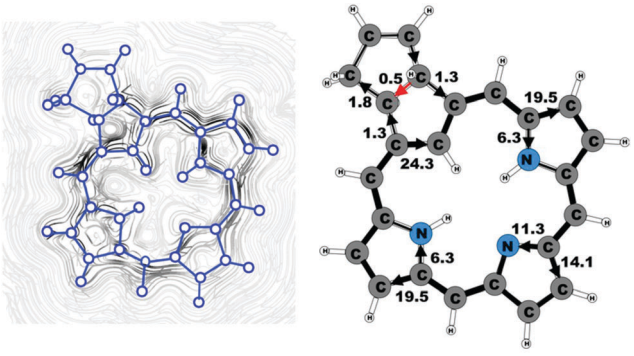

(a) (b)

Fig. 9 (a) A streamline plot of the current density 1 bohr above the carbachlorin **6b** (*trans*) molecule that sustains a net ring-current strength of 25.7 nA T^{-1} around the porphyrinoid macroring. (b) The calculated net current strengths (in nA T^{-1}) passing selected bonds are given for carbachlorin **6b** (*trans*).

The two ends of the propene moiety can bind to the cyclopentadienyl ring in the *cis* **6b** (Fig. 8) or *trans* **6b** (Fig. 9) position.

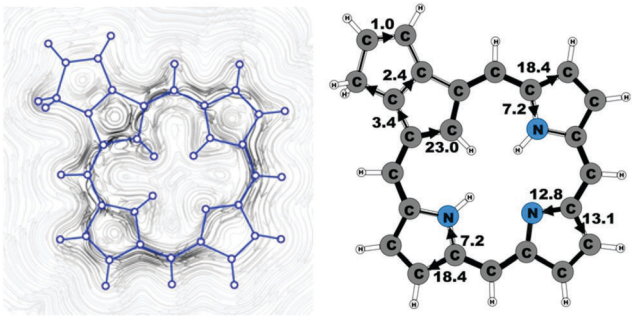

(a) (b)

Fig. 10 (a) A streamline plot of the current density 1 bohr above the carbaporphyrin **9** molecule that sustains a net ring-current strength of 25.9 nA T^{-1} around the porphyrinoid macroring. (b) The calculated net current strengths (in nA T^{-1}) passing selected bonds are given for carbaporphyrin **9**.

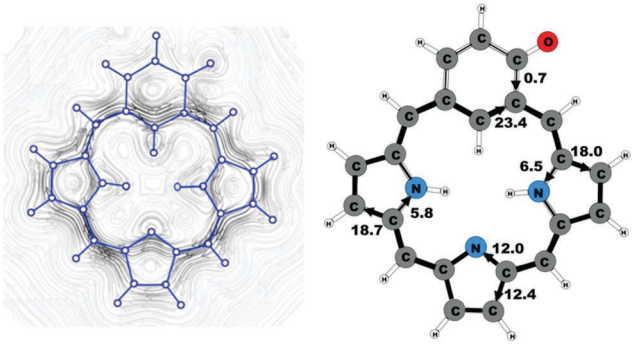

(a) (b)

Fig. 11 (a) A streamline plot of the current density 1 bohr above the oxybenziporphyrin **1** molecule that sustains a net ring-current strength of 24.4 nA T^{-1} around the porphyrinoid macroring. (b) The calculated net current strengths (in nA T^{-1}) passing selected bonds are given for oxybenziporphyrin **1**.

Compounds **6b** are propencarbachlorins, because the C_β–$C_{\beta'}$ bond of the cyclopentadienyl ring becomes saturated when binding the propene moiety to the cyclopentadienyl. Carbaporphyrins like compound **9** (Fig. 10) could in principle be obtained by oxidizing the corresponding carbachlorin. However, experimentally this is not straightforward since Li and Lash reported that they were not able to oxidize **6b**,[9] which would have yielded the corresponding carbaporphyrin **9**.

Compounds **1**–**4** are modified carbaporphyrinoids. In oxybenziporphyrin **1** (Fig. 11), the cyclopentadienyl ring is replaced by a cylohexadienone moiety. In benzocarbaporphyrin **2** (Fig. 12), a benzoic ring is fused to the cyclopentadienyl ring. In azuliporphyrin **3** (Fig. 13), a cycloheptatriene ring is fused to the cyclopentadienyl ring, and in tropiporphyrin **4** (Fig. 14), the cyclopentadienyl ring is replaced by a cycloheptatrienyl ring.

4 Current-density calculations

All the investigated compounds are found to be aromatic according to the magnetic criterion. Streamline representations

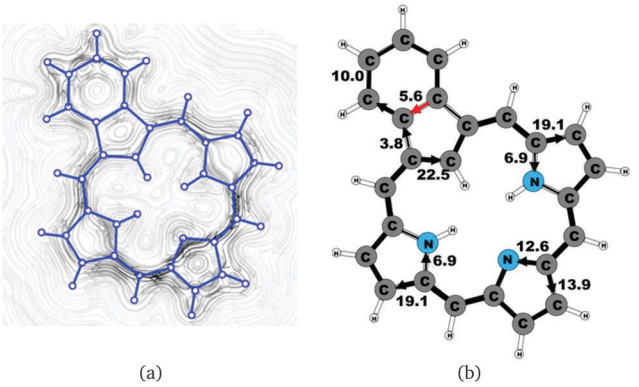

(a) (b)

Fig. 12 (a) A streamline plot of the current density 1 bohr above the benzocarbaporphyrin **2** molecule that sustains a net ring-current strength of 26.5 nA T^{-1} around the porphyrinoid macroring. (b) The calculated net current strengths (in nA T^{-1}) passing selected bonds are given for benzocarbaporphyrin **2**.

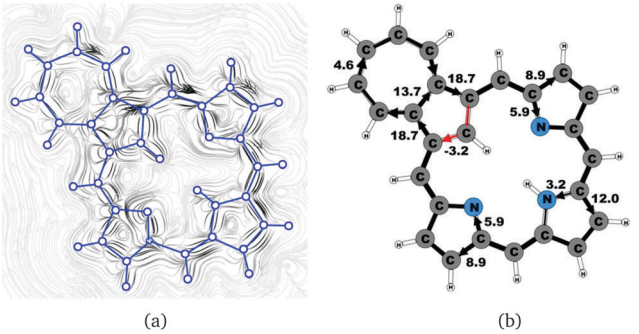

(a) (b)

Fig. 13 (a) A streamline plot of the current density 1 bohr above the azuliporphyrin **3** molecule that sustains a net ring-current strength of 15.1 nA T^{-1} around the porphyrinoid macroring. (b) The calculated net current strengths (in nA T^{-1}) passing selected bonds are given for azuliporphyrin **3**.

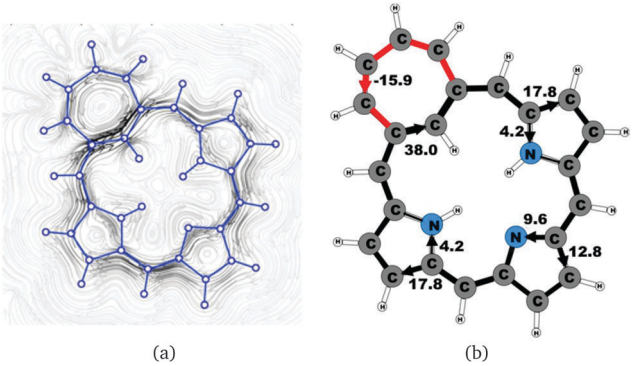

(a) (b)

Fig. 14 (a) A streamline plot of the current density 1 bohr above the tropiporphyrin **4** molecule that sustains a net ring-current strength of 21.9 nA T^{-1} around the porphyrinoid macroring. (b) The calculated net current strengths (in nA T^{-1}) passing selected bonds are given for tropiporphyrin **4**.

of the current densities obtained in a plane placed 1 bohr above the molecular plane and the calculated current density pathways that are obtained through explicit integration of the current flow across several chemical bonds are given in Fig. 1–14. An overview of the calculated results is given in Table 1 and the respective labeling of the pyrrolic rings is shown in Fig. 15.

Table 1 The total ring-current strength (in nA T^{-1}) and the current strengths (in nA T^{-1}) of the outer and inner pathways of the studied carbaporphyrinoids. The numbering of the currents is shown in Fig. 15

Ring →		A		B		C		D	
molecule	Total	1	2	3	4	5	6	7	8
20	26.8	6.3	20.5	17.7	7.3	13.0	13.8	17.7	7.3
20H^{+}	25.7	1.8	23.9	19.2	6.5	19.8	6.0	19.2	6.5
20H$_2^{2+}$	27.8	27.0	0.9	19.6	8.1	21.1	6.4	19.7	8.2
14	24.8	4.8	20.3	17.8	6.8	12.8	12.3	17.8	6.8
19	24.6	1.5	23.8	18.5	5.9	13.5	10.8	18.5	5.9
19′	26.1	1.6	24.3	13.6	12.7	20.0	6.2	20.4	5.6
19H^{+}	26.5	1.4	24.7	20.3	6.4	20.9	5.6	20.3	6.4
6b (*cis*)	25.5	1.4	24.5	19.0	6.5	13.7	11.5	19.0	6.5
6b (*trans*)	25.7	1.3	24.3	19.5	6.3	14.1	11.3	19.5	6.3
9	25.9	3.4	23.0	18.4	7.2	13.1	12.8	18.4	7.2
1	24.4	0.7	23.4	18.0	6.5	12.4	12.0	18.7	5.8
2	26.5	3.8	22.5	19.1	6.9	13.9	12.6	19.1	6.9
3	15.1	18.7	−3.2	8.9	5.9	12.0	3.2	8.9	5.9
4	22.1	−15.9	38.0	17.8	4.2	12.8	9.6	17.8	4.2

The current density calculations show that the aromatic pathway of the studied carbaporphyrinoids does not follow the classical 18π aromaticity route of porphyrinoids as suggested by Li and Lash.[9] This is not surprising, since the classical 18π aromatic pathway of porphyrins and chlorins might not even be correct.[10,22,59,81] The aromatic pathways of the studied carbaporphyrins and carbachlorins are indeed very reminiscent of the aromatic pathway of porphyrins and chlorins as previously obtained in current density calculations.[22] Similar current pathways as obtained for the carbaporphyrinoids have also been obtained in a number of current density studies on other porphyrinoids.[20–28]

For all studied compounds, the ring current divides into an outer and an inner pathway at each pyrrolic subring. Thus, all π-electrons of the pyrrolic rings take part in the delocalization pathways. The calculations show that the resistance of the inner NH group is generally larger than for the inner nitrogen without a hydrogen. Thus, a stronger current passes the inner N than the inner NH moiety of the pyrrolic rings. For the pyrrolic rings without an inner hydrogen, the current strengths *via* the outer and inner pathways are almost the same, whereas for the

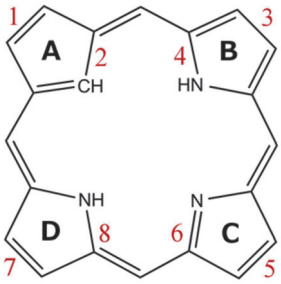

Fig. 15 The numbering of the current pathways of the carbaporphyrinoids. Odd numbers indicate outer routes.

pyrrolic rings with an inner hydrogen roughly 25% of the current takes the inner route. Thus, the common notion that the main part of the current takes the inner route at the pyrrolic rings without an inner hydrogen is incorrect. One of the main conclusions of this work is that all current pathways for the carbaporphyrinoids suggested by Li and Lash are not completely correct.[9] A comparison of the diatropic and paratropic contributions to the net current strength passing the meso-carbon with the ones passing *via* the inner and outer routes of the pyrrolic rings show that the pyrrolic rings do not sustain any strong local ring currents. In the following, we discuss in more detail the current pathways at the all-carbon subrings of the studied carbaporphyrinoids.

4.1 Carbaporphyrins 20, $20H^+$ and $20H_2^{2+}$

Molecule **20** is the unsubstituted *trans*-carbaporphyrin lacking the inner hydrogen in the *trans* position relative to the cyclopentadienyl ring. The calculations of the current density for **20** have recently been reported,[27] whereas in this work we have also studied the current densities of the protonated $\mathbf{20H^+}$ and diprotonated $\mathbf{20H_2^{2+}}$ forms of **20**. The current pathways are shown in Fig. 1–3. At the cyclopentadienyl ring the inner pathway dominates for **20** and $\mathbf{20H^+}$. For **20**, only 6.3 nA T^{-1} of the total ring current of 26.8 nA T^{-1} takes the outer route.[27] For the protonated form, the current strength of 1.8 nA T^{-1} along the outer pathway is even weaker, whereas the total ring-current strength of 25.7 nA T^{-1} is practically the same as for the unprotonated **20**. The doubly protonated $\mathbf{20H_2^{2+}}$ has five inner hydrogens implying that the inner carbon of the all-carbon five-membered subring is saturated. For $\mathbf{20H_2^{2+}}$, the ring current of 27.8 nA T^{-1} is slightly larger than for **20** and mainly takes the outer route, whose current strength is 27.0 nA T^{-1} as compared to the tiny 0.9 nA T^{-1} along the inner pathway. For these molecules, Li and Lash suggested an 18π aromaticity, where the inner NH groups and the C_β atoms of the pyrrolic ring without an inner hydrogen do not belong to the aromatic pathway.[9] Proton and carbon NMR spectroscopy suggest that **20** is planar,[9] whereas according to the calculations the planar form is a transition state. The small barrier of 1.9 kcal mol^{-1} does not prevent the thermal motion across the barrier implying that the molecule is on the average planar. The ring-current strength of planar **20** is 26.2 nA T^{-1} showing that the small nonplanarity of **20** does not significantly affect the aromatic properties.

4.2 Carbaporphyrin 14

Substituent effects were studied by adding an aldehyde group to one of the C_β positions of the cyclopentadienyl ring. Carbaporphyrin **14** with an aldehyde group in the C_β position as shown in Fig. 4 sustains a net ring-current whose strength is 24.8 nA T^{-1}. The net ring-current is 2.0 nA T^{-1} smaller than the one obtained for **20**,[27] whereas the current strength of 20.3 nA T^{-1} along the inner pathway at the cyclopentadienyl ring is almost the same for **14** and **20**. Substitution of the aldehyde group to the C_β position of the cyclopentadienyl ring decreases the current strength along the outer pathway by 1.5 nA T^{-1}, which is probably due to the electron withdrawing effect of the aldehyde group. However, the substitution does not influence the current pattern of the rest of the molecule.

4.3 Carbachlorins 19, 19′ and $19H^+$

The studied carbachlorins **19**, **19′** and $\mathbf{19H^+}$ are identical to **11**, **11′** and $\mathbf{11H^+}$ that were synthesized by Li and Lash,[9] when the alkyl substituents in the C_β positions are omitted. The calculated ring-current strength of **19** is 24.6 nA T^{-1}. As expected, most of the ring current (23.8 nA T^{-1}) passes on the inside of the cyclopentadienyl ring, whereas only 1.5 nA T^{-1} takes the outer route *via* the saturated C_β carbons. A current-density plot and the current strengths are shown in Fig. 5. The current-density analysis reveals that the current pathway of **19** is very similar to the ones obtained for the other carbachlorin compounds. However, the ring current is somewhat stronger along the outer route at the pyrrolic rings than for the carbaporphyrins. For example, 56% of the ring current passes the C_β carbons of the pyrrolic ring without an inner hydrogen. Li and Lash suggested that the ring current takes the outer pathway at the pyrrolic rings with inner hydrogens and the inner one at the pyrrolic ring without the inner hydrogen,[9] which is the traditional but incorrect aromatic pathway of porphyrins and chlorins. Thus, the suggested aromatic pathway of carbachlorin **19** is not completely correct.[9]

The current pathway of tautomer **19′** is very similar to that of **19**. The largest difference in the current pattern is obtained for the pyrrolic ring without the inner hydrogen, where current strengths along the outer and inner routes are almost equal in this case. The net current strength of 26.1 nA T^{-1} is about 1.5 nA T^{-1} larger than for **19**. The current strengths are shown in Fig. 6. The aromatic pathway at each of the pyrrolic rings looks like the aromatic pathway for **19** and **19′** at the pyrrolic rings with an inner hydrogen. Thus, the ring current flows mainly along the outer bonds of the protonated carbachlorin $\mathbf{19H^+}$. The current pathways are shown in Fig. 7. Li and Lash suggested that the aromatic pathway for $\mathbf{19H^+}$ can be considered as a superposition of three pathways because the NICS values in the three pyrrolic rings are practically the same.[9] Since the total ring-current strength is 26.5 nA T^{-1}, each of these pathways would have a current strength of almost 9 nA T^{-1}. The superposed current pattern would then be 17.7 nA T^{-1} along the outer pathway and 8.8 nA T^{-1} *via* the inner route, which can be compared to the calculated combined current of 20.3–20.9 nA T^{-1} along the outer route and 5.6–6.4 nA T^{-1} takes the inner one. When applying the superposition principle, the current flow of 1.4 nA T^{-1} passing the saturated C_β atoms of the all-carbon five-membered ring introduces uncertainties of 0.5 nA T^{-1} and 1.0 nA T^{-1} in the current strengths of the inner and outer pathways, respectively. Thus, the ratio between the current strengths of the outer and inner pathways is too large for validating the superposition principle.

4.4 Carbachlorin 6b

Carbachlorin **6b** (*cis*) sustains a net current strength of 25.5 nA T^{-1} of which 24.5 nA T^{-1} takes the inner pathway at the all-carbon five-membered ring. At the pyrrolic rings, the ring current follows largely the same pattern as in the corresponding unsubstituted

carbachlorin **19**. The calculated current pattern at the pyrrolic rings of compound **6b** (*trans*) is very similar to the one obtained for **6b** (*cis*). The net current strength is 25.7 nA T^{-1}. The current flow at the propene substituted all-carbon five-membered ring of 1.3 nA T^{-1} takes the outermost route. In addition the fused cyclopentene ring due to the propene substitution sustains a tiny local ring current of 0.5 nA T^{-1}.

4.5 Carbaporphyrin 9

Carbaporphyrin **9** can in principle be obtained by oxidizing carbachlorin **6**. However, that reaction step was unsuccessful.[9] Current-density calculations show that carbaporphyrin **9** is expected to have similar ring-current pathways as obtained for the unsubstituted carbaporphyrin **20**. The net ring-current strength is 25.9 nA T^{-1} as compared to 26.8 nA T^{-1} for **20** and 25.5–25.7 nA T^{-1} for **6b**. A small current of 1.0 nA T^{-1} passes the saturated CH_2 group of the cyclopentene ring fused to the cyclopentadienyl ring of the carbaporphyrin, whereas a current strength of 2.4 nA T^{-1} passes the common bond of the two five-membered rings.

4.6 Oxybenziporphyrin 1

Oxybenziporphyrin **1** is a carbaporphyrinoid where the cyclopentadienyl ring is replaced by a cylohexadienone ring.[52] **1** sustains a net ring-current strength of 24.4 nA T^{-1} around the macrocycle, which is 3 nA T^{-1} (10%) smaller than for porphyrin.[22] The current pattern at the pyrrolic rings is the same as for porphyrin and the other carbaporphyrinoids studied in this work. The current strengths along the different routes are shown in Fig. 11. The carbonyl group of the cylohexadienone ring prevents the ring-current to take the outer route. Thus, only 0.7 nA T^{-1} flows on the outside of the cylohexadienone ring and 23.4 nA T^{-1} takes the inner pathway. The net ring-current strength calculated for the molecular structure of **1** optimized at the same level of theory using also the D3 correction differs by only 0.3 nA T^{-1} from the value of 24.4 nA T^{-1} as obtained without the D3 correction. Thus, the use of the D3 correction has almost no effect on the ring current strengths of the investigated class of molecules.

4.7 Benzocarbaporphyrin 2

Benzocarbaporphyrin **2** is a carbaporphyrin with a benzoic ring fused to the C_β bond of the cyclopentadienyl ring.[49] The current pattern at the pyrrolic rings is very similar to that of the other carbaporphyrinoids of this work. The ring-current strength around the macrocycle of 26.5 nA T^{-1} is almost as large as for unsubstituted carbaporphyrin **20**. At the cyclopentadienyl ring, the current prefers the inner route whose strength is 22.5 nA T^{-1}, whereas a current of 3.8 nA T^{-1} flows outwards passing on the outside of the benzoic ring. The benzoic ring sustains a local ring current of 5.6 nA T^{-1}. The current pathway and current strengths are shown in Fig. 12. The current density calculations show that the proposed 18π aromatic pathway is not completely correct.[49,52]

4.8 Azuliporphyrin 3

Azuliporphyrin **3** consists of a cycloheptatriene ring fused to the cyclopentadienyl ring of carbaporphyrin **20**. Lash *et al.* proposed that it has some aromatic character, because the structure can formally be described by two resonance structures.[49,52] The zwitterionic form is thought to sustain a ring current around the carbaporphyrin macrocycle, whereas in the other form the ring current circles only around the azulene moiety.[49] However, the current density calculations yield a somewhat different picture of the aromatic character. The strength of the ring current circling around the carbaporphyrin macroring is 15.1 nA T^{-1}, which is about 55% of the ring-current strength of porphyrin. At the azulene moiety the main current of 18.7 nA T^{-1} takes the outer route around the cyclopentadienyl ring, whereas a weaker current of 4.6 nA T^{-1} passes on the outside of the cycloheptatrienyl ring. The cyclopentadienyl ring sustains a weak local ring current of 3.2 nA T^{-1}. At the pyrrolic rings, the main current flow passes the C_β carbons. At the pyrrolic rings without an inner hydrogen, 40% of the current takes the inner route, whereas at the pyrrolic ring with an inner hydrogen only 20% of the current passes the NH moiety. The current pathways and current strengths are shown in Fig. 13.

4.9 Tropiporphyrin 4

The calculated structure of tropiporphyrin **4**, which is obtained from carbaporphyrin by replacing the cyclopentadienyl ring with a cycloheptatrienyl ring,[55] is found to be almost planar with the largest out-of-plane torsional angle of 3° at the cycloheptatrienyl ring. The current strength of tropiporphyrin is 22.1 nA T^{-1}, which is 82% of the ring-current strength of carbaporphyrin **20**. The ring current around the macrocycle mainly passes along the outer routes at the pyrrolic rings. The pattern of the current flow around the carbaporphyrin ring is similar to the one for the other carbaporphyrins with about 20% of the ring current passing the NH moiety of the two pyrrolic rings with an inner hydrogen, whereas 43% of the ring current passes the nitrogen of the pyrrolic ring without an inner hydrogen. The cycloheptatrienyl ring is antiaromatic sustaining a strong local paratropic ring current of −15.9 nA T^{-1}, thus forming a strongly antiaromatic ring fused to the aromatic one. Fused rings with opposite tropicity have previously been found for thienopyrrole modified 20π-electron porphyrinoids and thieno-bridged porphyrins.[23,25] The current pathways and current strengths in Fig. 14 show that the calculations yield a different aromatic character as compared to the one deduced from the measured NMR chemical shifts.[55]

5 Summary and conclusions

Magnetically induced current densities of a number of synthesized as well as spectroscopically and theoretically characterized carbachlorins and carbaporphyrins[9] have been studied computationally at the DFT level and analyzed using the gauge including magnetically induced current (GIMIC) method. The investigated compounds are found to be aromatic with calculated ring-current strength susceptibilities ranging from 15 nA T^{-1} to 27 nA T^{-1}. Thus, they can be considered aromatic according to the magnetic criterion. Tropiporphyrin **3** has the weakest aromaticity among the

studied molecules with a ring-current strength of 15.1 nA T^{-1}, which can be compared to the ring-current strength of 12.0 nA T^{-1} for benzene.[29] The calculated ring-current strengths and the current strengths of different pathways are summarized in Table 1 and the numbering of the bonds and rings are shown in Fig. 15.

For most of the investigated carbaporphyrinoids, the inner pathway at the five membered all-carbon ring (A) is the preferred route and only a small current of 0.7 nA T^{-1} to 4.2 nA T^{-1} passes on the outer side of the ring, regardless of whether the bond is saturated or not. The only exceptions are $\mathbf{20H_2}^{2+}$, **3** and **4**, where the inner pathway is blocked by the saturated CH_2, a cycloheptatriene ring is fused to the cyclopentadienyl ring, and a cycloheptatrienyl ring replaces the cyclopentadienyl ring, respectively. Previous studies on aromatic molecules have also shown how the insertion of CH_2 moieties leads to changes in the current flow around porphyrinoids.[22,27,28] Insertion of an aldehyde group to the cyclopentadienyl ring of carbaporphyrin **14** did not significantly affect the current density pattern and current strengths as compared to the unsubstituted carbaporphyrin **20**. For azuliporphyrin **3** a cycloheptatriene ring is fused to the cyclopentadienyl ring, the ring current prefers the outer route. The current even splits into one branch passing around the cycloheptatrienyl ring, whereas the main current streams along the common bond between the cycloheptatrienyl and cyclopentadienyl rings. Tropiporphyrin **4** consists of an anti-aromatic cycloheptatrienyl ring fused to the aromatic porphyrinoid macroring leading to a weaker ring-current strength of 21.9 nA T^{-1} as compared to 26.8 nA T^{-1} for carbaporphyrin **20**. Similar current-strength trends were obtained for the pyrrolic rings as previously reported for other porphyrinoid compounds.[22,27,28] For the investigated compounds the ring current divides at the pyrrolic rings into the inner and outer branches showing that all π-electrons of the pyrrolic rings participate in the current pathway. For pyrrolic rings B and D with an inner hydrogen, the main share of the current flows on the outside of the ring, whereas at the pyrrolic rings without an inner hydrogen. At ring C without an inner hydrogen, the current is almost equally split into the inner and outer branches or the main current pathway is along the outer route.

In conclusion, for the investigated compounds the calculated current pathways disagree with previously proposed ones. Lash *et al.* have proposed that the aromatic pathway of the studied carbaporphyrinoids follow an 18π-electron aromaticity route that excludes the $C_\beta{=}C_{\beta'}$ bond of ring C, whereas the explicit current-density calculations of this work show that the ring current is generally stronger along the outer pathway of ring C than for the inner route.[9,49,52,55] Furthermore, we show that all π-electrons of the pyrrolic rings participate in the electron delocalization pathway. For tropiporphyrin **4**, the current-density analysis shows that the fused cycloheptatrienyl ring is antiaromatic. In general, the integration based current-density analysis provides accurate and reliable information about the aromatic character and the aromatic pathways of the studied multiring molecules. We suggest that one should not merely use spectroscopic data in combination with magnetic shielding calculations when aiming at information about the aromatic character of porphyrinoids, because the approaches do not provide very accurate information about molecular aromaticity for more complex molecules. Instead it is recommended to use current-density calculations in combination with numerical integration of current strengths, because this yields electron-delocalization pathways that show how electrons move around the molecular rings, when they are exposed to an external magnetic field.

Acknowledgements

This research was supported by the Academy of Finland through projects (137460 and 266227) and its Computational Science Research Programme (LASTU/258258). DS thanks Magnus Ehrnrooth Foundation, Swedish Cultural Foundation in Finland, Alexander von Humboldt Fundation and Fulbright Foundation for financial support during his sabbatical leave. CSC – the Finnish IT Center for Science – is acknowledged for computer time. H. F. thanks the Norwegian Research Council through the CoE Centre for Theoretical and Computational Chemistry (Grant No. 179568/V30 and 231571/F20) for support. This work had received support from the Norwegian Supercomputing Program (NOTUR) through a grant of computer time (Grant No. NN4654K).

References

1 A. Berlicka, P. Dutka, L. Szterenberg and L. Latos-Grażyński, *Angew. Chem., Int. Ed.*, 2014, **53**, 4885–4889.
2 S. Aronoff and M. Calvin, *J. Org. Chem.*, 1943, **8**, 205–223.
3 M. O. Senge, *Angew. Chem., Int. Ed.*, 2011, **50**, 4272–4277.
4 K. Berlin, *Angew. Chem., Int. Ed.*, 1996, **35**, 1820–1822.
5 T. D. Lash and S. T. Chaney, *Chem. – Eur. J.*, 1996, **2**, 944–948.
6 M. Pawlicki and L. Latos-Grażyński, *Chem. Rec.*, 2006, **6**, 64–78.
7 R. K. Pandey and G. Zheng, in *Porphyrin Handbook*, ed. K. M. S. K. M. Kadish and R. Guilard, Academic Press, San Diego, CA, 2000, vol. 6, pp. 157–230.
8 T. D. Lash, *Eur. J. Org. Chem.*, 2007, 5461–5481.
9 D. Li and T. D. Lash, *J. Org. Chem.*, 2014, **79**, 7112–7121.
10 J. Jusélius, D. Sundholm and J. Gauss, *J. Chem. Phys.*, 2004, **121**, 3952–3963.
11 S. Taubert, D. Sundholm and J. Jusélius, *J. Chem. Phys.*, 2011, **134**, 054123.
12 H. Fliegl, S. Taubert, O. Lehtonen and D. Sundholm, *Phys. Chem. Chem. Phys.*, 2011, **13**, 20500–20518.
13 M. P. Johansson, J. Jusélius and D. Sundholm, *Angew. Chem., Int. Ed.*, 2005, **44**, 1843–1846.
14 J. Jusélius and D. Sundholm, *Phys. Chem. Chem. Phys.*, 2008, **10**, 6630–6634.
15 S. Taubert, J. Jusélius, D. Sundholm, W. Klopper and H. Fliegl, *J. Phys. Chem. A*, 2008, **112**, 13584–13592.
16 S. Taubert, D. Sundholm and F. Pichierri, *J. Org. Chem.*, 2010, **75**, 5867–5874.
17 H. Fliegl, O. Lehtonen, D. Sundholm and V. R. I. Kaila, *Phys. Chem. Chem. Phys.*, 2011, **13**, 434–437.

18 M. Kaipio, M. Patzschke, H. Fliegl, F. Pichierri and D. Sundholm, *J. Phys. Chem. A*, 2012, **116**, 10257–10268.
19 D. Sundholm, *Phys. Chem. Chem. Phys.*, 2013, **15**, 9025–9028.
20 H. Fliegl, D. Sundholm, S. Taubert and F. Pichierri, *J. Phys. Chem. A*, 2010, **114**, 7153–7161.
21 H. Fliegl, D. Sundholm and F. Pichierri, *Phys. Chem. Chem. Phys.*, 2011, **13**, 20659–20665.
22 H. Fliegl and D. Sundholm, *J. Org. Chem.*, 2012, **77**, 3408–3414.
23 H. Fliegl, N. Özcan, R. Mera-Adasme, F. Pichierri, J. Jusélius and D. Sundholm, *Mol. Phys.*, 2013, **111**, 1364–1372.
24 R. R. Valiev, H. Fliegl and D. Sundholm, *J. Phys. Chem. A*, 2013, **117**, 9062–9068.
25 R. R. Valiev, H. Fliegl and D. Sundholm, *Phys. Chem. Chem. Phys.*, 2014, **16**, 11010–11016.
26 H. Fliegl, F. Pichierri and D. Sundholm, *J. Phys. Chem. A*, 2015, **119**, 2344–2350.
27 R. R. Valiev, H. Fliegl and D. Sundholm, *J. Phys. Chem. A*, 2015, **119**, 1201–1207.
28 R. R. Valiev, H. Fliegl and D. Sundholm, *Phys. Chem. Chem. Phys.*, 2015, **17**, 14215–14222.
29 H. Fliegl, D. Sundholm, S. Taubert, J. Jusélius and W. Klopper, *J. Phys. Chem. A*, 2009, **113**, 8668–8676.
30 A. Balaban, P. von Ragué Schleyer and H. S. Rzepa, *Chem. Rev.*, 2005, **105**, 3436–3447.
31 T. Heine, C. Corminboeuf and G. Seifert, *Chem. Rev.*, 2005, **105**, 3889–3910.
32 Z. Chen, C. S. Wannere, C. Corminboeuf, R. Puchta and P. von Ragué Schleyer, *Chem. Rev.*, 2005, **105**, 3842–3888.
33 P. Lazzeretti, *Phys. Chem. Chem. Phys.*, 2004, **6**, 217–223.
34 S. Pelloni, G. Monaco, P. Lazzeretti and R. Zanasi, *Phys. Chem. Chem. Phys.*, 2011, **13**, 20666–20672.
35 P. Lazzeretti, *Prog. Nucl. Magn. Reson. Spectrosc.*, 2000, **36**, 1–88.
36 I. Morao, B. Lecea and F. P. Cossío, *J. Org. Chem.*, 1997, **62**, 7033–7036.
37 J. Jusélius and D. Sundholm, *Phys. Chem. Chem. Phys.*, 1999, **1**, 3429–3435.
38 J. O. C. Jiménez-Halla, E. Matito, J. Robles and M. Solá, *J. Organomet. Chem.*, 2006, **691**, 4359–4366.
39 S. Pelloni and P. Lazzeretti, *J. Phys. Chem. A*, 2013, **117**, 9083–9092.
40 Z. Badri, S. Pathak, H. Fliegl, P. Rashidi-Ranjbar, R. Bast, R. Marek, C. Foroutan-Nejad and K. Ruud, *J. Chem. Theory Comput.*, 2013, **9**, 4789–4796.
41 G. Monaco and R. Zanasi, *J. Phys. Chem. A*, 2014, **118**, 1673–1683.
42 D. Du, H. Fliegl and D. Sundholm, *J. Chin. Chem. Soc.*, 2016, **63**, 93–100.
43 Y. C. Lin, D. Sundholm and J. Jusélius, *J. Chem. Theory Comput.*, 2006, **2**, 761–764.
44 S. Taubert, D. Sundholm and F. Pichierri, *J. Org. Chem.*, 2009, **74**, 6495–6502.
45 R. Islas, G. Martínez-Guajardo, J. O. C. Jiménez-Halla, M. Solá and G. Merino, *J. Chem. Theory Comput.*, 2010, **6**, 1131–1135.
46 A. C. Castro, E. Osorio, J. O. Jiménez-Halla, E. Matito, W. Tiznado and G. Merino, *J. Chem. Theory Comput.*, 2010, **6**, 2701–2750.
47 J. J. Torres, R. Islas, E. Osorio, J. G. Harrison, W. Tiznado and G. Merino, *J. Phys. Chem. A*, 2013, **117**, 5529–5533.
48 T. D. Lash, *Angew. Chem., Int. Ed.*, 1995, **34**, 2533–2535.
49 T. D. Lash, M. J. Hayes, J. D. Spence, M. A. Muckey, G. M. Ferrence and L. F. Szczepura, *J. Org. Chem.*, 2002, **67**, 4860–4874.
50 D. I. AbuSalim and T. D. Lash, *Org. Biomol. Chem.*, 2014, **12**, 8719–8736.
51 T. D. Lash and M. J. J. Hayes, *Angew. Chem., Int. Ed.*, 1997, **36**, 840–842.
52 T. D. Lash, S. T. Chaney and D. T. Richter, *J. Org. Chem.*, 1998, **63**, 9076–9088.
53 S. R. Graham, D. A. Colby and T. D. Lash, *Angew. Chem., Int. Ed.*, 2002, **41**, 1371–1374.
54 T. D. Lash, D. A. Colby, S. R. Graham and S. T. Chaney, *J. Org. Chem.*, 2004, **69**, 8851–8864.
55 K. M. Bergman, G. M. Ferrence and T. D. Lash, *J. Org. Chem.*, 2004, **69**, 7888–7897.
56 T. D. Lash and S. T. Chaney, *Tetrahedron Lett.*, 1996, **37**, 8825–8828.
57 P. von Ragué Schleyer, C. Maerker, A. Dransfeld, H. Jiao and N. J. R. van Eikema Hommes, *J. Am. Chem. Soc.*, 1996, **118**, 6317–6318.
58 M. K. Cyrañski, T. M. Krygowski, M. Wisiorowski, N. J. R. van Eikema Hommes and P. von Ragué Schleyer, *Angew. Chem., Int. Ed.*, 1998, **37**, 177–180.
59 J. Jusélius and D. Sundholm, *Phys. Chem. Chem. Phys.*, 2000, **2**, 2145–2151.
60 E. Steiner and P. W. Fowler, *ChemPhysChem*, 2002, **3**, 114–116.
61 E. Steiner, A. Soncini and P. W. Fowler, *Org. Biomol. Chem.*, 2005, **4**, 4053–4059.
62 J. I. Wu, I. Fernández and P. von Ragué Schleyer, *J. Am. Chem. Soc.*, 2013, **135**, 315–321.
63 A. D. Becke, *J. Chem. Phys.*, 1993, **98**, 5648–5652.
64 C. Lee, W. Yang and R. G. Parr, *Phys. Rev. B: Condens. Matter Mater. Phys.*, 1988, **37**, 785–789.
65 R. Ahlrichs, M. Bär, M. Häser, H. Horn and C. Kölmel, *Chem. Phys. Lett.*, 1989, **162**, 165–169.
66 F. Furche, R. Ahlrichs, C. Hättig, W. Klopper, M. Sierka and F. Weigend, *Wiley Interdiscip. Rev.: Comput. Mol. Sci.*, 2014, **4**, 91–100.
67 A. Schäfer, H. Horn and R. Ahlrichs, *J. Chem. Phys.*, 1992, **97**, 2571–2577.
68 F. Weigend and R. Ahlrichs, *Phys. Chem. Chem. Phys.*, 2005, **7**, 3297–3305.
69 M. Häser, R. Ahlrichs, H. P. Baron, P. Weis and H. Horn, *Theor. Chim. Acta*, 1992, **83**, 455–470.
70 M. Kollwitz, M. Häser and J. Gauss, *J. Chem. Phys.*, 1998, **108**, 8295–8301.
71 S. Taubert, H. Konschin and D. Sundholm, *Phys. Chem. Chem. Phys.*, 2005, **7**, 2561–2569.
72 R. Ditchfield, *Mol. Phys.*, 1974, **27**, 789–807.

73 K. Wolinski, J. F. Hinton and P. Pulay, *J. Am. Chem. Soc.*, 1990, **112**, 8251–8260.
74 XMakemol, http://www.nongnu.org/xmakemol/.
75 paint.net 4.0.6, http://www.getpaint.net/.
76 Marvin 15.9.28, 2015, ChemAxon, http://www.chemaxon.com.
77 PyNgl: Scientific visualization Python program package, http://www.pyngl.ucar.edu.
78 ChemBioDraw Ultra 14.0 by PerkinElmer, http://scistore.cambridgesoft.com.
79 gimp: GNU Image Manipulation Program, http://www.gimp.org.
80 S. Grimme, J. Antony, S. Ehrlich and H. Krieg, *J. Chem. Phys.*, 2010, **132**, 154104.
81 J. Jusélius and D. Sundholm, *J. Org. Chem.*, 2000, **65**, 5233–5237.